THE UNIVERSITY OF CHICAGO

PRECISION SPECTROSCOPY OF LASER TRAPPED HELIUM AND RADIUM ATOMS

A DISSERTATION SUBMITTED TO
THE FACULTY OF THE DIVISION OF THE PHYSICAL SCIENCES
IN CANDIDACY FOR THE DEGREE OF
DOCTOR OF PHILOSOPHY

DEPARTMENT OF PHYSICS

BY
IBRAHIM ARCHIBALD SULAI

CHICAGO, ILLINOIS
DECEMBER 2011

ABSTRACT

A laser spectroscopic measurement of the nuclear charge radius of ^{6}He ($t_{1/2} = 806$ ms) and ^{8}He ($t_{1/2} = 119$ ms) is reported. This is the first nuclear-model independent determination of the charge radius of ^{8}He and is an improvement over a previous determination made for ^{6}He. Atomic isotope shift measurements between ^{8}He and ^{4}He as well as between ^{6}He and ^{4}He on the $2^3S_1 - 3^3P_J$ transitions were performed. The isotope shift can be considered as a sum of two parts, a "mass shift" which is proportional to the difference in nuclear recoil energy of the two isotopes, and a "field shift" which is proportional to the difference in their mean square charge radii. By performing precise isotope shift measurements and using high precision atomic theory calculations of helium for the mass shift, the field shift was determined. This, along with the charge radius of ^{4}He—known precisely from electron scattering, yielded the values 2.061 ± 0.008 fm and 1.955 ± 0.017 fm for the charge radii of ^{6}He and ^{8}He respectively. Also, the hyperfine intervals in the 3^3P manifold of ^{3}He were measured with improved precision. In addition, the suppression of certain allowed transitions in ^{3}He due to the breakdown of LS coupling was investigated.

In the second half of this work, results of studies towards a search for a non-zero permanent electric dipole moment (EDM) of ^{225}Ra are given. A non-zero EDM would signify the violation of the discrete symmetries of parity (P) and time-reversal symmetry (T). It is believed that because of its nuclear structure, ^{225}Ra is a particularly sensitive system to search for P and T violation. The search will be performed in a sample of radium atoms trapped in a one dimensional optical lattice. The details of laser cooling, trapping and manipulation of radium atoms towards enabling the EDM search are reported. In addition, the lifetime of the $7s6d^1D_2$ atomic level of radium was measured for the first time to be 385 ± 45 μs.

ACKNOWLEDGMENTS

While working on my PhD at the University of Chicago, and performing experiments at Argonne National Lab, I have had the privilege of working on some very interesting projects and of learning a great deal. This is primarily because of the people I have had the good fortune of working and interacting with. And so, I want to thank my adviser Zheng-Tian Lu for taking me on as a student and for availing me with these opportunities. I have fond memories of working with Lu late into the night—searching for that factor of a few in helium trapping efficiency and of taking data during our ^{8}He run. Thank you Lu for, among many things, your example of how to approach problems, as well as for thoroughly reading through drafts of my thesis and giving me good feedback.

I acknowledge the support of the Medium Energy Physics group at Argonne and in particular Roy Holt for sharing his wealth of knowledge and experience each week as we discussed progress on the experiments. I also acknowledge the support of Bob Wiringa, who on multiple occasions, took time to help me understand the Quantum Monte Carlo calculations of helium. He also provided me with many useful figures used in this work. Teng-Lek Khoo also took time to explain details of nuclear deformations to me.

The first project I worked on was with Peter Mueller. Thank you Peter for your patience with me and for your thoughtful instruction. You gave me space to learn and grow as we worked in the BGO area as well as at GANIL. Thank you for being available with your wealth of experience as I transitioned to working on radium.

Kevin Bailey and Tom O'Connor designed many of the beautiful apparatus that made these experiments possible. Thank you Tom and Kevin for the many images that you provided for me, as well Kevin, for the best supply of coffee in building 203. Antonio Villari, Robert Alves Conde, Juan Antonio Nunez and other scientists at GANIL helped make my stay in Caen during our ^{8}He experiment very interesting and the run successful. With

Michael Bishof, I had a good time studying ^{3}He as well as packing up our helium lab from GANIL.

With Will Trimble, I worked on the radium experiment. Thank you Will for your very unique and entertaining ways of communicating physical ideas. Also, thank you for supplying me with food when I worked late at Argonne. I worked with Richard Parker, Matt Dietrich and Jaideep Singh in the final years of this work, and acknowledge their support. I also acknowledge the support and encouragement of John Greene and Bruce Nardi for their helpfulness whenever I approached them, as well as for the kind words they frequently shared with me when our paths crossed in the hallway. I thank previous and current ATTA group mates, Yun Ding, Wei Jiang, Will Williams and others with whom I bounced ideas off and learned a great deal, even though I didn't work directly with you.

I also acknowledge the other members of my thesis committee: Professors Ed Blucher, Paul Wiegmann, and Cheng Chin for taking the time to read my thesis and for the useful feedback.

I thank the community of friends I have made over the years at the University, at GCF, and at Church. You helped lift me up when I needed encouragement and were there to celebrate with me in happy times. Finally, I thank my family, Baba, Mama, Lengy, Lisha, Nanna and Yusufu for your encouragement, love and support throughout this time. This work was supported by the Department of Energy, as well as from a fellowship from the Grainger Foundation.

TABLE OF CONTENTS

LIST OF FIGURES

LIST OF TABLES

CHAPTER 1

INTRODUCTION

Precision measurements have played very important roles in informing our understanding of the physical world. As experiments reach greater levels of precision, their sensitivity to more subtle effects is increased. This often demands the reformulation of physical theories—leading to greater insight as to the nature of the forces and mechanisms that make our universe operate as it does. This has been the story of physics over the years. We hope, in the work reported here, to contribute to this rich tradition of precision measurements by performing laser spectroscopy on helium and radium atoms.

In the first half of this thesis, we will test nuclear theory for the light helium isotopes by providing measurements of an **allowed** moment of the nuclear charge distribution—the RMS nuclear charge radius. In the second half of the work, we are motivated by the prospects of detecting evidence of physics beyond the standard model. The signature for this is that a **forbidden** moment of the charge distribution—the permanent electric dipole moment (EDM) of radium-225, would be detected to be non-vanishing. Both classes of experiments rely on the laser cooling and trapping of radioactive atoms. The high selectivity and robustness of these techniques make the measurements possible with relatively few atoms.

For our studies of helium reported in Part-I of the thesis, we were particularly interested in studying the structure of the neutron rich helium isotopes ^{6}He and ^{8}He by determining their RMS nuclear charge radii. Chapters 2 to 4 give a motivation for the experiment, as well as a review of experimental probes for determining nuclear sizes. In chapter 5, we describe in detail our experiment to measure the charge radius of ^{6}He and ^{8}He. We give an overview of the hardware required, as well as the data analysis of results obtained. In chapters 6 and 7, we describe some supporting work, consisting of spectroscopy of ^{3}He. This involved measuring the hyperfine intervals in the 3^3P manifold, as well as investigating the

suppression of some 'allowed' transitions in ^{3}He.

In Part-II of this work, we report on our studies of radium. The primary motivation for studying radium is that it is an attractive system to use in searching for the violation of parity (P) and time - reversal symmetry (T). Any such violation of both P and T would be indicative of physics that is not currently described by standard model. Chapter 8 gives a brief review of discrete symmetry tests using permanent EDMs, and chapter 9 describes why radium has an enhanced sensitivity to possible symmetry violations. In chapter 10, we report the experimental details for laser cooling and trapping of radium. We report in chapter 11 our measurement of the lifetime of the $7s6d\ ^1D_2$ atomic state of radium. Finally, we discuss our proposal for studies of the DC Stark shifts of radium in chapter 12.

Part I: Studies with Helium

CHAPTER 2

MOTIVATION FOR HELIUM NUCLEAR CHARGE RADIUS MEASUREMENTS

A fundamental property of each nucleus is its size. Like many of its other properties, this intimately depends on the nature of the forces that bind the nucleus together—the nuclear potential. An important task in nuclear physics is to understand the microscopic nature of this potential in terms of an appropriate basis. Describing the nucleus in terms of quarks and gluons would amount to solving QCD in the low energy and highly non-perturbative regime. Precise calculations of nuclear structure are currently unobtainable using QCD.

An alternative way of describing nuclei is in terms of nucleon-nucleon interactions. The force between nucleons arises from a residual strong interaction—much like the van der Waals force that exists between two electrically neutral atoms. The most precise nuclear models are the so - called *ab initio* microscopic theories that construct potentials based on bare nucleon-nucleon interactions, which are then used to solve the nuclear many-body problem. They are especially successful in describing the ($A \leq 10$) light nuclei. The experiments we describe in part I of this thesis report results for nuclear charge radii for the helium isotopes ^{6}He and ^{8}He. These serve as high precision checks for nuclear structure calculations–testing both the potentials used and the many-body methods employed.

2.1 Characterizing nuclear size

The spatial distribution of nucleons in a nucleus can be characterized by a root-mean square radius. Nuclear models often make the assumption of point-like nucleons. In reality though, these nucleons have a finite spatial extent which must be considered in characterizing the nuclear size. Depending on the kind of experiment performed, one is sensitive to the distribu-

tion of the protons predominantly, (such as scattering experiments using an electromagnetic probe) or to all of the nucleons (such as in experiments using a hadronic probe). We define below a number of nuclear radii expressed in terms of the ground state wavefunction of the nucleus Ψ_N. Ψ_N is a solution of the non-relativistic many body Schroedinger equation over all the nucleons in the nucleus.[1]

$$\mathbf{H}\ \Psi_N(r_i, r_2 \dots r_A) = E\ \Psi_N(r_i, r_2 \dots r_A) \tag{2.1}$$

In equation 2.1, r_i represents the set of all the coordinates (spatial, momentum, spin, isospin etc.) associated with each nucleon. The *ab initio* Hamiltonian is constructed as the sum of a kinetic energy K_i, two-body nucleon-nucleon potential v_{ij}, and a three-body potential v_{ijk} .

$$\mathbf{H} = \sum_{i}^{A} K_i + \sum_{i<j}^{A} v_{ij} + \sum_{i<j<k}^{A} v_{ijk} + \dots \tag{2.2}$$

In principle, one can envision N-body potentials, though in practice, modern potentials usually only go up to the three-body term.

Given the charge density distribution $\rho_c(r)$, the mean square charge radius is

$$\left\langle r^2 \right\rangle = \int r^2 \rho_c(r) d^3\mathbf{r} \tag{2.3}$$

where $\rho_c(r)$ is normalized by $\int d^3\mathbf{r}\rho_c(r) = Ze$

Now, as is often done in calculations of charge distributions, point-like nucleons are assumed. From [128], given the nuclear wavefunction, the point-proton density is

1. A non-relativistic treatment is justified because of the relatively low velocities of the nucleons in the nucleus. For example, the average kinetic energy of a nucleon is $\sim$ 50 MeV, which can be compared to its mass $\sim$ 1 GeV.

$$\rho_p(r) = \frac{1}{4\pi r^2} \left\langle \Psi_N \middle| \sum_i^A \frac{1+\tau_{iz}}{2} \delta(r - |\mathbf{r_i} - \mathbf{R_{cm}}|) \middle| \Psi_N \right\rangle \tag{2.4}$$

and likewise the point-proton RMS radius is

$$\left\langle r^2 \right\rangle = \int r^2 \rho_p(r) d^3\mathbf{r} \tag{2.5}$$

In equation 2.4, the $(1+\tau_{iz})/2$ term projects out the contribution from the protons. If no projector is used, we then have

$$\rho_N(r) = \frac{1}{4\pi r^2} \left\langle \Psi_N \middle| \sum_i^A \delta(r - |\mathbf{r_i} - \mathbf{R_{cm}}|) \middle| \Psi_N \right\rangle \tag{2.6}$$

which can be used to calculate the point-nucleon rms radius.

When the finite size of the nucleons is properly taken into account, we can relate r_c to the point proton radius by

$$\left\langle r_c^2 \right\rangle = \left\langle r_{pt}^2 \right\rangle + \left\langle R_p^2 \right\rangle + N/Z \left\langle R_n^2 \right\rangle + \frac{3}{4M_p^2} \tag{2.7}$$

where $N = A - Z$, and $\left\langle R_p^2 \right\rangle^{1/2}$ and $\left\langle R_n^2 \right\rangle^{1/2}$ are the root mean square charge radii of the proton and neutron respectively. The final term in equation 2.7 is the Darwin-Foldy correction to the proton radius [69].

As we mentioned above, we can test the quality of the nuclear potential as well as the approaches for solving the many-body Schroedinger equation by comparing theory results with experiment. We note that from the r^2 dependence of the operator, charge radii are particularly sensitive to the long-range parts of the nuclear wavefunction. We next consider the appropriate nuclear potential to use by starting from a two body nucleon-nucleon interaction.

2.2 Nucleon-Nucleon Interactions

Gross features of the two-body N-N potential can be surmised from *n*-*n*, *n*-*p* and *p*-*p* elastic scattering as well as from the properties of the deuteron [170]. There is a large library of results of N-N elastic scattering experiments performed over the years. Angular distributions, cross sections, polarizations, asymmetries and other observables have been determined at a variety of energies [167]. The Nijmegen database contains one such compilation [76], where the results of NN scattering are synthesized into a partial-wave analysis. The prevailing picture that emerges from the data is that among other things, the N-N potential has a strong repulsive core,it is spin and isospin dependent, and it is non-central. Under some conditions, depending on the relative angular momentum of the two nucleons, the potential is attractive. *Ab - inito* models are constructed to reflect this character.

The problem of the origin and nature of the nuclear force is a very old one. A particularly important idea that emerged was due to Yukawa [172], where he recognized that the short range of the strong nuclear force could be explained in an exchange picture where the exchanged particle has a mass which gives the nucleon-nucleon force a characteristic range that is inversely proportional to the mass of the exchanged particle, which in this case is the pion. The one pion exchange potential (OPEP) is an important component of all modern N-N potentials. The pion is the lightest meson, and the force due to the exchange of the pion leads to the long tail of the N-N potential. In general, one can consider the one-boson exchange potential, where a boson of mass m and coupling constant f is exchanged. In the case of the OPEP, the potential assumes the form

$$V_{OPEP} = \frac{1}{3}\frac{f^2}{\hbar c} m_\pi c^2 (\tau_1 \cdot \tau_2) \left[\sigma_1 \cdot \sigma_2 + S_{12}\left(1 + \frac{3}{\mu r} + \frac{3}{(\mu r)^2}\right)\right] \frac{\mathrm{e}^{-\mu r}}{\mu r} \tag{2.8}$$

The strength of the interaction is given by the coupling constant f for the $N \rightarrow N + \pi$ process. This can be determined for example from π - nucleon scattering. It is a measure of

the strength of a meson field surrounding a nucleon [27]. τ and σ are the isospin and spin of the nucleons and

$$S_{12} = 3(\sigma_1 \cdot \hat{r})(\sigma_2 \cdot \hat{r}) - \sigma_1 \cdot \sigma_2 \tag{2.9}$$

is a tensor operator. The masses of the exchanged pions are

$$m_{\pi^0} = 139.6\text{Mev}, \quad \mathrm{m}_{\pi^\pm} = 135.0\text{Mev}, \quad \mu \equiv \frac{\mathrm{m}_\pi \mathrm{c}}{\hbar} = 0.70(\text{fm})^{-1}, \quad \frac{\mathrm{f}^2}{\hbar \mathrm{c}} = 0.081. \tag{2.10}$$

The non-central character of the nuclear force is made evident in the OPEP; as represented by the tensor operator S_{12}.

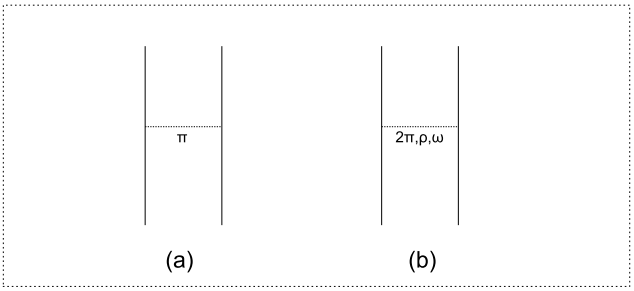

Figure 2.1: Feynman diagrams for N-N forces. (a) The OPEP which leads to the long range part of the force and (b) Two-Pion Exchange and the more general One-Boson exchange contribution which yield intermediate range contributions.

In constructing a modern N-N potential, the total two-body potential V can be expressed as the sum of an electromagnetic part V_{ij}^{γ}, an OPEP component V_{ij}^{π} and an intermediate range/repulsive core component V_{ij}^{R}

$$V_{ij} = V_{ij}^{\gamma} + V_{ij}^{\pi} + V_{ij}^{R} \tag{2.11}$$

The EM interaction is very well understood and is the significant isospin symmetry breaking part of the potential. The strong-interaction part of the potential, $V_{ij}^{\pi} + V_{ij}^{R}$, is the more

challenging part to construct. It, in addition, also has charge dependent (CD) and charge symmetry breaking (CSB) contributions. These are necessary for reproducing experimental results.

There are a number of widely used two-body nucleon nucleon potentials in the community. For example, there is a Reid and Nijmegen series [153], a Bonn series [104], a Paris series [99], an Argonne series [168] etc. An excellent review of the different potentials can be found in [167].

These models are all similar in that they are fit to the results of a partial wave analysis of a large dataset of N-N scattering. Also, the long range components are given by the OPEP. The potentials differ however in the manner they treat the intermediate and short range component. They also differ in the way the potential is expressed. While some of them are written in position space (r-space), others are written in momentum space (k-space). Furthermore, some are written with an operator structure, where the potential is expressed as a sum of operators, which are constructed in a manner that is manifestly allowed by all relevant symmetries. The terms that go into the expression of the potential are constrained to satisfy translational, rotational, Galilean symmetry, as well as invariance under time-reversal and parity [167]. For example, the Argonne series of potentials [167] are built up using an operator construct structure. Such a construction is well adapted to use in variational calculations. An alternative structure used is a partial-wave expansion. Here, the potential is specified separately in each $^{2S+1}L_J$ channel, as used for example in the Reid/Nijmegen series [153], and the Bonn series [104] of potentials. This approach typically leads to somewhat better fits to the data. However, by treating the partial waves independently, some non-locality is introduced [167]. Such a formulation is suited for Fadeev calculations of the many-body problem.

As noted in [167], a guiding principle in constructing N-N potentials is often to build the models in such a way as to optimize the accuracy with which they reproduce the two-body

data and the ease of use in many body calculations. Another goal, which might conflict with the first, is to elucidate the role of the sub-nucleon degrees of freedom in the N-N interaction. Depending on which of the goals above one is interested in, this will inform the manner in which the V_{ij}^R is constructed. In order to highlight the sub-nucleonic degrees of freedom, a 'meson-theoretic' approach is used, where, in addition to the OPEP, V_{ij}^R includes the exchange of various other massive bosons. This is the approach taken in the Bonn family of potentials. The Argonne family on the other hand treats V_{ij}^R more phenomenologically. We show some representative two-body potentials for a number of interaction channels in figure 2.2.

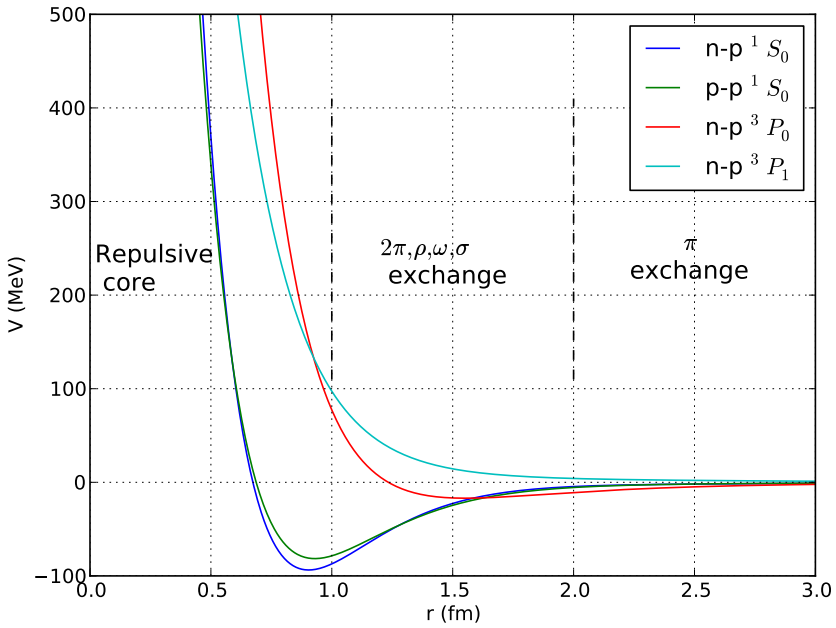

Figure 2.2: The potential between two nucleons as a function of separation between nucleons. The Reid93 Potential is plotted above, using the code published in [76]. We show some representative allowed channels. Some channels are forbidden on symmetry grounds. For example, low energy S-wave scattering, n-n or p-p can only occur in the singlet channel due to the Pauli exclusion principle.

We briefly describe here the Argonne v_{18} [168], the CD-Bonn potential [104] and the INOY potential [48]. These are quite representative of the available models. Moreover, they are of particular interest for our studies, as they have been used to calculate the charge radii of ^{6}He and ^{8}He. They also aim at addressing a common problem among many of these potentials, which is the issue of non-locality. The Bonn family of potentials are 'non-local' in the sense that the value of the potential at one point depends on the value of the wavefunction at a second point. The INOY (Inside non-local outside Yukawa) family of potentials are constructed in r-space such that the long-range part of the N-N interaction is well fit by the OPEP. The short-range behavior is treated phenomenologically in a manifestly non-local fashion. In doing so though, they are able to fit to properties of the three-nucleon systems the triton ^{3}H, and ^{3}He. Because the INOY potential is fit to A = 3 nuclei, the understanding is that some of the non-locality introduced is actually due to the three-nucleon interaction [126, 35].

The Av_{18} is the latest in the series of Argonne potentials formulated by R. Wiringa, S. Peiper and collaborators. It comprises of 18 operators with allowance made for charge dependent (CD) and charge symmetry breaking (CSB) terms. The hard core is treated phenomenologically. It is a local potential, formulated in r-space. It has 40 free parameters in total and is constrained by fitting to the deuteron binding energy, 1787 p-p and 2514 n-p elastic scattering data from 0 - 350 MeV. The total fitting is achieved with a χ^2 per datum of ~ 1.09. Details about the Argonne series of potentials in general, and the Argonne v_{18} in particular can be found in [168, 128, 125].

The CD-Bonn belongs to the family of Bonn potentials formulated by R. Machleidt [104]. They are meson theoretic in the sense that the long range potential is given by the OPEP. Intermediate potentials are given by exchange of heavier mesons, the ω-meson, the ρ meson, as well as a 'phenomenological' σ-meson. It is phenomenological in that it is a fictitious scalar boson of mass ~ 500 MeV, chosen to reproduce the intermediate range attraction of

the potential. As noted in [167], the microscopic source of this intermediate range attraction is believed to be due to two-pion exchange with the possible excitation of the intermediate nucleons to the Δ resonance. It is written in k-space and is non-local. Like the Av_{18}, it has nearly 40 free parameters and has been fit to the partial wave analysis from the Nijmegen group with a χ^2 per datum ~ 1.

2.2.1 Three-Body Forces

Once the two-nucleon potentials are obtained as described above, they can be used to solve the many-body Schroedinger equation for a nucleus with A-nucleons. Take for example the Argonne series of potentials, for which nuclear structure is performed with Quantum Monte Carlo techniques [127, 125, 126]. For nuclei with $A \geq 3$, the observation is that the gross features of the nuclear structure is reproduced. In particular, the correct ordering of the nuclear states is observed, and likewise the rapid saturation of nuclear binding energies above ^{4}He is reproduced . Notably though, with the exception of ^{2}H, other nuclei are under-bound. Some of the weakly bound nuclei are actually unbound to particle emission with only the two-nucleon potentials. This is shown in figure 2.4. Also, the two-nucleon calculations over-estimate the equilibrium nuclear densities [127]. This suggests that the potential used is incomplete and that it is important to augment the two-body potential with more terms. In particular, an additional attraction is needed in order to increase the binding energies. However, a short-range repulsive interaction is desired in order to maintain a saturated nuclear density to the experimental value [127].

In the meson exchange picture, there are a number of ways in generating a three-body interaction. These involve the exchange of 2-pions or 3-pions, along with a nucleon being in its excited state. In the lowest order, we can consider an s-wave 2-pion exchange interaction, and a p-wave 2-pion exchange interaction. Additionally, there are also 3-pion rings which

also lead to NNN forces. These are diagrammatically shown in figure 2.3 As in the case

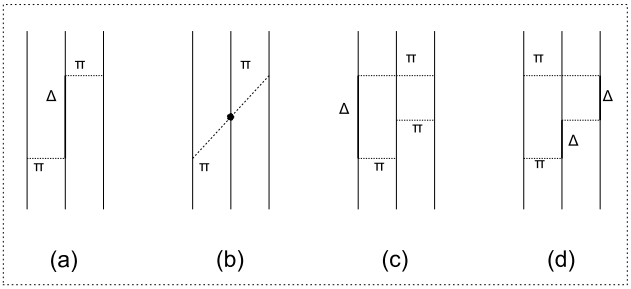

Figure 2.3: Three-nucleon forces. (a) The Fujita-Miyazawa three-body force [89].This arises from π-N scattering of the pion being exchanged between the 2 nucleons by a third nucleon via the p-wave Δ resonance. It leads to an attractive interaction. (b) This force arises from π-N S-wave scattering between the pion being exchanged by the two nucleons with a third partner. (c) and (d) are 3-pion rings, which rely on one of the nucleons being in the excited state

of the NN interactions, a number of modern NNN potentials have been developed. Some examples of those available in the community are the Tuscon-Melbourne family of potentials [43], the Brazil potential [41], the Illinois series [127]. They include a number of the diagrams shown in the figure 2.3, as well as possibly a phenomenological treatment of the short range. The Illinois series for example have a total of 5 free parameters, and are used (along with the Av_{18}) to fit the 17 lowest lying energy levels of the light nuclei. Results of only a NN potential augmented by the NNN potential are shown in figure 2.4.

As we mentioned above, without the NNN component of the *ab initio* potentials, nuclei with $A \geq 2$ are under bound. In particular, ^{6}He and ^{8}He are not bound at all with only the two-body NN interaction. This means that the excitation spectra of ^{6}He and ^{8}He, as well as other observables, such as their charge radii are sensitive to the three-nucleon potential.

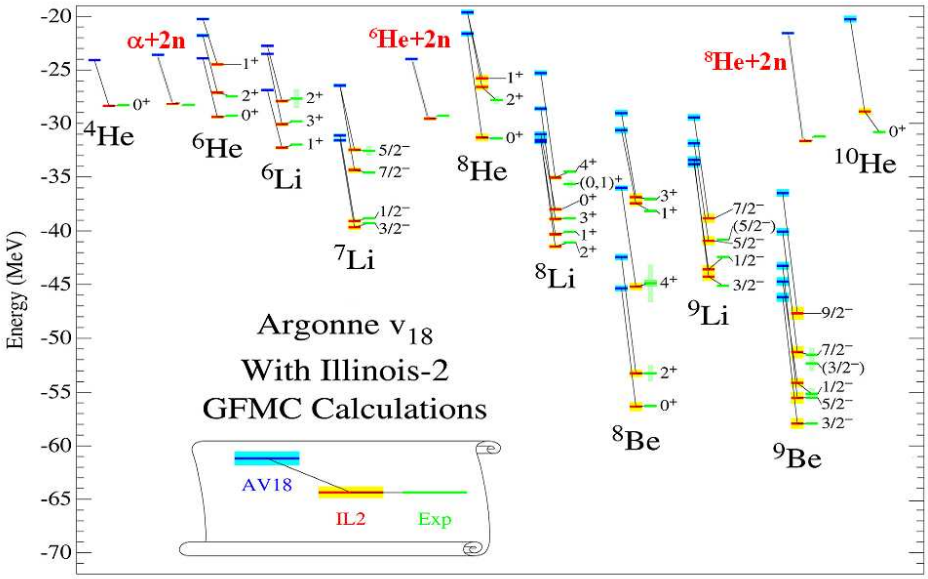

Figure 2.4: Nuclear levels of light isotopes calculated by GFMC using the AV18 + IL2 potentials. Using the AV18 which includes only a two-body force, we note that both ^{6}He and ^{8}He are not bound with respect to breakup into an alpha particle + 2n and ^{6}He + 2n. They are only bound when the three body force is applied. The width of the ^{1}0He resonance has been measured to be 300 keV. This corresponds to a half life of $\sim 10^{-21}$ s [119].

2.2.2 Many Body Calculations of Nuclear Structure

Once a high quality nuclear potential is constructed, the next task is to use it in the nuclear many-body Schroedinger equation. We briefly describe two approaches for solving the nuclear many-body problem which have been used to predict charge radii for the helium isotopes.

No Core Shell Model

The mean-field nuclear shell model is based on the idea that the nucleons are bound in an average potential provided by the other nucleons in the nucleus. Also, the nucleons exist in quantum states with definite angular momentum and parity. The sets of states with

the same angular momentum are, like in atomic physics, referred to as orbitals. States with filled orbitals are particularly tightly bound and form 'shells'. In many calculations, only the nucleons outside the closed shell are considered as active. Calculations can then be performed in significantly smaller Hilbert space which allows for the excitation of the valence nucleons. Although there is freedom in choosing which basis to use in representing the system, a harmonic oscillator basis is attractive due to its favorable algebraic structure, and also because harmonic oscillator eigenfunctions are good approximations of the single-particle wavefunctions in the mean field. Shell models with their varying degrees of sophistication are reviewed in [32].

The No Core Shell Model (NCSM) is an extension of this concept. In this approach, all the nucleons are 'active'. The strategy is to expand modern potentials, such as the Av_{18}, Nijemegen or CDBonn in a harmonic oscillator basis. By diagonalizing the Hamiltonian, one obtains energy levels as well as wavefunctions which can be used to determine expectation values of other observables. There is a dependence of the calculated value of an observable on the size of the model space used. Convergence studies must then be performed, whereby an observable is calculated as a function of the size of model space used. A good reference for the NCSM is [35].

Quantum Monte Carlo

Quantum Monte carlo refers to a class of techniques of solving the nuclear many-body problem where monte-carlo integration techniques are used. In the work of Wiringa and Pieper, the Variational Monte Carlo (VMC) scheme is used along with the Green's Function Monte Carlo (GFMC). The VMC method starts with the construction of a trial wavefunction of a specified angular momentum, parity and isospin $\Psi_v(J^\pi; T)$. As described in [128], given a trial wavefunction Ψ_v, the Metropolis monte-carlo integration method is used to evaluate

the expectation value $\langle\Psi_v|\, H\, |\Psi_v\rangle$. By the variational principle, this gives an upper bound on the energy of the ground state

$$E_V = \frac{\langle\Psi_v|\, H\, |\Psi_v\rangle}{\langle\Psi_v|\ \Psi_v\rangle} \geq E_0 \tag{2.12}$$

The parameters of Ψ_v are varied to minimize E_V. The resultant Ψ_v can then be used to calculate other properties as the expectation value of the appropriate operator, or some overlap integral in order to calculate state to state transition rates.

It turns out that the VMC alone does not lead to the lowest energy state. The GFMC scheme [128, 125, 126] can reach lower energies by taking Ψ_v as a starting wavefunction. It systematically projects out components of excited states which are still in the wavefunction Ψ_v. The idea is to project out the exact lowest energy state by evaluating

$$\Psi_0 = \lim_{t\to\infty} \exp[-(\mathrm{H} - \mathrm{E}_0)\tau]\Psi_\mathrm{v}, \tag{2.13}$$

As can be seen from equation 2.13, components of the wavefunction with energy substantially larger than E_0, are quickly suppressed. In the limit $t \to \infty$, this leads to the exact $\langle H\rangle$ [128].

Thus, by performing a GFMC integration of a wavefunction engineered to have a given spin and parity leads to a wavefunction of that state with energy minimized. The challenges in these studies is therefore to build better initial trial wavefunctions and to develop efficient algorithms for performing the monte-carlo integration. This has been applied to nuclei as large as A=12 [126].

Other approaches used in solving the nuclear many body problem for light nuclei are for example the Fadeev method [117], the stochastic variational method, coupled cluster approach, and the correlated hyperspherical harmonics [97]. In 2001, a benchmark test was

performed whereby a large number of the different many-body approaches were used to compute the properties of ^{4}He [93] using the same potential—the Av_8' NN interaction. The calculations of the binding energies and rms radii all agreed to within $\sim 2\%$.

2.2.3 ab initio Calculations for point-proton radii for Helium

We give below the predictions for the point-proton radii of the ^{6}He and ^{8}He isotopes using the NCSM method performed by Caurier and Navratil in [35], as well as with GFMC method by Pieper and Wiringa in [126].

Table 2.1: point-proton radii of $4, 6, 8$He in fm using *ab initio* potentials along with the NCSM [35] and GFMC [126] method. The potential used in each calculation is given in parenthesis.

	Experiment.	NCSM (CD-Bonn 2000)	NCSM (INOY)	GFMC (Argonne v_{18} + IL6)
^{4}He	1.455(1)	1.45(1)	1.37(1)	1.45(1)
^{6}He	1.912(8)	1.89(4)	1.76(3)	1.92(4)
^{8}He		1.88(6)	1.74(6)	1.82(2)

CHAPTER 3

EXPERIMENTAL PROBES OF NUCLEAR CHARGE RADII

There are a number of different experimental techniques for determining nuclear charge radii. In chapter 5, we will report our measurement of the charge radius of ^{6}He and ^{8}He using laser spectroscopy of trapped helium atoms. I will put our technique in context by describing some of the other common techniques for determining the charge distribution of nuclei—highlighting their strengths and limitations.

3.1 Electromagnetic probes of the charge distributions

3.1.1 Low energy elastic electron scattering

The majority of the charge radii of nuclei are determined by low energy elastic electron scattering [148].

For an incident electron beam with energy E which is scattered with an energy E′, the differential cross-section can be written in terms of the relativistic invariant $q^2 = 4\mathrm{EE}'\sin^2(\Theta/2)$. For a spin 1/2 nucleus, such as ^{3}He or the proton, we have:

$$\frac{d\sigma}{d\Omega}(E,\Theta) = \frac{(Z\alpha)^2 E'}{4E^3\sin^4(\Theta/2)}\left[A(q^2)\cos^2\left(\frac{\Theta}{2}\right) + \mathrm{B(q^2)}\sin^2\left(\frac{\Theta}{2}\right)\right] \tag{3.1}$$

$A(q^2)$ and $B(q^2)$ are structure functions which encode the deviation of the nucleus from the point scatterer. Another convenient way of describing the finite nuclear size contribution to the scattering cross section is in terms of the electric and magnetic form factors.

$$\begin{aligned} A(q^2) &= \frac{G_E^2(q^2) + (1+\kappa)^2\tau G_M^2(q^2)}{1+\tau} \\ B(q^2) &= 2\tau(1+\kappa)^2 G_M^2(q^2) \end{aligned} \tag{3.2}$$

where $\tau = q^2/4M^2$, κ is the anomalous magnetic moment of the nucleus, and $G_E(q^2)$ and $G_M(q^2)$ are the Sach's electric and magnetic form factors respectively. For a nucleus with no nuclear spin such as ^{4}He, the magnetic form factor, $G_M(q^2)$ vanishes, and the expression for the differential cross section reduces to

$$\frac{d\sigma}{d\Omega}(E,\Theta) = \frac{(Z\alpha)^2 E' \cos^2(\theta/2)}{4E^3 \sin^4(\Theta/2)} G_E^2(q^2) \tag{3.3}$$

In the Breit frame (i.e. the frame where the electron beam with initial momentum $\mathbf{p} = -\frac{Q}{2}$ is scattered to $\mathbf{p}' = +\frac{Q}{2}$), the electric form-factor $G_E(q^2)$, can be expressed as

$$G_E(q^2) = \int \rho_c(\mathbf{r}) e^{i\mathbf{q}\cdot\mathbf{r}} d^3\mathbf{r}. \tag{3.4}$$

$G_E(q^2)$ can be identified in equation 3.4 as the Fourier transform of the charge distribution. In the region of low momentum transfer q^2, equation 3.4 can be expanded to yield

$$\begin{aligned} G_E(q^2) &\approx \int \rho(\mathbf{r}) \left[1 + (i\mathbf{q}\cdot\mathbf{r}) + \frac{1}{2!}(i\mathbf{q}\cdot\mathbf{r})^2 + \frac{1}{3!}(i\mathbf{q}\cdot\mathbf{r})^3 + \ldots\right] d^3\mathbf{r} \\ &= \left[1 - \frac{q^2}{6}\left\langle r_c^2\right\rangle + \frac{q^4}{120}\left\langle r_c^4\right\rangle + \ldots\right] \end{aligned} \tag{3.5}$$

where the mean square charge radius is

$$\left\langle r^2\right\rangle = \int r^2 \rho(\mathbf{r}) d^3\mathbf{r}. \tag{3.6}$$

It is therefore evident that, to the extent that $G_E(q^2)$ can be determined at low q^2, the rms radius of the nucleus can be extracted. The charge radii of many nuclei have been determined in this manner [84]. A key result of the electron scattering studies of charge distributions is shown in figure 3.1. A survey of the charge distribution of nuclei with different masses led to the qualitative observation that the distributions for many nuclei could be represented by

the Fermi form with two parameters:

$$\rho(r) = \frac{\rho(0)}{1 + e^{(r-R)/a}} \tag{3.7}$$

where $\rho(0)$ is the approximate central density, R is the half density radius, and a is the surface thickness parameter. This is shown on the left panel of figure 3.1.

From a survey of the charge radii of a number of nuclei, the following observations can be made:

1 $R \sim r_0 A^{1/3}$, with $r_0 \sim 1.25$ fm, for a broad range of nuclei. This scaling suggests a roughly constant density of nuclear matter. This supports the idea that the nucleus is an incompressible fluid of tightly packed nucleons.

2 The surface diffuseness $a \sim 2.4 \pm 0.3 \times 10^{-13}$ cm for a large range of nuclei.

We note here that ^{6}He and ^{8}He belong to a class of nuclei with mass distributions that do not follow this general trend. They are so called 'halo nuclei'—and are characterized by rather large spatial extent of their neutron wavefunctions [4].

In electron-Nucleus scattering described above, the EM interaction is dominant. Notably though, the electrons also interact through the weak interaction. For example, Parity-Violating electron scattering can be used to study the weak interaction between the nucleus and the electrons. At low momentum transfer, the Z boson couples predominantly to the neutron. Hence, by measuring Parity violating cross sections from electron-nucleus scattering, one can determine the neutron distribution in the nucleus. This is for example the aim of the ^{208}Pb Radius Experiment "PREX" which is scheduled to be performed at Jefferson Laboratory [86, 133].

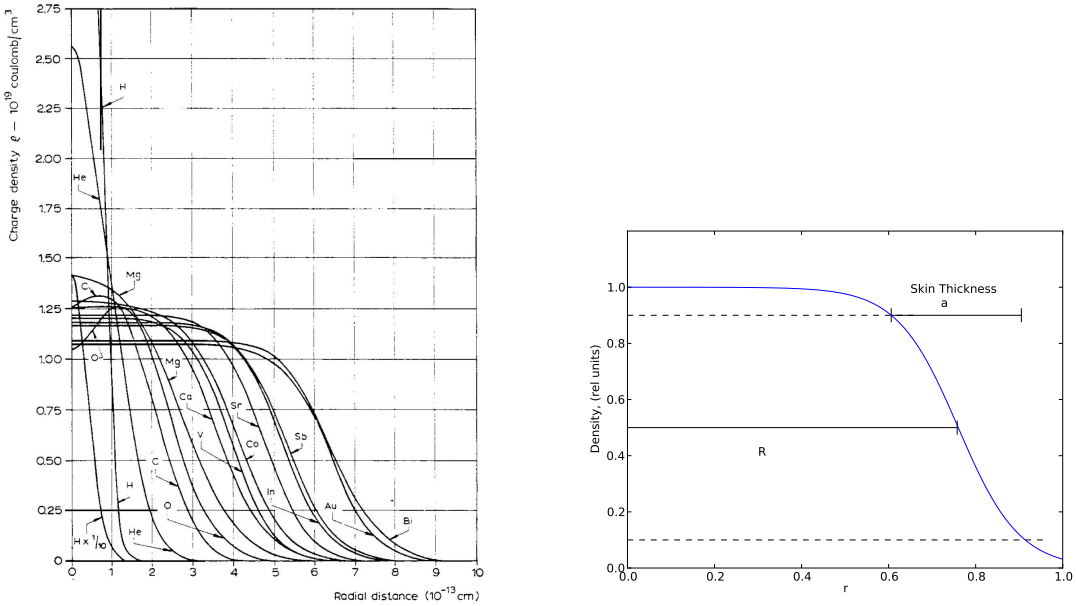

Figure 3.1: Charge density distribution for a number of different nuclei obtained by electron scattering. General shape of distribution resembles a Thomas Fermi form. Figure on left obtained from [83]

3.1.2 Atomic and Muonic Atom Spectroscopy

Another class of electromagnetic probes of charge distributions in nuclei is atomic and muonic atom spectroscopy. Here, the bound leptons (electrons or muons) are used as a probe of the nucleus. We first consider the case of a bound electron. The main idea is that for a bound electron, there is a non-zero probability of its being in the nuclear volume. This probability is particularly high for an electron in an S orbital. Consequently, the potential that it samples is not simply a Coulomb potential due to a point charge. Consider for example an atom with an electronic wavefunction ψ_n, and a nuclear radius R. Assuming that the wavefunction of the electron is constant in the nuclear volume, we can separate the energy of the state as:

$$E_n = \int_{r<R} \psi_n^* V' \psi_n dv + \int_{r>R} \psi_n^* V \psi_n dv. \tag{3.8}$$

where V is the $\sim 1/r$ Coulomb potential due to a point charge , and V' is the modified potential felt by the electron when it is in the nuclear volume when $r < R$ The point nucleus value can be readily calculated, and the energy of the transition measured experimentally. Deviations of E_n from the point nucleus value yield information about R and the charge distribution in the nucleus. A natural scale that governs the extent to which the electron wavefunction probes the nucleus is the ratio $R/a_0 \sim 10^{-5}$, where a_0 is the Bohr radius–a typical electron orbit size. This implies that the contribution to E_n due to finite nuclear size effects is of that order. In order to use this method to determine R therefore, the electronic wavefunctions must be known to high precision.

Optical and X-Ray electronic transitions have been used successfully in obtaining nuclear size parameters for a variety of nuclei using this method. By considering the deviation from the point nucleus approximation in the *isotope shift* of a particular transition, the sensitivity to uncertainties in the electronic wavefunctions can be minimized. We make use of this method in our studies of ^{8}He and ^{6}He, and will describe it in more detail in chapter 4

Muonic atoms are formed by substituting one of the bound electrons with a muon. A muon is captured by an atom in a high lying Rydberg level and eventually cascades down to the innermost electron orbit. The capture and cascade take $\sim 10^{-12} - 10^{-9}$s, while the lifetime of the muon is $\sim 2.2 \times 10^{-6}$s. As such the muon spends most of its lifetime bound to the nucleus [122]. Because of the difference in mass ($m_\mu/m_e = 207$), the orbit of the bound muon is correspondingly ~ 200 times smaller, and the deviation of the energy of the bound muon from that calculated using the point nucleus is correspondingly four orders of magnitude larger. This method has proved to be rather successful, and has been used to determine charge radii of a variety of nuclei [63]. A recent result for the determination of the proton charge radius using muonic hydrogen is particularly interesting [129] because it is more precise than other determinations of the rms proton radius—but yet is 5 standard deviations away from the particle data group value. As of now, there is not yet a resolution

for this discrepancy. An obvious disadvantage of muonic atom spectroscopy is that it can only be performed in a facility with muons, and one must overcome the technical difficulties of the short muon half life. A nice review for muonic atoms is [29].

3.2 Hadronic probes of charge distributions

Hadronic probes can also be used to probe the size of nuclei and to determine their mass and charge distributions. In these experiments, the strong interaction is the source of the scattering potential. Now, because the strong force has a short range, the projectile must be able to come sufficiently close to the target nucleus in order to interact. To do so, the energy of the collision must be large enough to overcome the coulomb repulsion. One can envision experiments for α-nucleus scattering, p-nucleus, π - nucleus, nucleus-nucleus scattering etc. In a manner similar to the EM case, one can measure an interaction cross section and then determine a nuclear size from the form factors determined from cross section measurements. In general, hadronic probes yield values for so called matter radii, as they are sensitive for interactions between the projectile and the target neutrons and protons–with no discrimination (to the extent that isospin symmetry holds).

For the isotopes of helium, an important set of experiments were performed in 1992 by Tanihata *et al.* [158] at Berkeley. They performed their experiment in inverse kinematics, whereby they used a radioactive beam of helium to scatter off of a fixed carbon target in order to determine the interaction cross sections σ_I. From these cross-sections, they were able to determine the nuclear matter radii. Their results for σ_I as well as the 2-neutron and 4-neutron removal cross sections are reproduced in table 3.2.

The general observation of their studies is that the interaction cross section increases as

Table 3.1: Measured interaction cross sections; reproduced from [158]

Reaction	Cross section (mb)		
	σ_I	σ_{-2n}	σ_{-4n}
^{4}He + C	503 ± 5	-	-
^{6}He + C	722 ± 5	189 ± 14	-
^{8}He + C	817 ± 6	202 ± 17	95 ± 9

one goes from mass 4 to 6 to 8. Furthermore,

$$\begin{aligned} \sigma_I(^6He) - \sigma_I(^4He) &\sim \sigma_{-2n}(^4He) \\ \sigma_I(^8He) - \sigma_I(^4He) &\sim \sigma_{-2n}(^8He) + \sigma_{-4n}(^8He) \end{aligned} \tag{3.9}$$

The relations in equation 3.9 suggested that one could think of ^{6}He and ^{8}He as being comprised of a ^{4}He core surrounded by 2 and 4 neutrons respectively.

Alkhazov *et al.* [5] in 1997, also studied these nuclei. Their experiment was similarly performed in inverse kinematics at GSI, where radioactive beams of helium isotopes of energies between 674 and 717 Mev/u were made to scatter off of a proton (hydrogen) target. The target was in the form of a hydrogen filled ionization chamber. It therefore also served as a recoil detector—yielding excellent acceptance. They reported matter radii $R_m(^6\text{He}) = 2.30 \pm 0.07$ fm, and $R_m(^8\text{He}) = 2.45 \pm 0.07$ fm [5].

The results of Tanihata *et. al* [158] and Alkhazov *et al.* [5] are consistent with the picture that ^{6}He and ^{8}He are halo nuclei. That is, they are weakly bound systems which consist of an alpha-particle core, surrounded by two and four loosely bound neutrons respectively. Because the additional neutrons are loosely bound, they are very spatially diffuse, and form a halo as it were. Such weakly bound systems are particularly challenging for nuclear structure calculations. Moreover, theories usually calculate the point-nucleon distributions. Derivation of radii from the measured cross sections depends on models of nucleon distributions and

Table 3.2: Experimentally determined charge radii in fm for the proton and the isotopes of helium. There are plans to perform improved muonic helium spectroscopy which will provide values for ^{3}He and ^{4}He charge radii [10].

		Elastic e^- scattering	μ-atom Spectroscopy	Atomic spectroscopy
$\langle r^2 \rangle^{1/2}$ (fm)	p	0.8772(46) [174]	0.8418(7) [129]	0.883(14) [107]
	^{3}He	1.959(30)[8]	-	1.9506(14)[147]
	^{4}He	1.681(4)[149]	1.673(1)[28]	-
	^{6}He	-	-	2.061(8)[165, 31]
	^{8}He	-	-	1.955(17)[114, 31]

interactions. This model dependence introduces additional uncertainties when comparing with theory. A nuclear model independent determination of the charge radius using methods of atomic or muonic atom spectroscopy is therefore advantageous.

CHAPTER 4

NUCLEAR SIZE OF HELIUM FROM ISOTOPE SHIFT—ATOMIC THEORY

Helium has been an important test case for the application of quantum mechanics in describing atomic structure. Unlike hydrogen, there is no analytical solution to the non-relativistic Schroedinger equation. Approximation techniques must be applied in order to account for the few-body and consequently non-separable nature of the system. In order to test the calculations of atomic structure, precise experiments must be performed.

Currently, the most precise helium atomic structure calculations are performed by Gordon Drake and collaborators, as well as Krzysztof Pachucki, Jonathan Saperstein and collaborators. In Drake's work, the starting point for the calculation is the non-relativistic Hamiltonian of the form [49]:

$$H = \frac{\hbar^2}{2M}\nabla_X^2 - \frac{\hbar^2}{2m}\nabla_{x1}^2 - \frac{\hbar^2}{2m}\nabla_{x2}^2 - \frac{Ze^2}{|\mathbf{X}-\mathbf{x_1}|} - \frac{Ze^2}{|\mathbf{X}-\mathbf{x_2}|} + \frac{e^2}{|\mathbf{x_1}-\mathbf{x_2}|} \tag{4.1}$$

where M is the mass of the nucleus, m, the mass of the electrons. $\mathbf{X}$, $\mathbf{x_1}$ and $\mathbf{x_2}$ refer to the coordinates of the nucleus and the two electrons respectively. Transforming to the center of mass and relative coordinate,

$$\begin{aligned} \mathbf{r1} &= \mathbf{x_1} - \mathbf{X} \\ \mathbf{r2} &= \mathbf{x_2} - \mathbf{X} \\ \mathbf{R} &= \frac{M\mathbf{X} + m\mathbf{x_1} + m\mathbf{x_2}}{M+2m} \\ \mathbf{r_{12}} &= \mathbf{r_1} - \mathbf{r_2} \end{aligned} \tag{4.2}$$

they obtain and expression for the Hamiltonian

$$H = -\frac{\hbar^2}{2\mu}\nabla^2_{r_1} - \frac{\hbar^2}{2\mu}\nabla^2_{r_2} - \frac{\hbar^2}{M}\nabla_{r_1}\cdot\nabla_{r_2} - \frac{Ze^2}{\mathbf{r_1}} - \frac{Ze^2}{\mathbf{r_2}} + \frac{e^2}{\mathbf{r_{12}}} \tag{4.3}$$

Thus, the non-relativistic Schroedinger equation for the helium atom is of the form

$$\left[-\frac{1}{2}\nabla^2_1 - \frac{1}{2}\nabla^2_2 - \frac{Z}{r_1} - \frac{Z}{r_2} + \frac{1}{r_{12}} - \frac{\mu}{M}\nabla_1\cdot\nabla_2\right]\psi = E\psi \tag{4.4}$$

Writing the Hamiltonian as in equation 4.3 is desirable because the Hamiltonian for an infinitely heavy nucleus retains this form except for the appearance of the additional 'mass polarization' term $\frac{\mu}{M}\nabla_1\cdot\ \nabla_2$ which appears for a nucleus of non-infinite mass. The mass ratio therefore appears as a natural expansion parameter [53].

The Schroedinger equation given in equation 4.4 is solved variationally, by writing a trial wavefunction in Hylleraas coordinates. As Drake *et al.* report, ground state energies which are "*accurate to one part in* 10^{20}*, can be obtained for helium and matrix elements for other corrections such as relativistic corrections, converge to about half as many figures*" [53].

Thereafter, additional contributions to the energy levels are added in perturbation theory. The total energy of an atomic state is given by an expansion in terms of the fine structure constant:

$$E_{\rm tot} = E_{\rm nr} + \alpha^2 E_{\rm rel} + \alpha^3 E_{\rm QED} + \ldots + E_{\rm nuc} \tag{4.5}$$

where $E_{\rm nr}$ is the non-relativistic energy, $E_{\rm rel}$, the leading relativistic correction, and $E_{\rm QED}$ the leading QED correction [53]. Each of the above contributions to the total energy can

Table 4.1: Terms added to the non-relativistic Hamiltonian perturbatively and their relative orders of magnitude in terms of Z (from [49]). For ^{4}He, $\mu/M = 1.370745624 \times 10^{-4}$ and $\alpha^2 = 0.5325135450 \times 10^{-4}$

Contribution	Magnitude	Rel. Value
Non-relativistic energy	Z^2	1
Relativistic corrections	$Z^4\alpha^2$	10^{-3}
Mass polarization	$Z^2\mu/M$	10^{-4}
Anomalous magnetic moment	$Z^4\alpha^3$	10^{-5}
QED correction(Lamb Shift)	$Z^4\alpha^3(\ln\alpha) + \ldots$	10^{-5}
Relativistic recoil	$Z^4\alpha^2\mu/M$	10^{-6}
Second-order mass polarization	$Z^2(\mu/M)^2$	10^{-8}
Finite nuclear size	$Z^4\left\langle \bar{r}_c/a_0\right\rangle^2$	10^{-9}

also be expanded in terms of the mass ratio μ/M in the form:

$$\begin{aligned} E_{\rm nr} &= E^{(0)}_{\rm nr} + \frac{\mu}{M}E^{(1)}_{\rm nr} + \left(\frac{\mu}{M}\right)^2 E^{(2)}_{\rm nr} + \ldots \\ E_{\rm rel} &= E^{(0)}_{\rm rel} + \frac{\mu}{M}E^{(1)}_{\rm rel} + \ldots \\ E_{\rm QED} &= E^{(0)}_{\rm QED} + \frac{\mu}{M}E^{(1)}_{\rm QED} + \ldots \end{aligned} \tag{4.6}$$

4.1 Finite Nuclear Size Effects

In table 4.1, we reproduce from [49] the different terms which contribute to the energies of the bound states of helium. As discussed above, the mass polarization term has to do with the fact that the nucleus is not infinitely heavy. Relativistic corrections account for such interactions as spin-orbit, spin-spin, spin-other orbit etc. As a result, these corrections to the energy lead to the fine structure in the spectra of atomic states. The accuracy of the relativistic corrections can be tested by precise measurements of the fine structure intervals.

This has been done for example for ^{4}He on the 3P manifold in our group by Mueller *et al.* [115] as well as in our present work for ^{6}He in [114]

If all the terms which are larger than the finite nuclear size effects are well under control (i.e. calculable to precision greater than the finite nuclear size contribution), then a precision spectroscopy measurement can be turned around to extract the contribution due to the nuclear size. The energy difference of a particular transition in two isotopes a, and b of the same element yields the isotope shift $\Delta E(a-b)$. From equations 4.5 and 4.6, we note the the isotope shift can be written as

$$\begin{aligned}\Delta E(a-b) = &\left[\left(\frac{\mu}{M}\right)_a - \left(\frac{\mu}{M}\right)_b\right]\left(E^{(1)}_{\rm nr} + \alpha^2 E^{(1)}_{rel} + \alpha^3 E^{(1)}_{QED}\right) \\ &+ \left[\left(\frac{\mu}{M}\right)^2_a - \left(\frac{\mu}{M}\right)^2_b\right] E^{(2)}_{\rm nr} + \ldots + (E_{\rm nuc,a} - E_{\rm nuc,b}) + \ldots\end{aligned} \tag{4.7}$$

From equation 4.7, we see that the difference in finite nuclear size terms $(E_{\rm nuc,a} - E_{\rm nuc,b})$ can be determined if the other terms on the RHS of 4.7 can be calculated with sufficient accuracy. Subtracting the calculated terms then from the measured isotope shift leaves the finite nuclear size contributions.

In the case of the helium isotopes, This procedure is possible because the mass independent QED correction term $\alpha^3 E^{(0)}_{\rm QED}$ (from equation 4.6) cancels in the isotope shift, as it is independent of mass and therefore common to all isotopes. The remaining QED term, $\frac{\mu}{M}\alpha^3 E^{(1)}_{\rm QED}$ can be calculated to sufficient accuracy [53]. By sufficient here, we mean that the uncertainty on that contribution is much smaller than the size of the finite nuclear size contribution to the transition energy.

As discussed in [17, 49] and other places, the finite nuclear size correction for low-Z atoms can be expressed as,

$$\frac{2\pi Z e^2}{3}\left|\psi(0)\right|^2 \left\langle r^2 \right\rangle \tag{4.8}$$

This dependence can be easily shown by considering the electrostatic energy of a an electron with wavefunction $\psi(r)$ around a nucleus with a charge distribution $\rho(r)$. Now, assuming that the electron is in an S-state it has substantial spatial overlap with the nucleus. Because the spatial extent of the electron wavefunction is so much larger than the typical scale in the nucleus, i.e. $a_0 >> R_N$, the electron wavefunction can be assumed to be constant, $\psi(0)$, within the volume of the nucleus. As a result, the electrostatic energy of the interacting charges can be obtained, using Gauss' law to be the following:

$$E = \int \rho(r) V(r) d^3r \tag{4.9}$$

where

$$V(r) = -2\pi e \left|\psi(0)\right|^2 (R_N^2 - r^2/3) \;\; \text{for} \left|\mathrm{r}\right| < \mathrm{R_N} \tag{4.10}$$

Thus,

$$\begin{aligned} E &= \int\limits_{|r|<R_N} \rho(r)\{-2\pi e \left|\psi(0)\right|^2 (R_N^2 - r^2/3)\} d^3r \\ &= V(0) \int\limits_{|r|<R_N} \rho(r) d^3r + \frac{2\pi e}{3} \int\limits_{|r|<R_N} r^2 \rho(r) d^3r \end{aligned} \tag{4.11}$$

Making use of the equations:

$$\begin{aligned} \int\limits_{|r|<R_N} \rho(r) d^3r &= Ze \\ \int\limits_{|r|<R_N} r^2 \rho(r) d^3r &= Ze \left\langle r_c^2 \right\rangle \end{aligned} \tag{4.12}$$

we get

$$E = ZeV(0) + \frac{2\pi}{3} Ze^2 \left|\psi(0)\right|^2 \left\langle r_c^2 \right\rangle \tag{4.13}$$

where the first term represents the interaction between an electron and a point-like nucleus. The second term is the finite size correction. It is important to note that in the above derivation, the only assumption made was that the electron wavefunction $\psi(0)$ was constant over the volume of the nucleus. No particular form of the nuclear charge distribution $\rho(r)$ was assumed.

Table 4.2: Calculated Isotope Shifts between ^{6}He and ^{4}He and between ^{8}He and ^{4}He for the 2^3S_1 to 3^3P_J transition at 389 nm [52]. The theoretical uncertainty in the ^{8}He and ^{6}He mass shift determination come from the uncertainty in the mass of the respective nuclei. These reported values make use of the masses in [12] for ^{6}He and [142] for ^{8}He.

^{6}He - ^{4}He
$J = 0: \quad \delta\nu_{6,4} = 43196.157(1)\ \text{MHz} + 1.008\,(\langle r^2\rangle_4 - \langle r^2\rangle_6)\ \text{MHz/fm}^2$
$J = 1: \quad \delta\nu_{6,4} = 43195.897(1)\ \text{MHz} + 1.008\,(\langle r^2\rangle_4 - \langle r^2\rangle_6)\ \text{MHz/fm}^2$
$J = 2: \quad \delta\nu_{6,4} = 43196.171(1)\ \text{MHz} + 1.008\,(\langle r^2\rangle_4 - \langle r^2\rangle_6)\ \text{MHz/fm}^2$

^{8}He - ^{4}He
$J = 0: \quad \delta\nu_{8,4} = 64702.489(1)\ \text{MHz} + 1.008\,(\langle r^2\rangle_4 - \langle r^2\rangle_8)\ \text{MHz/fm}^2$
$J = 1: \quad \delta\nu_{8,4} = 64702.098(1)\ \text{MHz} + 1.008\,(\langle r^2\rangle_4 - \langle r^2\rangle_8)\ \text{MHz/fm}^2$
$J = 2: \quad \delta\nu_{8,4} = 64702.509(1)\ \text{MHz} + 1.008\,(\langle r^2\rangle_4 - \langle r^2\rangle_8)\ \text{MHz/fm}^2$

Condensing all the mass dependent terms in equation 4.7 into a single term, the "Mass shift" (MS), and the finite nuclear size terms into a "Field Shift", ($K_{\text{FS}}\delta\langle r^2\rangle$), we can express the isotope shift between two isotopes as:

$$\delta\nu_{a,b} = MS + K_{\text{FS}}\delta\langle r^2\rangle \tag{4.14}$$

where, $\delta\langle r^2\rangle$ is the difference in RMS charge radius between isotopes a and b.

For our experiment, which will be described in chapter 5, we determined the ^{6}He - ^{4}He

and ^{8}He - ^{4}He isotope shift for transitions between 2^3S_1 to 3^3P_J, with $J = 0, 1, 2$ at 389 nm. The Mass shifts were calculated by Drake *et al.* to be roughly 43 GHz and 64 GHz for ^{6}He-^{4}He and ^{8}He-^{4}He respectively. The field shifts, on the other hand, are on the order of a few MHz. The exact values determined for different transitions are reported in table 4.2.

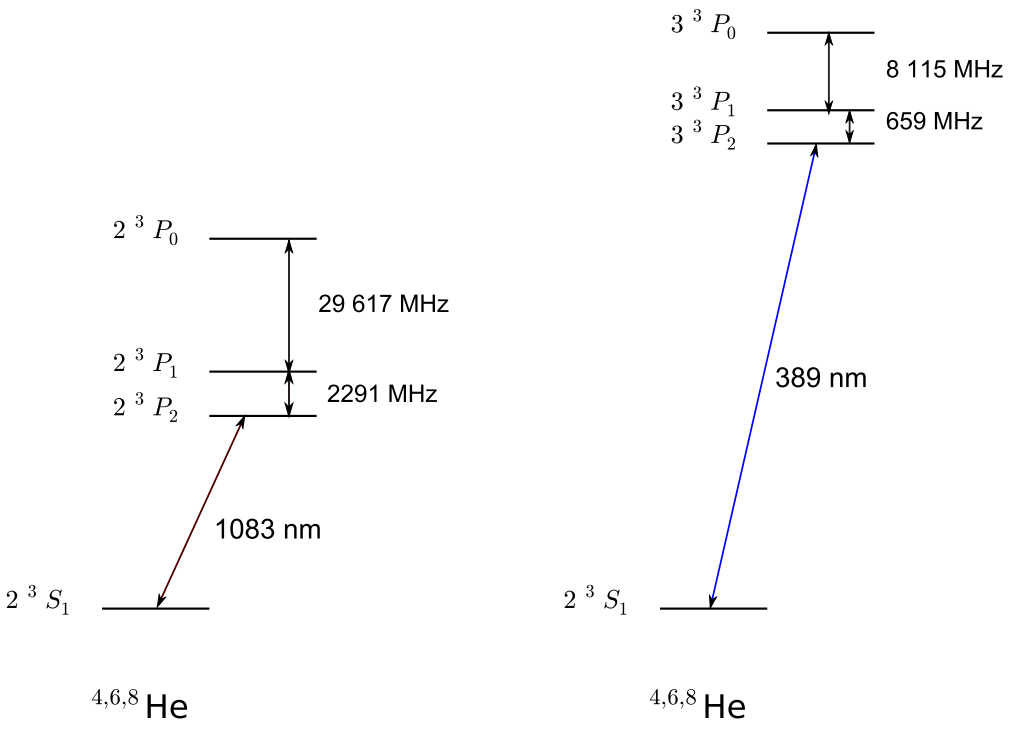

Figure 4.1: Level Scheme for Helium atoms showing the metastable state 2^3S_1, the 2^3P and the 3^3P manifold of states.(Not to scale). The fine structure splittings for ^{4}He to the nearest MHz calculated by Drake *et al* [52] are given.

CHAPTER 5

LASER SPECTROSCOPIC DETERMINATION OF THE CHARGE RADIUS OF HELIUM 8

In chapter 4, we described how an atomic isotope shift measurement can be used to make a sensitive determination of the charge radius of an isotope of interest. In this chapter, we will describe the details of our experiment for doing just that in ^{6}He and ^{8}He. We aim at measuring the isotope shift of ^{8}He - ^{4}He and ^{6}He - ^{4}He on the 2^3S_1 to 3^3P_2 transition. Measuring the isotope shift with an error of 100kHz would allow for the determination of the RMS charge radius with a fractional uncertainty of 1%. In order to perform this experiment, we must start by finding adequate supplies of ^{6}He and ^{8}He.

5.1 Production and transport of ^{6}He and ^{8}He

The ^{6}He and ^{8}He atoms used for our experiment were produced at GANIL, the Grand Acceleratueur National d'Ion Lourdes, in Caen, France. We collaborated with A. Villari *et al.* at GANIL. Part of their research involves developing intense radioactive beams for nuclear physics. The GANIL facility consists of five coupled cyclotrons (see figure 5.1). CSS1 and CSS2 together can be used to accelerate a primary stable beam up to energies of 95 MeV/u [36]. Typically a radioactive beam is generated by colliding the primary beam from CSS2 on a fixed target and re-accelerating a radioactive beam thereafter with CIME.

Since we desired a low energy beam of ^{8}He and ^{6}He, the beam emerging from CSS2 was directly sent to SIRA (figure 5.1). There, the ^{13}C primary beam with energy 75 MeV/u and 0.4 pμA was delivered to the Nanogan-III Target and ion source system. On colliding with the ^{12}C target in Nanogan-III, many radioactive isotopes are produced by fragmentation reactions. In particular, ^{6}He and ^{8}He nuclei were produced with rates of 1×10^8 s^{-1} and

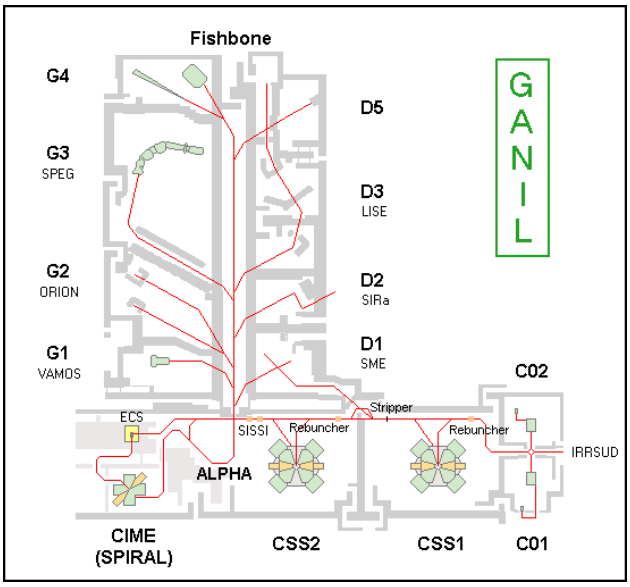

Figure 5.1: Schematic showing the general layout of the GANIL facility. Our experiment was located in the experimental hall outside SIRa. Image obtained from [36]

.

5×10^5 s^{-1} [100, 162].

Because helium is a noble gas, the atoms diffuse out of the porous graphite target quickly, and effuse into the adjacent ECR ion source. The carbon target was heated to $\sim 200 \circ C$, which accelerated the diffusion process out. It is estimated that the characteristic time for the helium atoms to leave the target was $\sim 250ms$. Once in the ECR source, the helium atoms are ionized, predominantly to the 1^+ state, and then transported as a 20 keV ion beam to a mass separator, which selects between ^{6}He and ^{8}He. It was this ion beam that was delivered to the experimental hall D2. A general schematic of the major components in the accelerator beam line is shown in figure 5.2.

Since we desired to perform spectroscopy on neutral atoms, we passed the ions delivered from the ECR source through a thin graphite foil. The ions were quickly neutralized, and the neutral atoms diffused out of the graphite. The foil was heated to $\sim 600^\circ$ C to accelerate the diffusion process.The released atoms were pumped into the atomic beam apparatus within

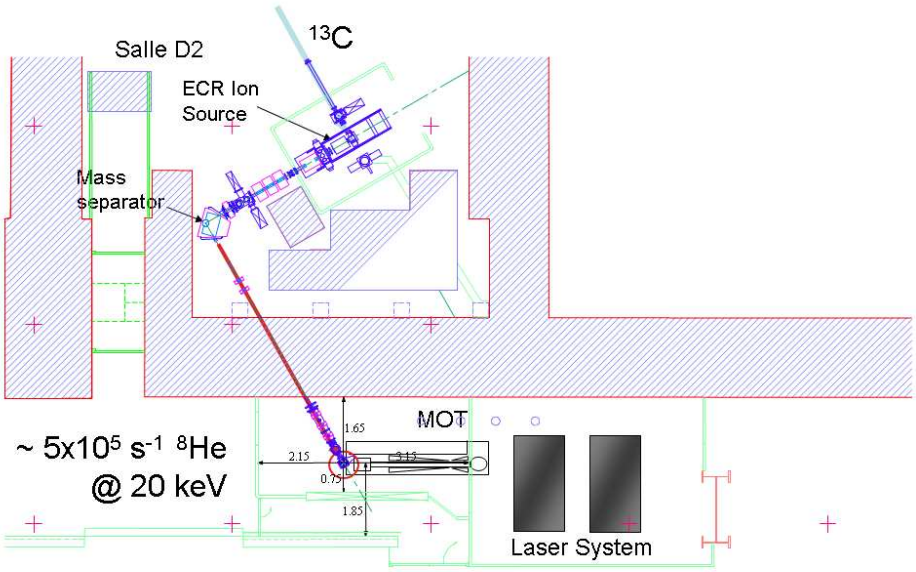

Figure 5.2: Schematic showing layout of atomic beam line relative to the ion transport infrastructure after the ECR source.

250 ms with rates of approximately $5 \times 10^7 s^{-1}$ and $1 \times 10^5 s^{-1}$ for ^{6}He and ^{8}He respectively. A schematic of the atomic beam layout is shown in figure 5.3.

5.2 Laser manipulation of neutral helium atoms

We make use of an atom-trap apparatus to first stop and hold the atoms before performing spectroscopy on them. The atoms are slowed down using a Zeeman slower, and trapped in a magneto-optical trap. These work on standard laser cooling principles and are treated in [108, 65].

In manipulating neutral helium (and other noble gas) atoms with lasers, there is the challenge that one can not perform laser cooling on ground state atoms because transitions from the ground state requires light of very short wavelengths. However, it is possible to

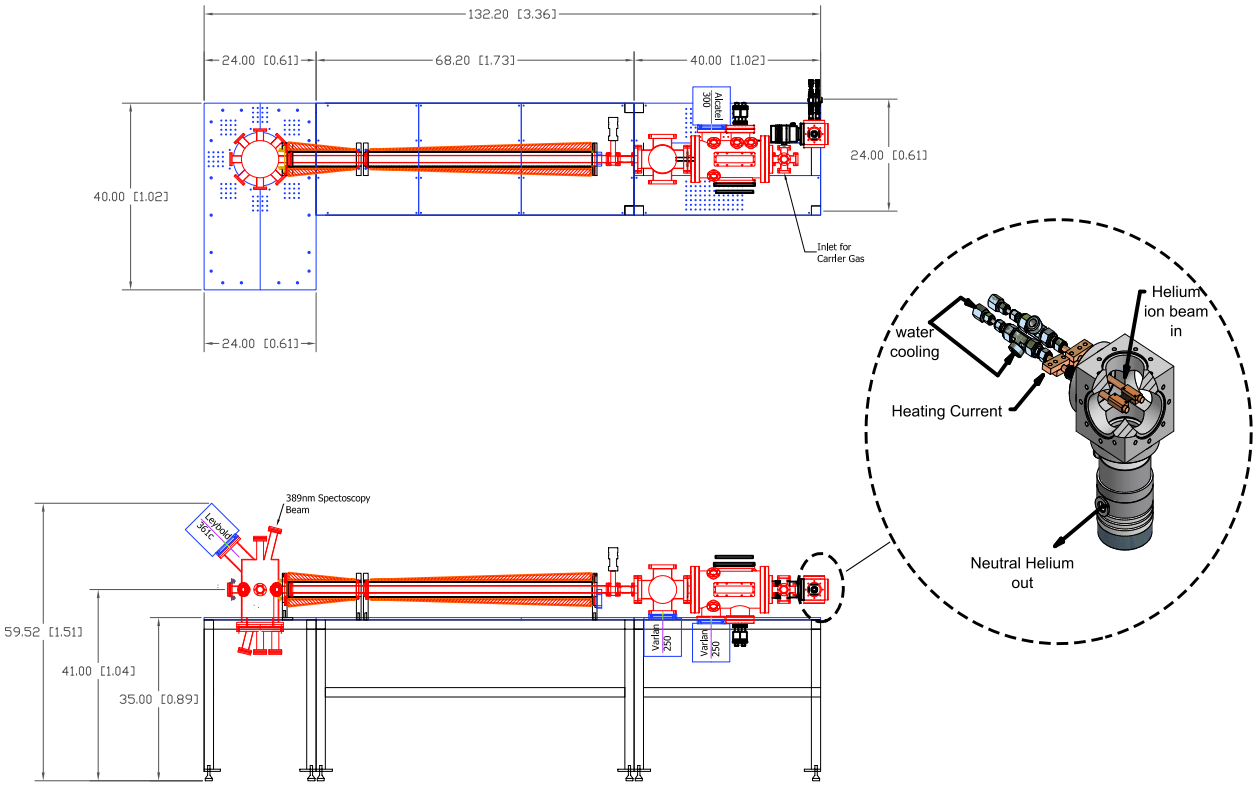

Figure 5.3: Helium atomic beam layout showing the major parts of the vacuum system. Neutralizer graphite foil is also shown.

laser cool the atoms once they are in the long lived metastable state.

For our experiment, high efficiency of trapping is of paramount importance because the rates of ^{8}He production are so low. We describe below the various sections of the apparatus—each of which is optimized to maximize the loading rate of atoms into the MOT.

5.2.1 metastable source

Noble gas atoms in the metastable state are amenable to laser cooling and trapping because of the accessibility of closed transitions at attainable laser wavelengths from the metastable state. They have been used in a number of different experimental setups ranging from trace analysis [37], Bose - Einstein condensation [42], studies of cold collisions, [102], atom

lithography [6] and studies of Bose-Fermi statistics using Hanbury-Brown Twiss experiments with atoms [144].

For all these studies, it is important to have an efficient way of populating the metastable 2^3S_1 state. Most groups use either DC or RF discharges. We make use of an RF driven discharge to excite the atoms into the metastable state. The idea is that in the plasma, electron-atom collisions have a finite, though small probability of exciting the atoms to the metastable level. This yields a metastable excitation efficiency on the order of 10^{-6} to 10^{-5}. As of date, this is the state of the art of metastable helium production.

As we mentioned in section 5.1, ^{6}He and ^{8}He are transported as ions at 20 keV. The atoms are then neutralized, and pumped into the atomic beam apparatus. On entry, the helium atoms are mixed with a carrier gas made up either of krypton (Kr) or xenon (Xe). We need the additional pressure provided by the carrier gas in order to be able to sustain the plasma. The metastable discharge source we used is similar to that used in [164, 165]. It is basically a quarter wave helical resonator, which operates at a fundamental frequency of $\sim$ 80 MHz. A schematic drawing of the discharge source is given in figure 5.4. Such resonators are particularly useful because they are able to sustain plasma discharges at relatively low residual pressures [103]. We cool the discharge by liquid nitrogen(LN_2), which is made to flow into a reservoir which is in contact with a ceramic tube that conducts the gas. This serves to reduce the effective temperature of the beam that is released into the Zeeman slower. Xe as a buffer gas yields a slightly ($\times$1.4) better metastable yield than Kr. For tuning, we used mostly Kr because of the higher cost of Xe. We used Xe during the experimental run.

5.2.2 Vacuum system

The atomic beam line that we used was $\sim$ 2 meters in length, and is shown in figure 5.3. A combination of two turbo pumps (pumping speed 250 L/s and 300 L/s) pumped out

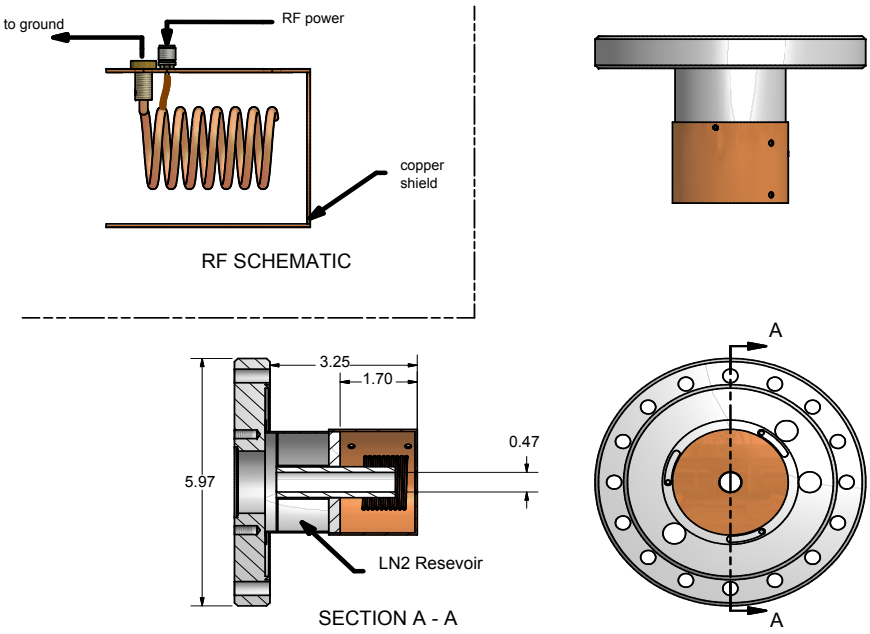

Figure 5.4: Schematic of RF discharge Source used for creating metastable helium atomic beam. (All dimensions are in inches)

the transverse cooling chamber. Thereafter, we had a conductance limiter, between the TC chamber and a four-way cross, which had a third turbo pump of 250 L/s. We used a Leybold 381c turbo pump to evacuate the MOT chamber. The equilibrium pressure of the MOT chamber was $\sim 5 \times 10^{-8}$ Torr. This resulted in a vacuum limited MOT lifetime of a few hundred milliseconds — longer than the half life of ^{8}He (118 ms).

5.2.3 Laser systems

We operated two independent laser systems for this experiment. For slowing and loading of atoms into a magneto-optical trap, we made use of the transition $2^3S_1 \rightarrow 2^3\mathrm{P}_2$ at 1083 nm. The 2^3S_1 $m_J = 1 \rightarrow 2^3\mathrm{P}_2$ $\mathrm{m_J} = 2$ transition is cycling, and therefore suitable for laser cooling with circularly polarized light. For spectroscopy, we made use of the $2^3P_1 \rightarrow 3^3\mathrm{P_J}$ at 389 nm. The detection efficiency of 389 nm light using PMTs is really high. Furthermore,

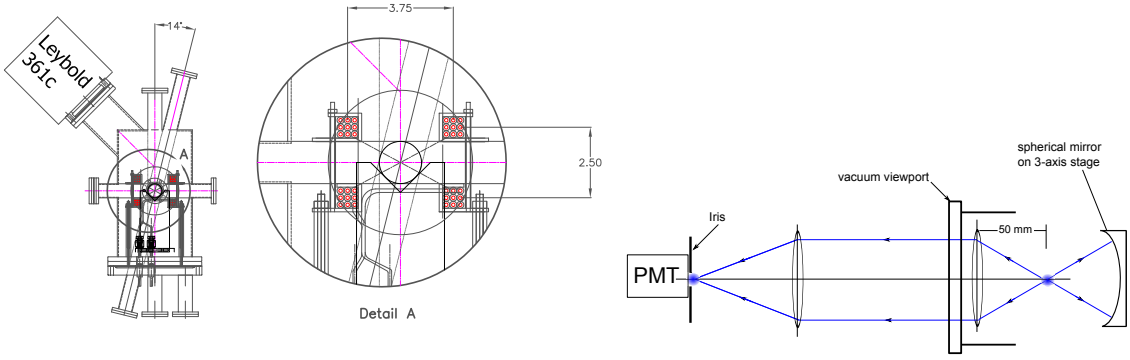

Figure 5.5: Schematic of the MOT magnetic coils. The coils are made of copper tubing—which is also the conductor for water cooling. The pair of ports at 14 degrees to the vertical ports were used for the spectroscopy beam, while on the horizontal plane, we had the MOT and slower beams as well as the MOT imaging optics, which are shown on the right. The interior of the vacuum system was painted black in order to minimize the background from scattered light.

1083 nm light can be easily separated from 389 nm light using interference filters. As such, the trapping light did not contribute the background.

1083 nm laser system

For laser cooling, it was important that the 1083 nm light was locked to the resonant frequency of the helium atoms. It was also important to have enough power to distribute for slowing the atomic beam, operating the MOT and transverse cooling. These three different tasks also required independent frequency and amplitude control.

We generated 1083nm light from a home made diode lasers which were amplified by fiber amplifiers from Keyopsys. The diodes were from Toptica, Model LD-1083-0075. The setup is shown in figure 5.7. We made use of two lasers, designated as DL1 and DL2. DL1 is locked to one of the modes of a hermetically sealed Fabry-Perot cavity with FSR = 300 MHz. At the same time, light from DL1 is used to perform saturation spectroscopy in a helium vapor cell. The length of the cavity is stabilized to the atomic resonance of either a ^{3}He or ^{4}He saturation spectroscopy resonance. Finally, DL2, after double passing AOM1, is also locked to the same cavity, albeit to a different mode. Consequently, by scanning the frequency of

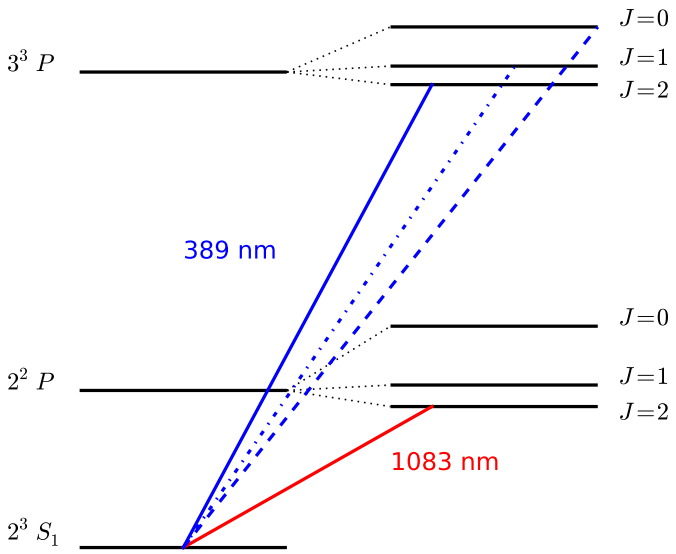

Figure 5.6: Level Scheme for Helium Showing the 1083 nm and 389 nm transition. The 1083 nm transition to J = 2 is used for cooling. We excite transitions to each of the three fine structure levels in the 3^3P manifold for spectroscopy.

AOM1, and by changing the mode to which DL2 is locked, we can change the frequency of the 1083nm light that is sent to the fiber amplifiers and eventually to the experiment. The frequency difference between the two lasers is precisely determined by measuring the beat frequency of the interference of the two lasers.

As shown in figure 5.7, we had independent control of frequencies of the light going to the MOT, slower and transverse cooling. In order to switch isotopes, we locked DL1 to a different line in the helium vapor cell, and also changed the offset frequency shift given by AOM1 in figure 5.7. Amplifier 1 supplied up to 4 Watts of light which was distributed to the transverse cooling and slower. Fiber amplifier 2 supplied 1 W, and its output was used to create the MOT.

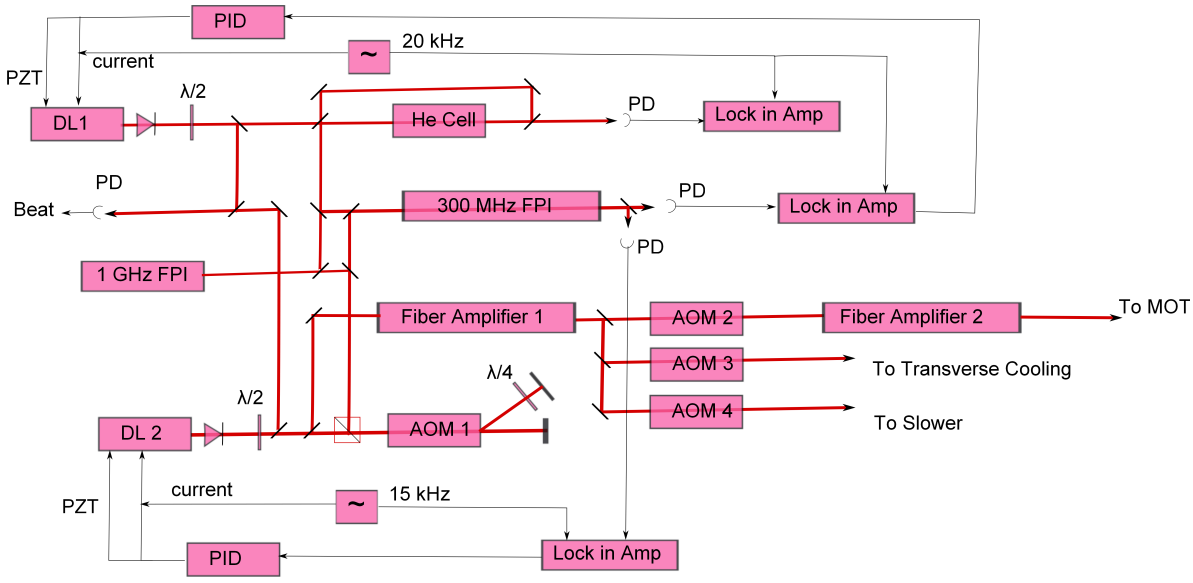

Figure 5.7: Setup of optics used for generating 1083 nm light.

389 nm laser system

For spectroscopy, we generated 389 nm light by frequency doubling 778nm light. The layout of the table is shown in figure 5.8. This layout is similar to the layout used in [164]. Once again, we use a transfer lock using a cavity to lock DL1 to a saturation spectroscopy feature of iodine. A second diode laser at 778 nm (DL2) is also locked to the same 200 MHz cavity after double passing an acousto-optical modulator, (AOM1 in gigure 5.8). Its frequency is then tuned by scanning AOM1. Light from DL2 is used to injection lock another diode laser, DL3. The output of DL3 is then amplified by sending it to a tapered amplifier and then frequency doubled using an LBO crystal in a doubling ring cavity. The 389 nm light output from the doubling ring was then double passed through an AOM2 which had a center frequency of 100 kHz. The emergent first order beam was therefore shifted up by 200 kHz. By scanning that AOM, we therefore scanned the frequency of the laser. Typically, we had

approximately 1 mW of 389 nm light available for spectroscopy. The exact frequency of the lasers was determined by measuring the beat note between DL1 and DL2.The exact value of the beat frequency depended on the transition (and isotope) we were measuring. Its value varied from 0 up to 20 GHz. The relative positions of the $2^3S_1 - 3^3P_2$ lines for ^{4}He. ^{6}He and ^{8}He are shown with respect to an iodine line with wave number 12854.92 cm^{-1} (i.e. 777.91 nm).

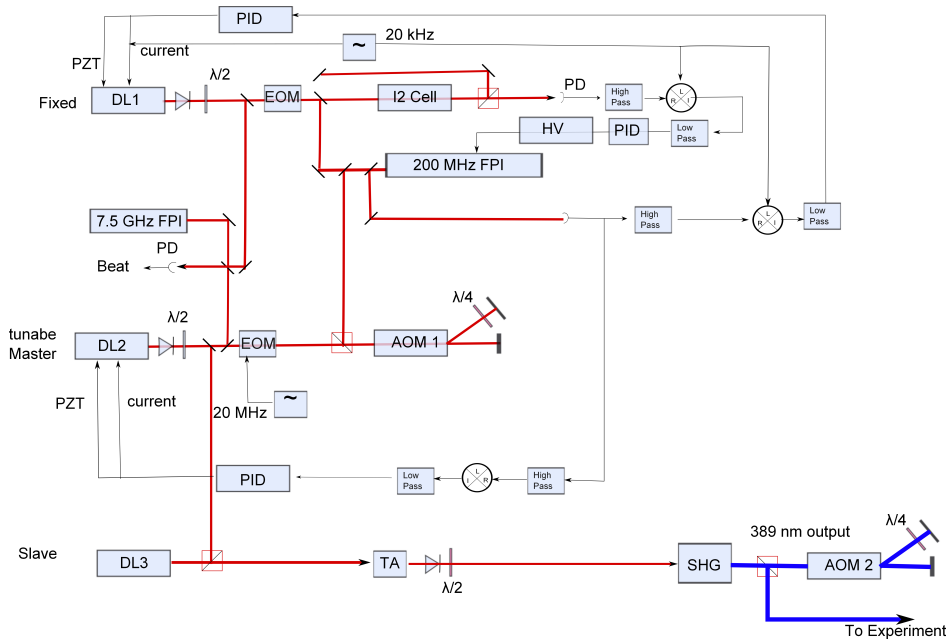

Figure 5.8: Setup of optics used for generating 389 nm light.

5.2.4 Transverse cooling

We employed a stage of transverse cooling of the metastable beam that emerged from the RF discharge source. The basic idea of transverse cooling is that by laser cooling a divergent atomic beam in the direction transverse to its motion, we are able to collimate it and increase its forward brightness. One improvement that we made on the system over that used in [164, 165] is that we made use of a longer transverse cooling section. The length of the TC

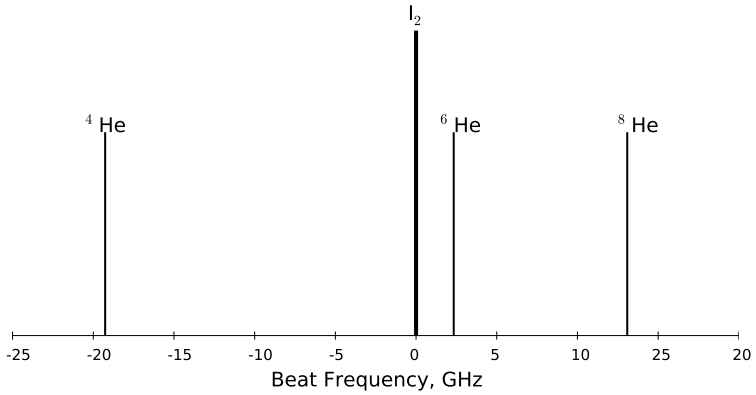

Figure 5.9: Lock point of spectroscopy with respect to an molecular iodine line. DL1 was locked to the Iodine line, while DL2 was scanned to either the ^{4}He, ^{6}He or ^{8}He resonance. We kept track of the absolute frequency by measuring the beat frequency between DL1 and DL2

mirrors was increased from 4" to 7". Furthermore, one of the mirrors, in each dimension used to set up the retro-reflecting pattern of the transverse cooling beam was placed inside the vacuum system with adjustability. In the old design, the mirrors were fixed.

All in all, we obtained an increase in the loading rate of the MOT from the transverse cooling stage of a factor of 100. This was a factor of 4 improvement over the older transverse cooling scheme. All these improvements were performed in order to improve the overall trapping efficiency of the system.

5.2.5 Zeeman slower

We made use of a Zeeman slower in order to successfully slow down an atomic beam from a thermal energy of 77 K (from the LN2) to the capture velocity of the trap. At 77 K, the most probable velocity of ^{8}He atoms is 400 m/s. The basic idea of a Zeeman slower is that because laser cooling relies on the resonant scattering of photons, this force exerted by the

light is only substantial once the atom is near resonance. Now, as an atom is slowed down, its Doppler shift becomes significant, and could even exceed the natural line width of the transition. In order to compensate for this, one must restore the resonance condition. This can be done by either changing the frequency of the laser (i.e. chirping the laser), or by changing the transition frequency using the Zeeman effect.

In order to maintain resonance for a beam being slowed down from 77K, we engineered a spatially varying magnetic field of the form:

$$B(z) = B_{\max}\sqrt{1 - z\frac{a_{\max}}{v_0^2}} \tag{5.1}$$

where

$$B_{\max} = \frac{h}{\mu_B \lambda} v_0 \tag{5.2}$$

and v_0 is the capture velocity of the slower. v_0 is of course a function of the maximum acceleration imparted on the atom by the scattered photon $a_{\max}$, the length of the slower L and the final velocity v_f.

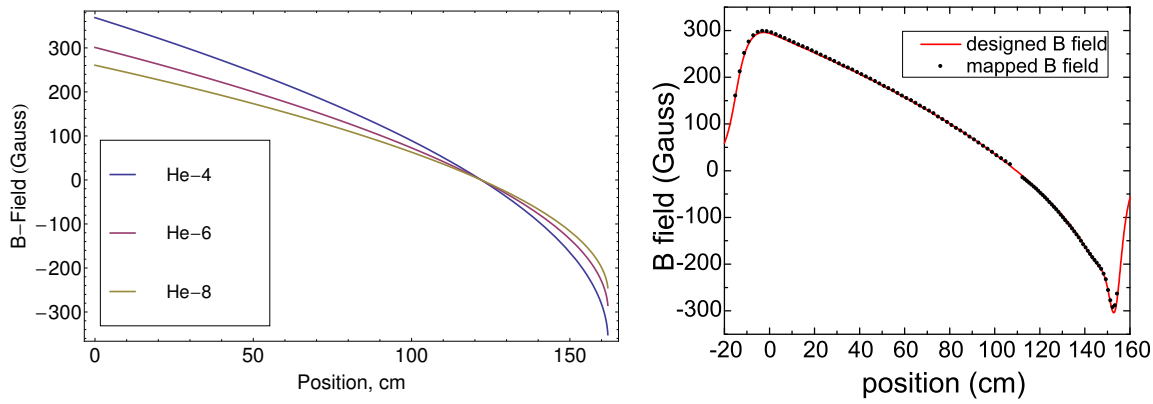

Figure 5.10: The left panel shows the calculated magnetic field profile for the Zeeman slower optimized to trap the three different isotopes. On the right panel, we show the calculated ^{6}He profile for the slower and MOT, along with the measured magnetic field. Figure reproduced from [164]. For the measurements reported here, the slower was operated in the setting shown for ^{8}He.

The Zeeman slower used for the experiment is identical to the one used in [164, 165]. It consists of two tapered solenoids such that there is a zero field crossing at approximately 100cm (shown in figure 5.10). The field was mapped after the coils were wound and found to be consistent to the design. Given that there were 3 independent coils, we were able to tune the slower to optimize the loading rate of different isotopes by changing the relevant set points of the currents which we supplied to the coils.

We also made use of a match coil, and a trim coil in order to create a smooth transition from the large fields in the slower to the zero field required for the MOT.

For the spectroscopy measurements, we operated the zeeman slower at a setting optimal for ^{8}He. In switching isotopes, we did NOT switch the slower. This is in order to keep the magnetic fields at the trap the same for all isotopes—avoiding possible systematic effects.

5.2.6 Magneto-optical trap of metastable helium

The principle of operation of a magneto-optical trap is described in detail in [108, 65]. Here, I will simply summarize some of the specifics of our magneto-optical trap for metastable helium. As mentioned above, the transition at 1083 nm is used for laser cooling of helium.

Since the ^{6}He and ^{8}He atoms are of such low abundance, the MOT is set up in order to optimize the loading rate. We refer to this configuration as the 'Loading Mode'. Once an atom is detected in the MOT, the state of the system is changed to the 'Spectroscopy Mode'. Here, we operate the MOT in such a way whereby the spatial extent of the MOT is highly reduced—ensuring that the fluorescence of the atom in the trap is efficiently collected. We achieve this reduction by changing the detuning and intensity of the MOT light. The exact values of detuning and intensity are given in table 5.2.

While awaiting the arrival of, say a ^{8}He atom, we had a resonant 389 nm beam illuminating the MOT center. The trigger was implemented in software. We kept a running average

Table 5.1: Calculated Parameters relevant for Laser cooling of helium for the 1083 nm and 389 nm transitions

.

Parameters	$2^3S_1 - 2^3P_J$	$2^3S_1 - 3^3P_J$		Units / Description
λ	1083	389	(nm)	Transition Wavelength
$k = 1/\lambda$	9223	25706	(cm^{-1})	Wavenumber
τ	98	106	(ns)	Atomic State Lifetime
$\sigma_{ge} = 3\lambda^2/2\pi$	560	72	(10^{-15} m^2)	Absorption cross section
$\Gamma = 1/2\pi\tau$	1.62	9	(MHz)	Natural linewidth
$I_s = \pi hc/3\lambda^3\tau$	0.16	3.33	(mW/cm^2)	Saturation Intensity
$T_D = h\Gamma/2k_B$	38	36	(μK)	Temp limit of Doppler cooling
$v_r = \hbar k/M$	12	34	^{3}He	Recoil velocity (cm/s)
	9	25	^{4}He	
	6	17	^{6}He	
	4	12	^{8}He	
$V_D = \sqrt{k_B T_D/M}$	10.8	9.9	^{3}He	Doppler Limit Velocity (cm/s)
	8.1	7.4	^{4}He	
	5.3	4.9	^{6}He	
	4.0	3.7	^{8}He	
$\omega_r/2\pi = \hbar k^2/4\pi M$	56	439	^{3}He	Recoil frequency (kHz)
	42	329	^{4}He	
	28	219	^{6}He	
	21	164	^{8}He	
$a_{max} = \hbar k/2M\tau$	62	174	^{3}He	Maximum Acceleration (10^4 m/s^2)
	46	130	^{4}He	
	31	87	^{6}He	
	23	65	^{8}He	
$T_r = \hbar^2 k^2/Mk_B$	5.6	43	^{3}He	Recoil Temperature (μK)
	4.2	32	^{4}He	
	2.8	21	^{6}He	
	2.1	16	^{8}He	

Table 5.2: Conditions of 'Loading' and 'Spectroscopy' modes of operation. Note that the 389 nm beam is + 5MHz detuned during the loading phase. This ensures that the transition is resonant when one accounts for the AC Stark shift due to the trapping light

	Loading Mode	Spectroscopy Mode
MOT Detuning ($\Delta/2\pi$)	-20 MHz	-3 MHz
MOT Intensity	70 I_s (CW)	5 I_s (chopped, 100 kHz 80% ON duty cycle)
Slower Detuning ($\Delta/2\pi$)	(-512,-418,-362) MHz for ^{4}He, ^{6}He and ^{8}He	Off
Slower Intensity	100 Is	
389 nm Detuning ($\Delta/2\pi$)	+5 MHz	Scanning
389 nm Intensity	~ 1 I_s (CW)	~ 1 I_s (chopped, 100 kHz 20% ON duty cycle)

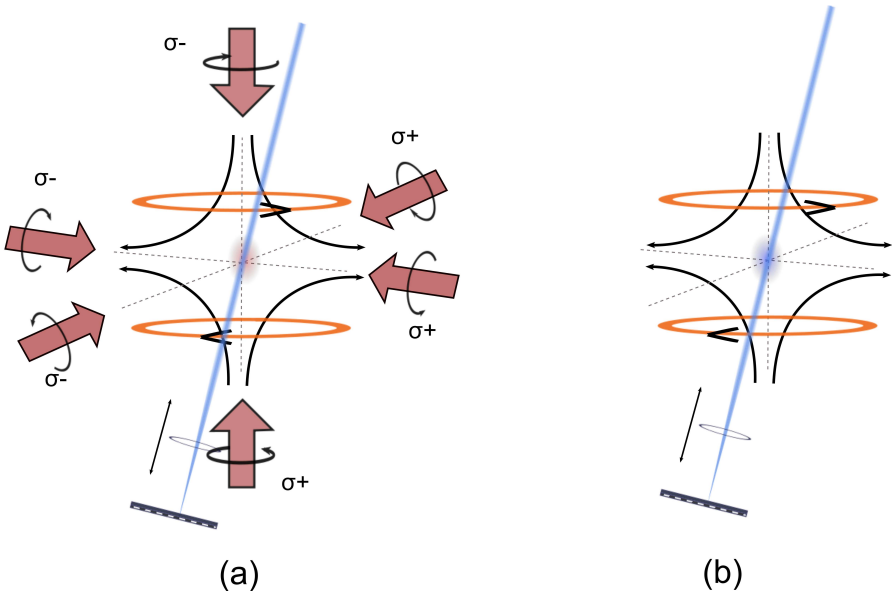

Figure 5.11: Schematic for difference between (a.) Loading mode, where the 1083nm light for the MOT is on and (b.) Spectroscopy mode, where 1083 nm light is off, and 389 nm light is on. Note that in both cases, the magnetic field is kept on. We make use of a cat's eye retro reflector arrangement, with a lens on a translation stage. We adjust the position of the lens to ensure balanced intensities of the 389 nm beam.

of the singles rate from our PMT sensitive to 389 nm light. Upon the arrival of an atom, we noted an increase in the count rate. However, there were also false events due to the PMT detecting neutrons which were generated by the operating cyclotron. Those signals from the neutrons were usually stronger than the atom signals, and also very short lived ($\sim$ 1 ms). We therefore required that a real event consists of counts greater than background, but lower than the neutron level, and that the elevated rate persisted for 50ms. When those conditions were satisfied, we changed modes to spectroscopy mode. We detected the presence of a single atom signal with a signal to noise ratio of 10 within 50 ms of integration.

5.3 Spectroscopy of trapped helium atoms

Recall from the introduction of this chapter that our goal was to perform spectroscopy on the 2^3S_1 to 3^3P_J transitions in ^{4}He, ^{6}He and ^{8}He and to determine the isotope shifts on those transitions.

Once the system was in spectroscopy mode, the 389 nm laser was scanned continuously around the resonance over a span of ± 9 MHz around the resonance of interest. The total scan took $\sim 6\mu s$. A schematic of the timing used during spectroscopy mode is shown in figure 5.12.

Anticipating the need to understand certain systematic errors, we measured the spectra (for ^{4}He and ^{6}He) under varying probe intensity levels. This will be discussed in detail in section 5.7. We describe below in some more detail the steps taken for data collection.

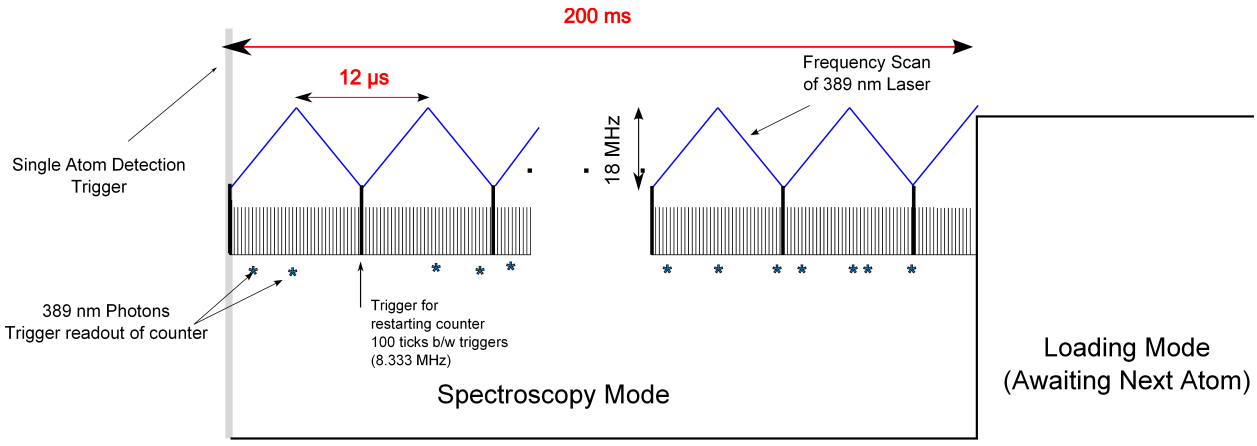

Figure 5.12: Timing Scheme for chopping and trapping. On Detecting a single atom in the trap, the system is switched to spectroscopy mode where an 8.333 MHz counter starts. The counter is phase locked with 83.33 kHz frequency that generates ramp for frequency of 389 nm light. Subsequently detected photons trigger the readout of the counter.

5.4 Data collection

Each atom arrival trigger event initiated

(i) The switch from Loading to Spectroscopy mode

(ii) The start of an 83.333 kHz triangular ramp, used to control the voltage of the 389nm AOM which effectively changes the frequency of the 389 nm laser.

(iii) The start of an 8.333 MHz counter, which serves as a clock used to encode photon arrival times.

In spectroscopy mode, the frequency of the 389 nm light is being scanned. Subsequently detected 389 nm photons trigger a readout of the clock pulses.The data was stored as a series of time stamps of photon arrival for each trigger event.

5.4.1 Measurement procedure

During each run, we cycled between the three helium isotopes in a procedure outlined in table 5.3. On average, during each run, we spent about 15 minutes on ^{4}He and a similar interval of time on ^{6}He. We operated the trap under conditions where the loading rate was similar between ^{4}He and ^{6}He. We achieved this loading rate for ^{4}He of a few atoms per second by operating the system with no transverse cooling as well as with a very small diameter slowing beam. Furthermore, for these two isotopes, we studied the dependence of the fluorescence peak center on the intensity of the probe light. This is because a large class of systematic errors such as mechanical effects of the light, heating/cooling effects, power broadening etc. scale with the intensity of the light being used to illuminate the atoms.

For ^{8}He, we accumulated data until we had recorded the capture of ~ 60 atoms. This took between 2 - 3 hours. Because of the comparably low loading rate, we only performed

spectroscopy at the highest intensity setting of the probe light. In quantifying possible systematic errors due to the intensity of the light, we make use of the results from ^{4}He and ^{6}He. This will be treated more in section 5.6.

The switching procedure between isotopes involved re-locking both the trapping and spectroscopy lasers to the set point of the desired isotope. This typically took around 10 minutes.

Table 5.3: Measurement procedure during a run

Isotope	389 nm Power Level	Time
^{4}He	70 μW 100 μW 900 μW	15 Minutes
SWITCH ISOTOPE		10 Minutes
^{6}He	70 μW 100 μW 900 μW	15 Minutes
SWITCH ISOTOPE		10 Minutes
^{8}He	900 μW	2 - 3 Hours

5.4.2 Fine structure interval measurements

Recall that for the even isotopes of Helium, the 3^3P manifold is split up into three fine structure levels namely 3^3P_0, 3^3P_1 and 3^3P_2. Over the course of the experiment, we were able to excite and consequently measure the frequency of the following transitions:

(a) $2^3S_1 - 3^3P_2$ for ^{4}He, ^{6}He and ^{8}He

(b) $2^3S_1 - 3^3P_1$ for ^{4}He, ^{6}He and ^{8}He

(c) $2^3S_1 - 3^3P_0$ for ^{4}He and ^{6}He. We did not record this spectrum for ^{8}He because it was very weak and would have required long integration times in order to get an adequate signal to noise ratio.

5.5 Data analysis

5.5.1 Applying atom cuts

Whenever the trigger condition was satisfied, we wrote all the photon arrival times to file. Of course, not all events were true atom events. Considering that the 1/e lifetime of the trap was a couple hundred milliseconds, and that the half life of ^{8}He is 119ms, we applied cuts on the data based on the total number of detected photons during a 12 μs period—the period for a complete sweep over the scan range of the 389 nm laser. In figure 5.5.1, we show a sample of the raw data obtained, as well as the result of setting a cut of greater than 30 detected photons. We applied this same cut on all the data that we analyzed.

In figure 5.5.1, the spectrum obtained arises from the spectroscopy laser traversing over the resonant frequency twice. Once with the frequency increasing and once with the frequency decreasing.

5.5.2 Converting time bins to frequency

The raw data is written to file as series of 389nm photon arrival times. For each data point, we recall the frequency of the scanning AOM which scans around the resonance by mapping the photon arrival time stamp with the AOM frequency. The scanning AOM is controlled by a function generator which is locked to the same frequency reference that generates the clock for the photon arrival times. We verify the long term stability of the AOM by performing a

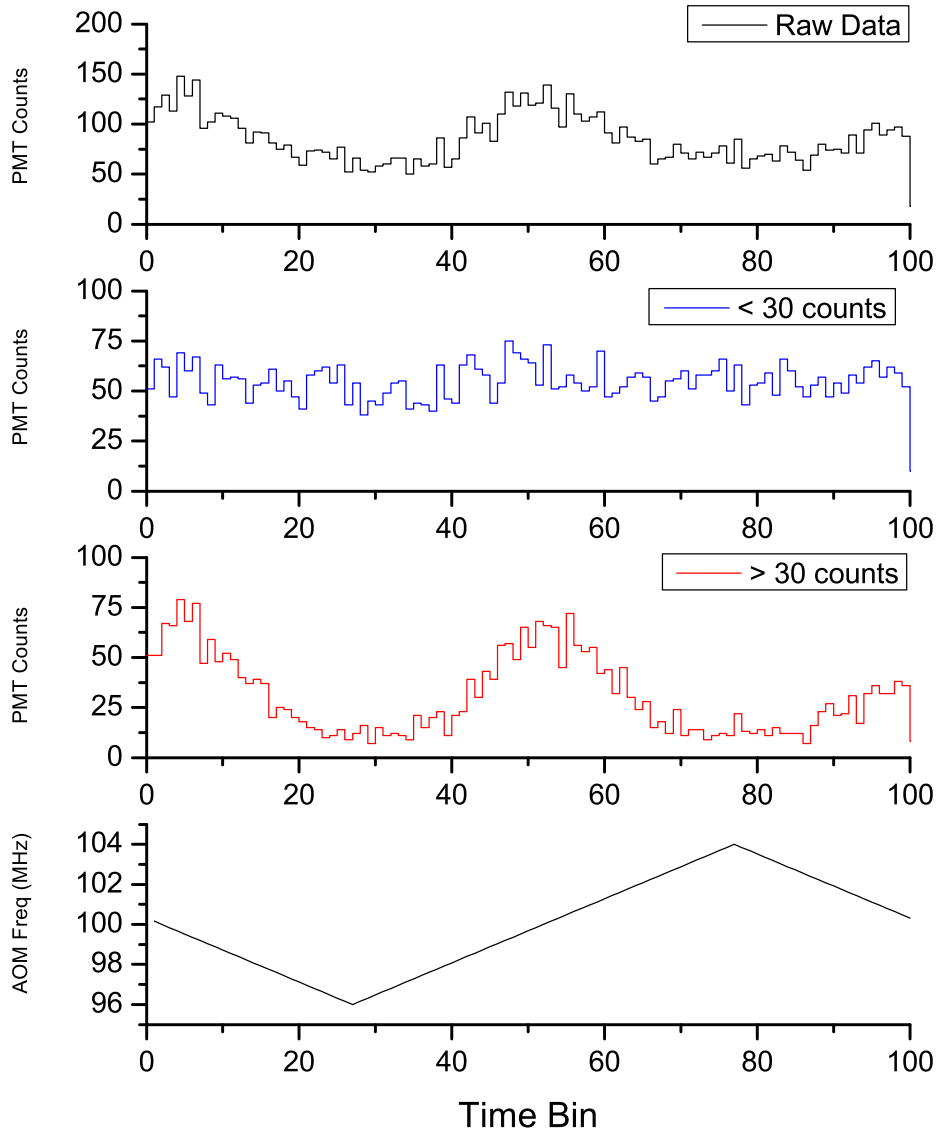

Figure 5.13: The top panel shows the raw histogram obtained from all single photon events. We further applied cuts on all events that had less than 30 photons detected during the 12 μs period associated with a scan.

voltage to frequency calibration every day.

Over the course of one run, we observed a VCO drift of $<$ 400 Hz, due to fluctuations in the control voltage.

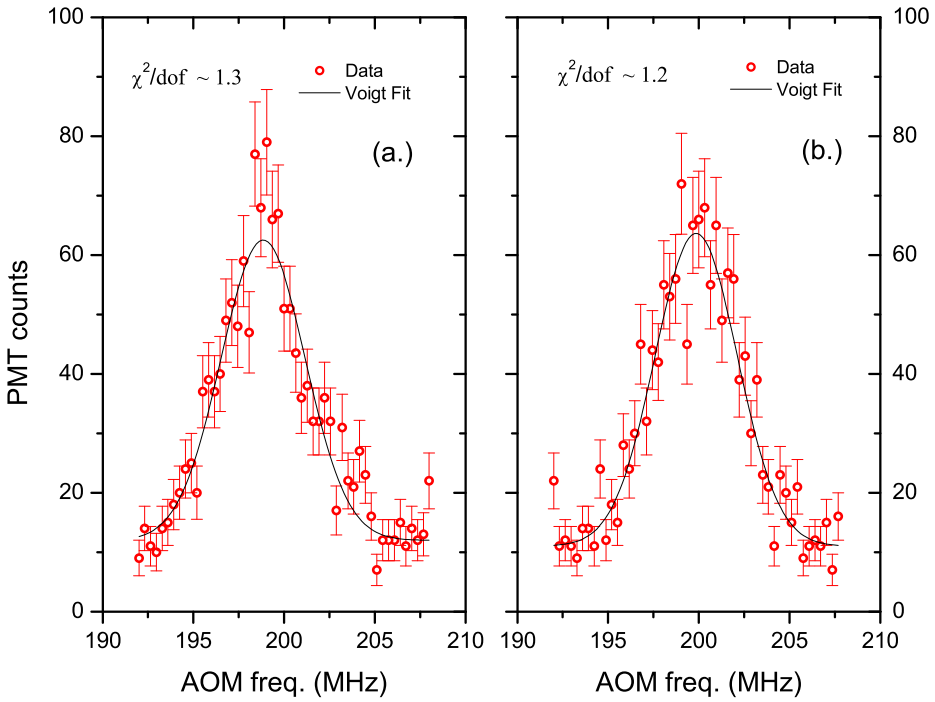

Figure 5.14: Frequency scan across the ^{8}He resonance showing two peaks, one each for the frequency increasing and decreasing with time. Error bars shown are the statistical error bars due to photon shot noise.

5.5.3 Power dependence of the resonant frequencies

Once we have converted the time bins to frequency, we next perform a least squares fit to each line to a voigt profile. We treat the line with ascending frequency independently with the line with descending frequency. The number of points at each frequency setting are weighted statistically. We obtain fits to each line with a typical $\chi^2/\text{dof} \sim 1.2$.

A spectrum is taken for 3 different settings of the intensity of the probing beam. Data for ^{4}He and ^{6}He is shown in figure 5.15. We observe that the extracted resonant frequencies do indeed depend on the intensity of the probing light. This might be due to the mechanical effects of the probing laser. By extrapolating to the condition of zero probing intensity, we expect shifts associated with pushing or heating by the 389 nm light to tend to zero. Our analysis procedure with respect to the power dependence is as follows:

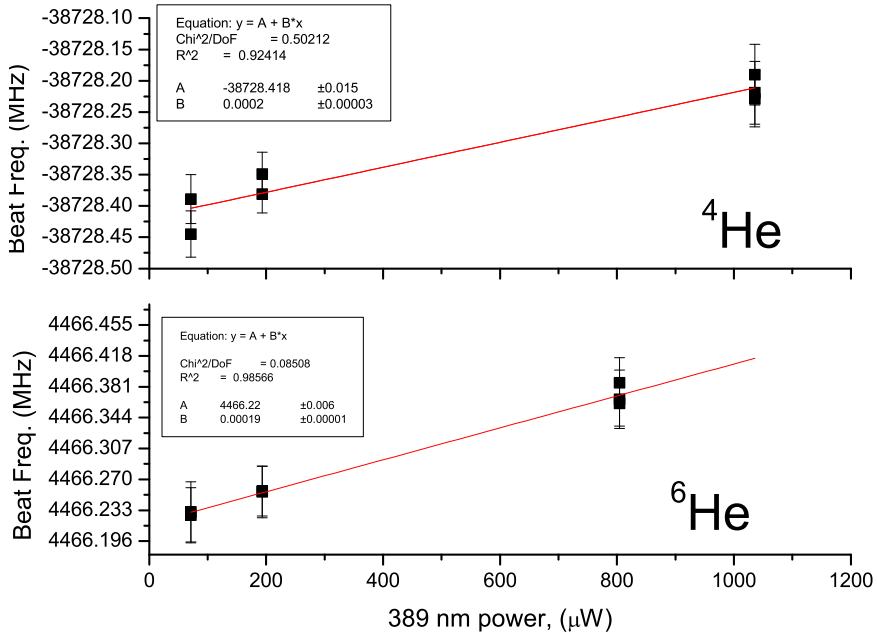

Figure 5.15: The resonance frequency as a function of the probing power of two representative transitions in ^{4}He and ^{6}He. This data was taken during each ^{4}He and ^{6}He run. As can be seen, their relative slopes are comparable.

1. For ^{4}He and ^{6}He lines, we measure the line centers under 3 different conditions. The final value of that transition is the zero intensity intercept.

2. For ^{8}He, we measure the transition frequency with a probe beam of 700μm. An effectively zero intensity value of the peak center is obtained for the ^{8}He measurement by correcting the value using the power dependent slope obtained from ^{4}He and ^{6}He.

5.6 Statistical error analysis

5.6.1 Photon counting

In figure 5.5.1, we show a pair of spectra obtained for ^{8}He. As a first step in our data and error analysis, we perform a least squares fit to a voigt profile (with a fixed Lorentzian width) in order to determine the line center. Each point is simply weighted by photon counting statistics (i.e. photon shot noise). The χ^2 in each of such fits was typically $\chi^2 \sim 1.3$ per degree of freedom. This suggests that there might be additional sources of of random fluctuation in the data during the course of accumulating data. Some parameters in our setup that we expect to drift over the period of a measurement are considered next.

5.6.2 Probing laser alignment

One source of random scatter in our measurements of the resonance frequencies of the transitions we were studying, we believe, comes from the relative balance between the downward and the retro-reflected 389 nm spectroscopy beam. This beam is incident on the atoms at an angle, 14 degrees to the vertical. This is shown in figure 5.5. Now, if the beams are imbalanced, we would expect that the trapped atoms would be pushed in the direction of the vertical beam; either upwards or downwards, depending on which direction had the more intense beam.

Since the second return beam had to go through an optical view port two times more than the downward going beam, its power is expected to be lower. However, we ensure that the intensity of the two beams is the same by focusing the return beam slightly. We do so by adjusting the position of the lens in the cat's-eye reflector—thereby changing the focusing of the reflected beam.

We determined that we were in a balanced configuration by the following procedure. For

each setting of the cat's-eye reflector, we measured and plotted the line center frequency vs probing light intensity. The setting which had the minimal slope corresponded to the balanced upward and downward going beams. In figure 5.16, we show a series of the slopes of the frequency vs power determined for ^{4}He immediately followed by a similar measurement for ^{6}He which were taken throughout the duration of the experiment. Each measurement is separated from the adjacent one by $\sim$ 4 to 5 hours. Over the course of the run, we noticed that the slope of the two isotopes were roughly correlated with each other. It is important to note that there is no statistically significant difference between the average slope for the power dependence of ^{4}He and ^{6}He.

The 389 nm light is free space coupled around three-meter distance from the laser table to the atomic beam line from which it is coupled down to the atoms in the vacuum chamber. For spectroscopy on ^{6}He, we obtained data in a rather short period of time. As a result, we extrapolated the measured frequency to zero intensity—allotting little uncertainty to fluctuations in the pointing of the probe beam. For the spectroscopy of ^{8}He however, we obtained data over a substantially longer period of time. We allotted uncertainty in the isotope shift between ^{8}He and ^{4}He of 12 kHz, due to the fluctuation of the pointing of the 389 nm probe beam.

5.6.3 Reference laser frequency drift

The final source of statistical error that we consider in our error budget is statistical fluctuations of the reference frequency of the spectroscopy light. Recall that the long term stability of the 389 nm light is obtained by locking the fundamental frequency at 778 nm to a saturation spectroscopy peak in iodine. One source of random fluctuations in the 389 nm frequency could therefore come from fluctuations in the lock to the iodine reference.

An additional source of frequency drift that we must have under control is frequency drift

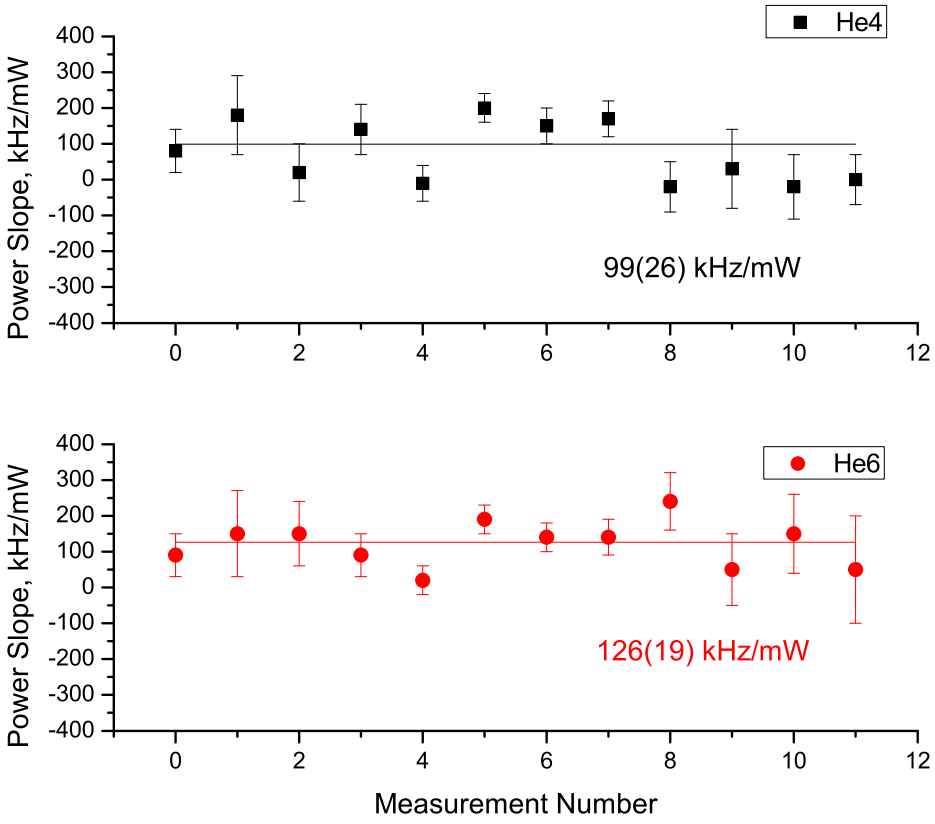

Figure 5.16: The variation of the slope of the resonance frequency vs. probe beam power over the course of the run. There appear to be low frequency drifts in the magnitude of the slope. We believe this is due to the fluctuation in the probe beam pointing

due to the fluctuation of the control voltage for the AOM used to perform the fast scan of the 389 nm light across the atomic resonance. Once again, because we are able to acquire data for ^{6}He over a time short compared with the time scale for frequency drift, we allot an uncertainty of 2 kHz for ^{6}He and of 24 kHz for the ^{8}He field shift.

Table 5.4: Experimental isotope shifts $\delta\nu_{A,4}$ (including recoil correction) for the different transitions in ^{6}He and ^{8}He. All values are in MHz. The errors given in parentheses for $\delta\nu_{A,4}$ and $\delta\nu_{A,4}^{\mathrm{FS}}$ include only statistical uncertainties.

	Transition	$\delta\nu_{A,4}$
^{6}He	$2\,^3S_1 \rightarrow 3\,^3P_0$	43196.740(37)
	$2\,^3S_1 \rightarrow 3\,^3P_1$	43194.483(12)
	$2\,^3S_1 \rightarrow 3\,^3P_2$	43194.751(10)
^{8}He	$2\,^3S_1 \rightarrow 3\,^3P_1$	64701.129(73)
	$2\,^3S_1 \rightarrow 3\,^3P_2$	64701.466(52)

5.7 Systematic error analysis

5.7.1 Probing power shift

The ^{8}He "zero intensity" line center frequencies are determined by extrapolating from the values of the measured power dependence of ^{4}He and ^{6}He. As no such correction has to be applied to the ^{6}He-^{4}He IS measurement, there could be an associated systematic error which would affect the ^{8}He - ^{4}He IS measurement alone. Given that the slope of the power dependence is $\sim$ 100 kHz/mW, and the measurements for ^{8}He are performed with probe powers of $\sim$ 700 μW, we make a correction to the ^{8}He line center frequencies of 70 kHz and allot an uncertainty 15 kHz due to that correction.

5.7.2 Zeeman shift

A systematic uncertainty is caused by Zeeman shifts that might have varied among isotopes if the atoms were not located exactly at the zero B-field position of the MOT. Limits on this effect are set conservatively at $<$ 30 kHz for the ^{6}He - ^{4}He isotope shift, and $<$ 45 kHz for ^{8}He - ^{4}He.

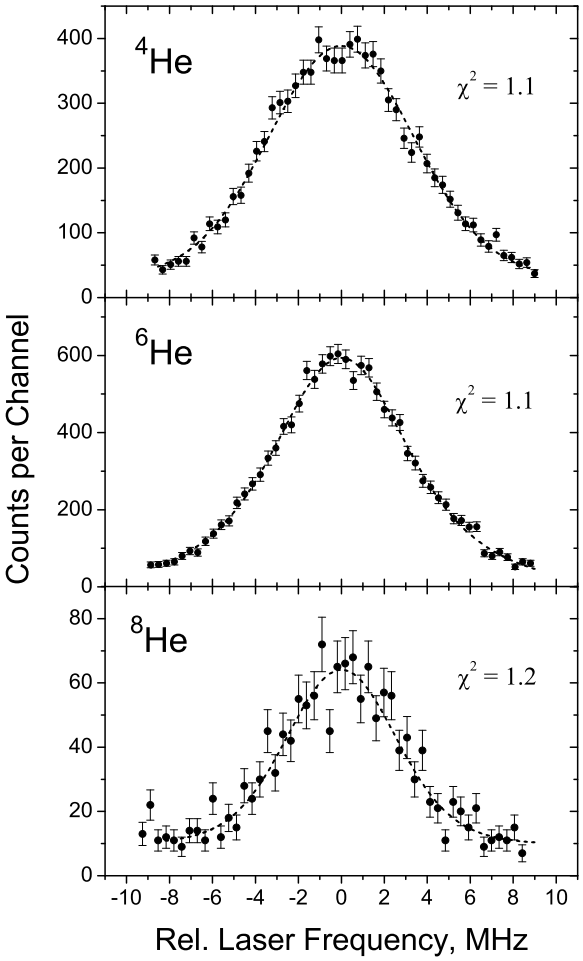

Figure 5.17: Sample spectra for ^{4}He, ^{6}He and ^{8}He taken on the $2\,^3S_1 \rightarrow 3\,^3P_2$ transition at a probing laser intensity of $\sim 3 \times I_{\mathrm{sat}}$. Error bars are statistical uncertainties, the dashed lines represent least squares fits (with the listed reduced χ^2) using Voigt profiles. The apparent peak broadening towards lower masses is due to the $1/\sqrt{m}$ scaling of the residual Doppler width.

5.7.3 Nuclear mass

Uncertainties due to the determination of the nuclear mass of ^{4}He, ^{6}He and ^{8}He affected our experiment via the mass shift calculations reported in table 4.2. The mass shift uncertainties amount to 15 kHz and 74 kHz respectively. We allot those values as systematic uncertainties due to nuclear mass determination in what we quote for the field shift.

Since the publication of our result, the mass of ^{8}He [142] has been measured with almost a factor of 10 improved precision. The values charge radius values reported in this thesis take the newly measured masses into consideration. As a result, the uncertainty in the mass shift due to the nuclear mass is greatly reduced.

5.8 Corrections to the isotope shift

5.8.1 Photon recoil

This is a correction that we make to the measured field shift of each isotope. It arises from the fact that when a photon is absorbed or emitted, energy-momentum conservation requires that the atom receive a recoil equal in magnitude to that of the emitted or absorbed photon, given by $f_{\text{rec}} = hk^2/2M$. This is accurately calculated. It is very important for helium atoms because they are very light. It is especially important for an isotope shift measurement because the recoil correction is mass dependent. For example, ^{8}He - ^{4}He, $f_{\text{rec}} = 165$ kHz and ^{6}He - ^{4}He, $f_{\text{rec}} = 110$ kHz

5.8.2 Nuclear polarization

The nuclear polarization correction correction and uncertainty associated with it refers to the extent to which the nucleus is polarized by the electric field generated by the atomic electrons [120]. This nuclear polarization can lead to a perturbation of the energy level of the energy levels being measured. In ^{6}He for example, the nuclear polarizability correction is $\sim 0.35\%$ of the finite nuclear size effect [120].

Nuclear polarizabilities can be extracted from the nuclear E1 transition matrix element. The are characterized by the so called ‘ B(E1) values’. An example of the nuclear polarizability determination using B(E1) values is provided in [91]. Pachucki *et al* in [120] compute

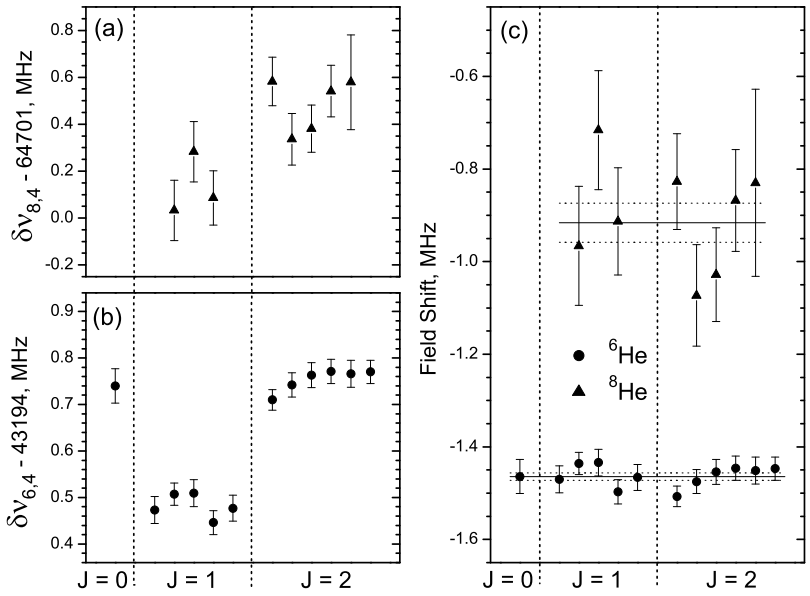

Figure 5.18: Experimental isotope shifts relative to ^{4}He from the individual measurements for ^{8}He (a) and ^{6}He (b). As expected, the isotope shift depends on the J of the upper $3\,^3P_J$ state. However, the extracted field shift values plotted in (c) show no systematic J dependence for either isotope. The horizontal lines in (c) mark the weighted averages and statistical error bands of the field shift.

corrections to helium atomic levels. We apply those corrections, namely 0.014(3) MHz and -0.002(1) MHz for the field shifts of ^{6}He and ^{8}He respectively. A nice discussion of nuclear polarizabilities and their impact on finite nuclear size determination from spectroscopy is given in [134].

5.9 Results

In table 5.6, we give the error budget, summarizing our estimate of the statistical and systematic uncertainties.

$$\begin{aligned} \delta\nu_{\mathrm{FS}} \text{ for } ^6\mathrm{He} &= -1.432 \pm 0.031 \text{ MHz} \\ \delta\nu_{\mathrm{FS}} \text{ for } ^8\mathrm{He} &= -1.006 \pm 0.067 \text{ MHz} \end{aligned} \tag{5.3}$$

Table 5.5: Weighted averages of the experimental isotope shifts $\delta\nu_{A,4}$ (including recoil correction) for the different transitions in ^{6}He and ^{8}He. The field shift $\delta\nu^{\mathrm{FS}}_{A,4} = K_{\mathrm{FS}}\,\delta\langle r^2\rangle_{A,4}$ was calculated for each transition using the listed *theoretical* mass shift values $\delta\nu^{\mathrm{MS}}_{A,4}$. All values are in MHz. The errors given in parentheses for $\delta\nu_{A,4}$ and $\delta\nu^{\mathrm{FS}}_{A,4}$ include only statistical uncertainties.

	Transition	$\delta\nu_{A,4}$	$\delta\nu^{\mathrm{MS}}_{A,4}$	$\delta\nu^{\mathrm{FS}}_{A,4}$
^{6}He	$2\,^3S_1 \rightarrow 3\,^3P_0$	43194.740(37)	43196.157	-1.464(37)
	$2\,^3S_1 \rightarrow 3\,^3P_1$	43194.483(12)	43195.897	-1.460(12)
	$2\,^3S_1 \rightarrow 3\,^3P_2$	43194.751(10)	43196.171	-1.466(10)
^{8}He	$2\,^3S_1 \rightarrow 3\,^3P_1$	64701.466(52)	64702.098	-1.053(52)
	$2\,^3S_1 \rightarrow 3\,^3P_2$	64701.129(73)	64702.489	-0.979(73)

Table 5.6: Statistical and systematic uncertainties and corrections on the combined results for the field shifts of ^{6}He and ^{8}He relative to ^{4}He. All values are in MHz.

	^{6}He		^{8}He	
	value	error	value	error
Statistical				
Photon counting		0.008		0.032
Probing laser alignment		0.002		0.012
Reference laser drift		0.002		0.024
Systematic				
Probing power shift				0.015
Zeeman shift		0.030		0.045
Nuclear mass		0.001		0.001
Corrections				
Recoil effect	0.110	0.000	0.165	0.000
Nuclear polarization	-0.014	0.003	-0.002	0.001
$\delta\nu^{\mathrm{FS}}_{A,4}$ combined	-1.432	0.031	-1.006	0.067

With the field shifts determined for an isotope of mass number A, we then make use of the expression

$$\delta\nu_{FS} = -1.008 \text{ MHz/fm}^2 \times \left(\left\langle \mathrm{r}^2 \right\rangle_{\mathrm{A}} - \left\langle \mathrm{r}^2 \right\rangle_{4}\right) \tag{5.4}$$

and the value $\langle r^2 \rangle_{ch}^{1/2} = 1.681(4)$ fm, for the ^{4}He helium charge radius [149] to obtain

$$\begin{aligned} \delta \left\langle \mathrm{r}^2 \right\rangle_{6,4} &= 1.420 \pm 0.031 \text{ fm}^2 \\ \left\langle \mathrm{r}^2 \right\rangle^{1/2} \text{ for } ^6\mathrm{He} &= 2.061 \pm 0.008 \text{ fm} \end{aligned} \tag{5.5}$$

and

$$\begin{aligned} \delta \left\langle \mathrm{r}^2 \right\rangle_{8,4} &= 0.998 \pm 0.067 \text{ fm}^2 \\ \left\langle \mathrm{r}^2 \right\rangle^{1/2} \text{ for } ^8\mathrm{He} &= 1.955 \pm 0.017 \text{ fm} \end{aligned} \tag{5.6}$$

5.10 Implications of Measurement

With the results reported in section 5.9, we now have a complete set of experimentally determined charge radii of nuclei on the helium isotopic chain using the atomic spectroscopy method. These are given in table 5.7 below.

Property	^{3}He	^{4}He	^{6}He	^{8}He	Units
$\delta \langle r^2 \rangle_{A,4}$	1.059(3)	–	1.420(31)	0.998(67)	fm^2
$\langle r^2 \rangle_{ch}^{1/2}$	1.967(7)	1.681(4)	2.061(8)	1.955(17)	fm

Table 5.7: RMS radii of the helium isotopes determined using the isotope shift method. The value for ^{6}He and ^{8}He are the results of this work, while the value for ^{8}He is from [147]

As we mentioned in chapter 2, one of the primary motivations of this work was to test the *ab initio* nuclear structure calculations on the neutron-rich helium isotopes. Caurier and

Navratil [35] and Pieper and Wiringa [126] used two sets of different *ab initio* potentials and many-body techniques to describe the helium isotopes. Recall that the different nuclear potentials as well as the many-body approaches were described in section 2.2. With the charge radius determination along the isotopic chain complete, we can consider the trends as one moves from ^{3}He to ^{4}He to ^{6}He to ^{8}He. We therefore hope to address the following two questions:

1. How well do the different *ab initio* nuclear structure approaches describe the experimentally measured charge radii?

2. How do we understand the trend in nuclear size? In particular, the RMS radius of ^{3}He is greater than the RMS radius of ^{4}He and ^{8}He, whereas ^{6}He is larger than the other three?

5.11 Comparison with nuclear theory

In figure 5.19, we plot the results of the experimentally determined RMS radii of ^{6}He and ^{8}He and compare them with the predictions from [35]. There, the authors made use of the No Core Shell Model (NCSM) approach with both the CDBonn and INOY potentials. The RMS radii are plotted against the corresponding two-neutron separation energies because the nuclear size and neutron separation energies are highly correlated. This correlation is especially pronounced in the case of nuclei with loosely bound 'halo' nuclei such as ^{6}He and ^{8}He. This is well reviewed in the article [4].

For ^{6}He, the CDBonn potential does a better job of reproducing the experimental value of the two-neutron separation energy and charge radius than the INOY. Both potentials however yield a stable ^{6}He against breakup into ^{4}He and two neutrons. This is not the case for ^{8}He. There, only the INOY potential yields a stable configuration, against breakup to

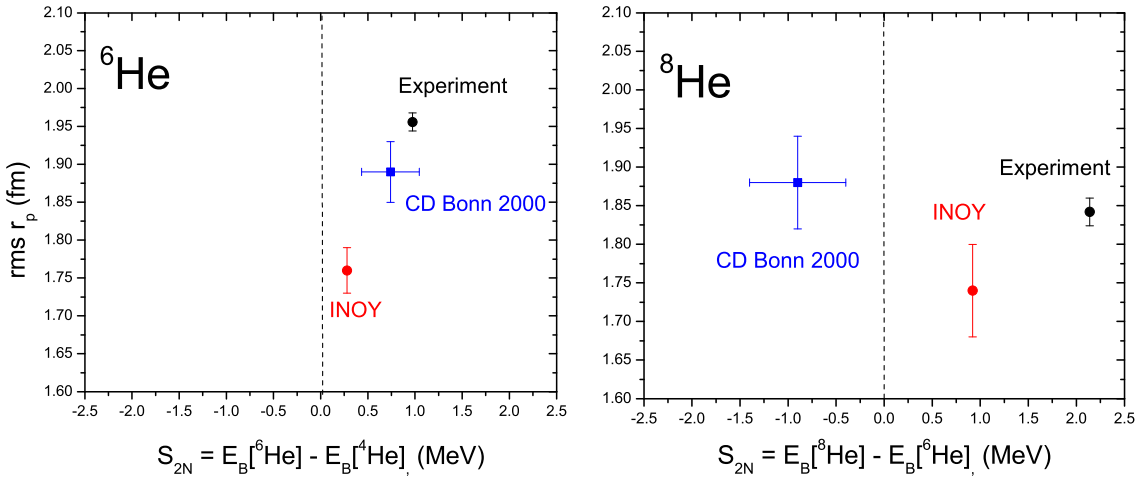

Figure 5.19: NCSM predictions for charge radii and separation energies obtained from [35].

^{6}He and two neutrons. On the other hand, while the CDBonn potential yields an RMS radius which agrees well with the experiment, there is poor agreement with experiment in the case of the INOY potential. It therefore appears that the CDBonn potential yields an under bound ^{8}He, and very likely ^{6}He as well. This is in fact not surprising, as the CDBonn consists of only the two-body force, and, as we discussed in section 2.2.1, the three-body force is required to allow for the binding of nuclei with $A \geq 3$. No three-nucleon forces are incorporated. The INOY was studied because of the idea that the short range non-localities introduced in the potentials would incorporate the effect of the three (and higher) body forces between nucleons [35].

While it is conceivable to perform a NCSM calculation using the CDBonn potential—augmented with a 'three-body' force, the computational challenges are significantly increased and have not currently been done for the helium nuclei. The results from [35] then indicate the limit to which the INOY potential, captures the essential interactions that govern the properties of the neutron-rich helium isotopes.

Pieper and Wiringa, in [126, 125] used the Greens Function Monte Carlo approach along

with the Argonne v18 + Illinois series of 3 body forces to describe the helium isotopes. A correlation plot of the calculated RMS charge radii for ^{6}He and ^{8}He along with the two-neutron separation energies S_{2n} obtained from those calculations is shown in figure 5.20. Two different three-body forces were used in their calculations; namely the Illinois-2 and the Illinois-6. The parametrization are described in more detail in [126].

We note that because of the variational nature of their calculation, every calculation has a slightly different initial wavefunction. Consequently, the initial spread of the starting wave function leads to the final distribution of the observables of interest. This spread was used to assign the theoretical uncertainty in a manner described in [126]

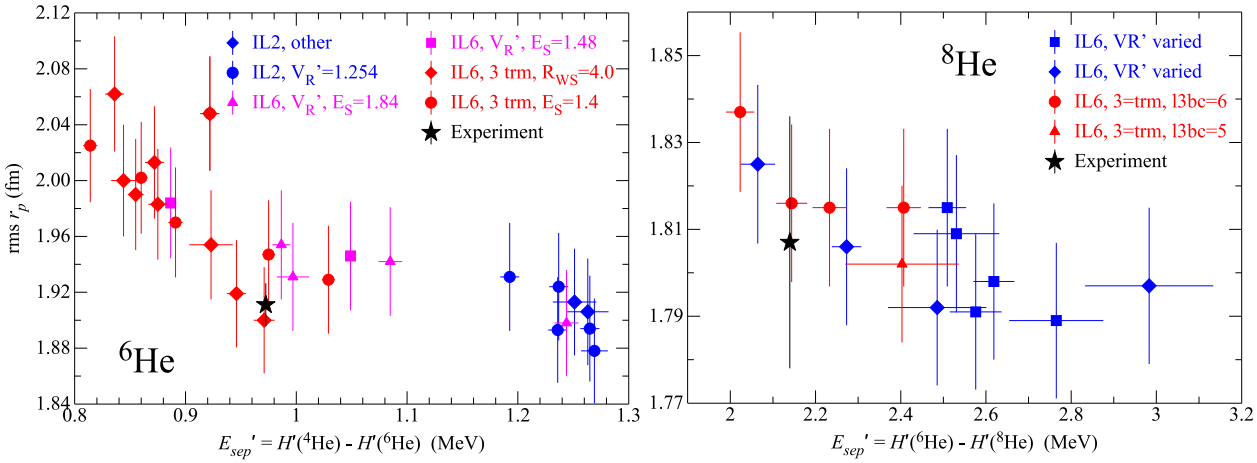

Figure 5.20: GFMC predictions for charge radii and separation energies obtained from [126]. Note the difference in scale between this and figure 5.19

As is evident from the correlation plot in figure 5.20, the GFMC calculations with Argonne v18 + IL6 yield ^{6}He and ^{8}He nuclei which are bound against break-up to ^{4}He + 2n and ^{6}He + 2n respectively.

5.11.1 Charge Radii Trends

Now that the charge radii of all the helium nuclei have been determined, we can consider the trend as we move from A = 3, to A = 8. This is shown in figure 5.21.

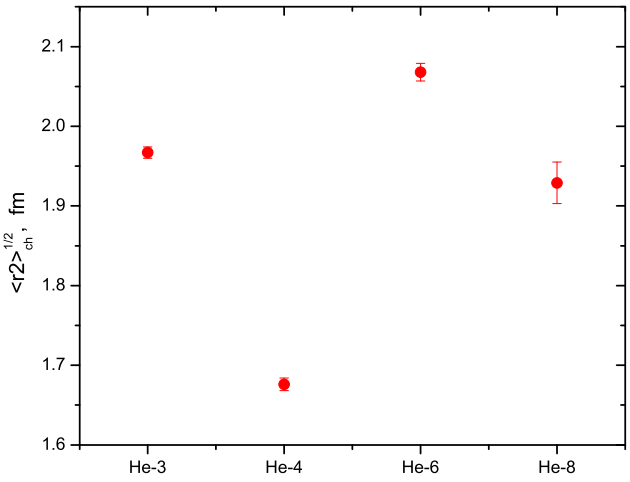

Figure 5.21: Charge radii for the helium isotopes.

Property	^{3}He	^{4}He	^{6}He	^{8}He	Units
E_B	7.718	28.296	29.268	31.408	MeV
E_B/A	2.572	7.073	4.878	3.926	MeV
S_n	7.718	20.577	1.860	2.574	MeV
S_{2n}	-	-	0.972	2.140	MeV
S_p	5.493	19.813	22.590	24.830	MeV

Table 5.8: Binding energies and associated properties of the helium isotopes. The binding energy E_B, binding energy per nucleon E_B/A, one neutron S_n, two neutron separation energy S_{2n} and proton separation energy S_p of the helium isotopes are given. Values obtained from [11, 12]

We see that the charge radius of the stable nuclei ^{3}He is larger than ^{4}He. As we go up in mass, we note that the ^{6}He charge radius is larger than that of ^{4}He. The ^{8}He charge

radius is similarly larger than ^{4}He, though it is notably smaller than ^{6}He. In making sense of this trend, we recall that the charge distribution is given mostly by the protons, and that all four isotopes have the same number of protons. One working picture of ^{6}He and ^{8}He is that they are systems with two and four valence neutrons which surround an alpha particle core. Such neutrons would form a halo as has been suggested from the interpretation of scattering results by Tanihata *et al.* [158] and Alkhazov *et al.* [5], as described in section 3.2. A larger charge radius can therefore arise as a consequence of the motion of the alpha particle core about the center of mass of the system. If that is the case, then the extent of this motion about the center of mass depends on the spatial correlation of the valence neutrons in the halo. For example, a configuration where the neutrons are symmetrically distributed in space on opposite sides of the alpha particle would lead to a smaller motion of the core than if the two neutrons were correlated such that there was a tendency that the two neutrons are closer to each other.

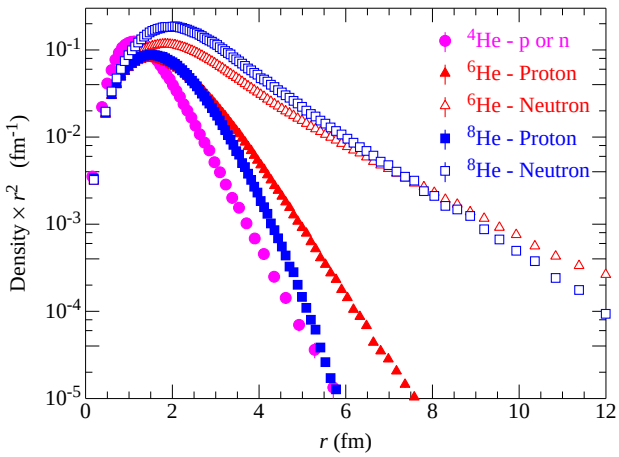

Figure 5.22: Calculated density distributions from [126].

Another mechanism that could lead to enhanced charge radii for some isotopes is that perhaps the alpha particle is significantly perturbed by the presence (or absence in the case of ^{3}He) of the additional neutrons. To answer that question, Pieper and Wiringa calculate the function ρ_{pp}, which is proportional to the probability of finding two protons a given

distance apart. Recall in section 2.1, that we defined the point proton distribution

$$\rho_p(r) = \frac{1}{4\pi r^2} \left\langle \Psi_N \middle| \sum_i^A \frac{1+\tau_{iz}}{2} \delta(r - |\mathbf{r_i} - \mathbf{R_{cm}}|) \middle| \Psi_N \right\rangle \tag{5.7}$$

As given in [128], the proton-proton distribution function is similarly defined as

$$\rho_{pp}(r) = \frac{1}{4\pi r^2} \left\langle \Psi_N \middle| \sum_{i<j}^A \frac{1+\tau_{iz}}{2} \frac{1+\tau_{jz}}{2} \delta(r - |\mathbf{r_i} - \mathbf{r_j}|) \middle| \Psi_N \right\rangle \tag{5.8}$$

An important point is that ρ_{pp} is not sensitive to the center of mass effect. As such, if the core of the helium isotopes is not distorted by adding or removing additional neutrons, the ρ_{pp} distributions should be the same [128].

We plot results of $r^2\rho_{pp}$ in figure 5.23. This illustrates the fact that the protons in ^{3}He are on average further apart than in the even isotopes. However, the proton-proton correlation ρ_{pp} does not explain the trend in size between ^{4}He, ^{6}He and ^{8}He. The average separation of the protons in the even isotopes is similar and does not lead to the 5 % decrease in charge radius measured. The large separation of the protons in the ^{3}He nucleus is related to the rather small binding energy per nucleon of ^{3}He, which is 2.57 MeV compared to 7.07 MeV for ^{4}He/. That the binding of ^{4}He is so large is related to its being a magic nucleus leading to the especially tight binding of the alpha particle. The trends in binding energies for the helium isotopic chain is given in table 5.7.

Calculations of ρ_p using the GFMC explicitly reproduce the trend in r_p—predicting the trends observed. The function $r^2\rho_p$ for the helium isotopes is given in figure 5.22. In addition, it also predicts a neutron distribution with long tails—in support of the neutron halo interpretation. We therefore conclude that the increase in RMS charge radius from ^{4}He to ^{6}He and the decrease from ^{6}He to ^{8}He is due to the motion of the α particle core about the center of mass of the nucleus, and that the neutrons are spatially correlated to be close

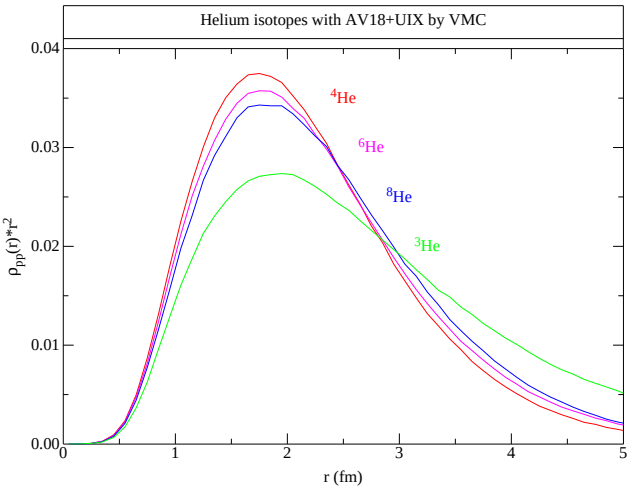

Figure 5.23: Two body density distribution obtained from the AV18 + UIX potentials using the Variational Monte Carlo approach. Figure provided by [169]

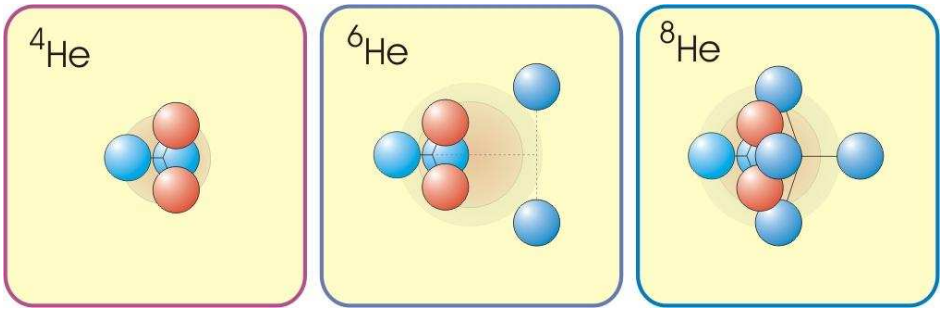

Figure 5.24: Cartoon of nucleons in helium isotopes

to each other as given in figure 5.24.

CHAPTER 6

HELIUM - 3 SPECTROSCOPY

We have reported isotope shifts measurements on the 2^3S - 3^3P transition between ^4He and ^6He [165], and also between ^4He and ^8He [114] by performing spectroscopy on single atoms held in a magneto-optical trap. These measurements probe the difference of the mean square charge radii of the two isotopes. In order to fully understand systematic effects inherent in the trap based technique, it is desirable that a ^4He and ^3He isotope shift measurement be made in the trap and compared with a more precise result obtained using a different technique. Marin *et al.* have reported the most precise ^3He - ^4He isotope shift result on the 2^3S - 3^3P transition [105]. They performed laser spectroscopy in a vapor cell, obtaining the isotope shift with an uncertainty of 165 kHz. However, using the trap based technique, we obtained an uncertainty in the isotope shift of 100 kHz [164]. This is a more precise value than the best published value [105]. As a result, we embarked on making an independent atomic beam measurement of the isotope shift on this transition. In so doing, we also made improved measurements of the 3^3P_J hyperfine intervals in ^3He.

6.1 Experimental Details

The experimental scheme involves carrying out Doppler-free fluorescence spectroscopy on a metastable helium atomic beam. This setup is identical to that used to measure the ^4He fine structure on the 3^3P manifold as reported by Mueller *et al.* [115]. The metastable $1s2p2^3S_1$ level (lifetime $\sim$ 2 hours) is populated by electron bombardment of ground state helium atoms in an RF driven discharge. A mixture of He and Kr gas (partial pressure: 1×10^{-7} and 5×10^{-7} Torr respectively) is passed through the discharge region where the $2\ ^3S_1$ state is populated. About 1×10^{-5} of the helium ground state atoms are excited to the metastable state.

The intensity of the metastable atomic beam is increased by cooling the RF discharge with liquid nitrogen. In addition, two dimensional transverse laser cooling is carried out using the 1s2s $^3S_1$ to 1s2p $^3P_2$ cycling transition for ^{4}He at 1083 nm. For ^{3}He, the 2 $^3S_1, F = 3/2$ to 2 $^3P_2, F = 5/2$ transition is used. The atomic beam then passes through a collimator (length:diameter aspect ratio $\sim$ 200) and a flight path of 1.8 m, after which it enters a magnetically shielded region. There it is overlapped by a pair of counter-propagating laser beams of wavelength $\lambda = 389$ nm. Transitions from the 2 $^3S_1$ metastable state to different 3 ^3P states are then excited by scanning the frequency of the 389 nm light. The counter propagating spectroscopy beams are linearly polarized in the y direction as shown in figure 6.1

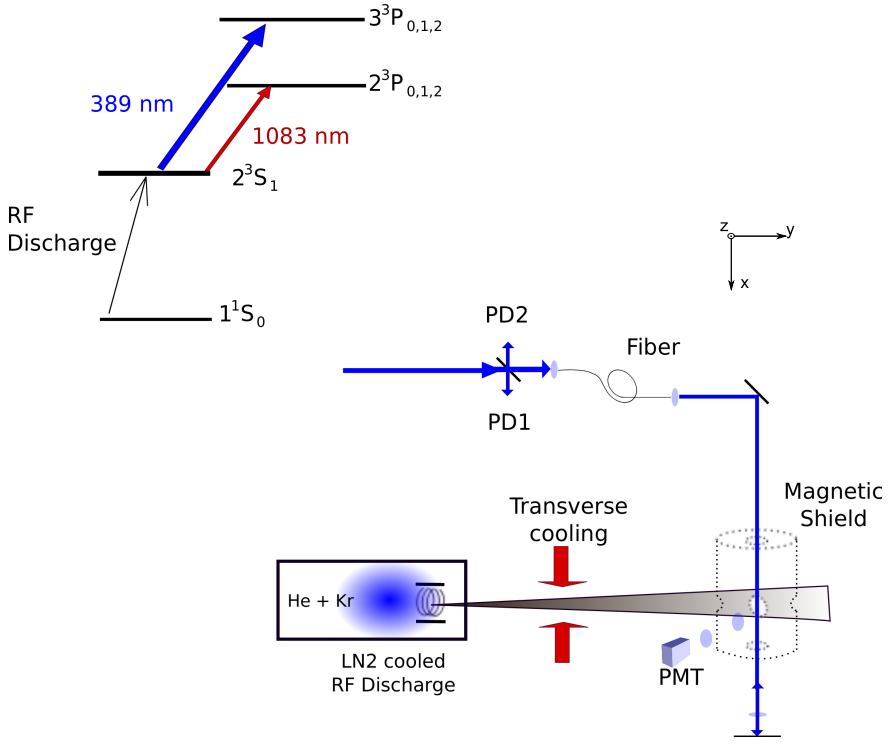

Figure 6.1: Schematic of the experimental setup. A metastable helium beam is obtained from an RF discharge and overlapped with a 389 nm spectroscopy beam in a magnetically shielded region. A simplified level scheme is shown in the top left corner of the figure, along with the 1083 nm, and 389 nm laser used for transverse cooling and spectroscopy

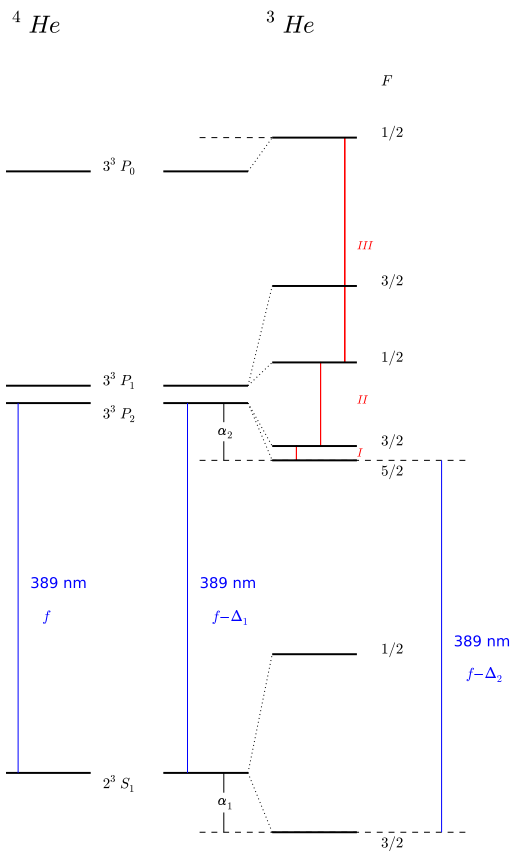

Figure 6.2: Levels in the 2^3S and 3^3P manifold for ^{3}He and ^{4}He. The intervals designated by Roman numerals are the hyperfine intervals for which we report improved measurements. In order to determine the isotope shift between ^{3}He and ^{4}He, we need to consider the hyperfine shift of the $2^3S_1; F = 3/2$ and $3^3P_2; F = 5/2$–designated as α_1 and α_2 respectively. From [113], $\alpha_1 = -2246.5873$ MHz and $\alpha_2 = 2162.785$ MHz. As discussed in [113], the errors on these shifts are less than 0.1 kHz and 1 kHz for α_1 and α_2 respectively. They are hence negligible when compared with the experimental uncertainties.

6.1.1 Laser System

The light required for transverse cooling is generated by means of a home built temperature stabilized diode laser system. Frequency control is attained by locking the laser to the same helium transition for transverse cooling using saturation spectroscopy in a vapor cell [164].

The 1083 nm light is further amplified by injection locking a Keyopsys fiber amplifier yielding ∼1 W of the 1083 nm light for use in the experiment.

For spectroscopy on the 2^3S to 3^3P transition, 389 nm light is generated by frequency doubling light emitted from an external-cavity diode laser which operates at 778 nm, referred to henceforth as LD1. We achieve a long term frequency stability of LD1 by effectively implementing a transfer lock via a fabry-perot cavity to a molecular iodine line. LD1 is locked to the cavity. The cavity is locked to LD2 which is locked to a saturation spectroscopy feature of a molecular I_2 line. As we scan an offset AOM, we monitor the relative frequency of LD1 by measuring a beat note frequency between LD1 and LD2. The setup is described in chapter 5.

About 1 mW of 389 nm light is produced. It is then spatial filtered and transferred near the interaction region by an optical fiber. The emerging beam is expanded to approximately 1 cm diameter and carefully aligned to be perpendicular to the atomic beam. A cat's-eye reflector on the far side of the vacuum chamber ensures that the beam is retro-reflected. This arrangement of optics makes the retro-reflection immune to small angle steering of the input probe beam. The quality of the retro-reflection is monitored by looking at a reverse transmission of light through the optical fiber. A fringe pattern is observed on PD2 which arises as a result of the interference of light reflected from the front end of the optical fiber with the light which was reflected by the cat's eye reflector. By maximizing the contrast of the interference fringes, a good overlap of the input probe beam and its retro-reflection is obtained.

6.1.2 Measurement/Detection Scheme

In order to obtain a spectrum, resonant fluorescence from the atomic beam is detected as the frequency of the probe light is changed. A pair of lensesj forms an image the laser induced

fluorescence of the 389 nm light from the atoms in the atomic beam onto a photo-multiplier tube (PMT). In a period of about 2 minutes, the probe light is scanned over an interval of 30 MHz across the resonance by discretely changing the RF frequency of the frequency shifting AOM in the path of LD1. At each frequency step, the PMT counts, beat frequency between LD1 and LD2, and relative power of 389 nm light is recorded.

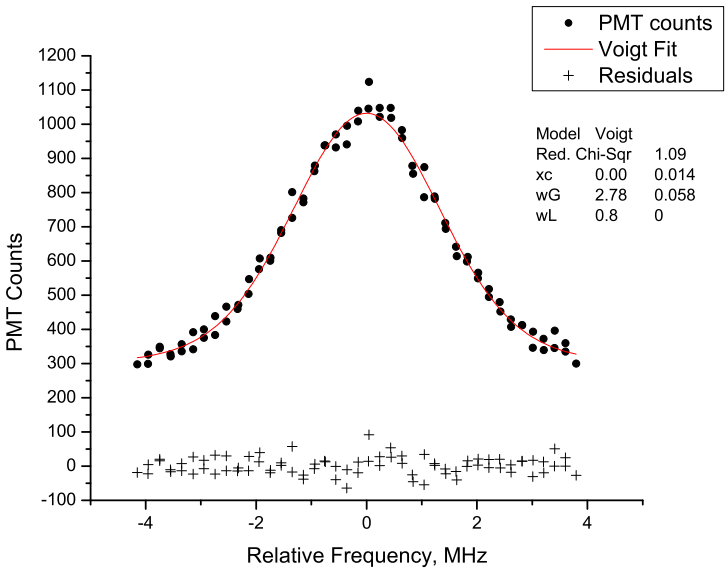

Figure 6.3: Typical spectrum obtained in two minutes. A Voigt fit is shown along with the fit residuals.

For each isotope, we measure the frequencies of different transitions from a common 'ground' state; namely the 2^3S_1 state for ^{4}He and the $2^3S_1, F = 3/2$ state for ^{3}He. Hyperfine structure intervals are thus obtained by taking differences in the transition frequencies from the 'ground' state to each of the two hyperfine states in the interval of interest. Figure 6.2 shows the hyperfine intervals that we measured. They are indicated by the Roman numerals I, II, and III. For the ^{4}He - ^{3}He isotope shift, the 2^3S_1 to 3^3P_2 transition in ^{4}He (designated as f), is compared with the $2^3S_1, F = 3/2$ to $3^3P_2, F = 5/2$ in ^{3}He (designated as $f - \Delta_2$).

Each spectral line obtained is fit using a χ^2 minimization to a Voight profile whose

Lorentzian width is constrained to the natural line width of the transition. The uncertainty on the fit ranges betweeen 10 to 100 kHz.—depending on the line being measured, and the intensity of the probe light. We obtaine reduced χ^2 values ~ 1 for most of the fits. At each probe intensity, we measure each line center about four times. We take the weighted average of the four measurements as the central value for a particular probe intensity, and their standard deviation as the statistical uncertainty.

Two spectra are obtained in sequence. One with the retro-reflected beam blocked (i.e. one beam, 'OB' configuration) and the other with the retro-reflected beam unblocked (i.e. two beam, 'TB' configuration). A difference in the line center frequency of the OB and TB spectrum would suggest a deviation from the orthogonal alignment between the probe laser and the atomic beam. By iteratively measuring the line center for the OB and TB cases while changing the angle between the probe beam laser and the atomic beam, the condition of perpendicular alignment is obtained. This is illustrated in figure 6.4

From figure 6.4, we note that the TB line center is insensitive to the change of the angle between the laser and atomic beam. On the other hand, the position of the OB lines moves dramatically when that angle is varied. This is because in the TB configuration, the Doppler shift due to a misalignment results in two peaks which are symmetrically shifted about the center frequency. This leads to a broadening of the line, but not a shift. The ideal measurement position is therefore the angle where the two configurations lead to the same value for the line center.

Now, momentum is transferred to the atoms from the photons with each photon absorption and re-emission cycle. As a result, there is a net momentum transfer to the atoms in the OB case which results in a shift of the line center. In principle this shift tends to zero for a TB configuration, as the net momentum transfer vanishes if the beam and its retro-reflected partner are balanced. In order to eliminate the perturbation due to radiation pressure of the light, we measure the spectrum of each line at intensities ranging from $2 \times 10^{-3}\ I_s$ to

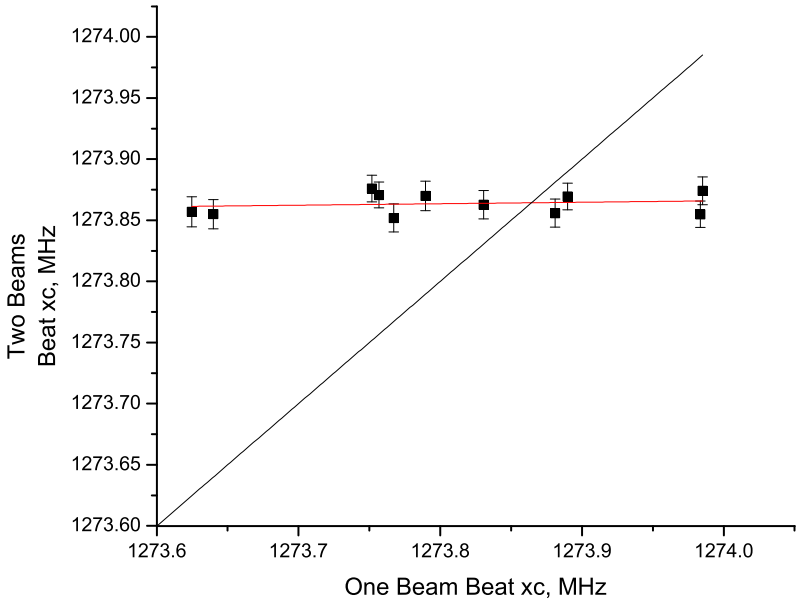

Figure 6.4: Shifts in the line centers as the angle between the probe beam and the atomic beam is varied through an angle of 1 radian. Notice that the OB spectrum is sensitive to the residual Doppler shift, which is absent in the TB case.

$8 \times 10^{-3}\ I_s$. The saturation intensity for this transition is $I_s = 3.33$ mw/cm^2. We then extrapolate the power dependent line center values to the 'zero intensity' condition. We refer to a set of power dependent frequency measurements as a 'series'. In evaluating the frequency of a hyperfine interval, we take the difference of the zero intensity intercepts of the two transitions—propagating the errors accordingly. Results are given in tables 6.2 and 6.3. The reported frequency of each interval is the average of three to four series. We show a plot of the power dependence of line center frequencies in figure 6.5, as well as the series average contributing to the isotope shift in figure 6.2.2.

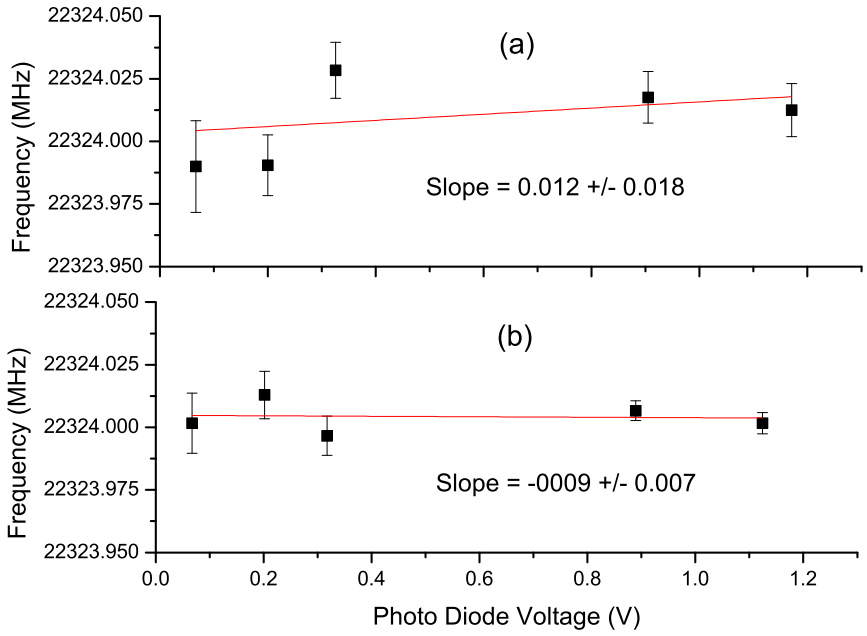

Figure 6.5: Left figure:Dependence of Line Center position on the intensity of the probing laser. Panel (a.) Probe laser not retro-reflected. Panel (b.) Probe laser retro-reflected.

6.2 Results / Error Analysis

6.2.1 Systematic Error Budget

Laser spectroscopy in an atomic beam is a favorable technique because it is free from many systematic effects. In particular, it is substantially less sensitive to pressure shifts associated with vapor cell techniques [173] or to Zeeman shifts that can arise in magneto - optical trap based schemes [164]. In our experimental setup, the interaction region is enclosed in a magnetically shielded region, where the earth's magnetic field is attenuated by up to a factor of 100. The total field is less than 3mG in the center of the shield. It should be noted that the probe beam is linearly polarized. Therefore, the presence of a non zero magnetic field will, to the first order only broaden the line and not shift it. Based on the magnetic field

attenuation and the Zeeman shift of 1.4 MHz/Gauss, the maximum systematic error due to Zeeman shifts for each transition measured is estimated conservatively to be 5 kHz.

Systematic errors due to Doppler shifts are estimated from the difference between line center frequencies obtained from the OB and TB configurations. If a difference between the OB and TB configurations is measured, an estimate for the maximum Doppler shift is obtained by multiplying the difference between the line centers with the maximum slope of the correlation plot shown in figure 6.4. Using this procedure, we attribute uncertainties of 5 kHz to hyperfine intervals due to the steering of the probe beam. For the isotope shift measurement, we assign a possible systematic error of 10 kHz due to Doppler shifts. This is larger than for the hyperfine intervals because of the mass dependence of the Doppler shift.

Light pressure shifts refer to shifts of the resonant frequency due to an imbalance of beams, leading to the pushing of atoms. Because of our procedure for using a balanced pair of beams for probing and extrapolating to zero intensity, we conservatively estimate systematics due to light pressure shifts to be less than 3 kHz. Other sources of possible systematics are estimated to be less than 3 kHz.

Table 6.1: Systematic Error budget for the hyperfine intervals and isotope shift measurements reported

Effect	Hyperfine Intervals (kHz)	Isotope Shift (kHz)
Zeeman Shifts	5	5
Doppler Shift	5	10
Light Pressure Shift	3	3
Other effects	< 2	< 3
Total	10	13

6.2.2 Isotope Shift

The presence of hyperfine structure in the ^{3}He spectrum complicates the analysis of an isotope shift measurement between ^{3}He and ^{4}He. In figure 6.2, we show the hyperfine levels in ^{3}He with respect to the unperturbed ^{3}He fine structure levels. In [113], the hyperfine shifts are calculated as perturbations due to the hyperfine interaction from these levels. The shifts of $2^3S_1, F = 3/2$ and $3^3P_2, F = 5/2$–designated as α_1 and α_2 in the figure are given in [113], as $\alpha_1 = -2246.5873$ MHz and $\alpha_2 = 2162.785$ MHz.

We desire to determine Δ_1, the isotope shift in the absence of hyperfine structure. In order to do so, we measure the frequency difference between the 2^3S_1 - 2^3P_2 transition in ^{4}He (which we designate as f) and the $2^3S_1, F = 3/2$ - $3^3P_2, F = 5/2$ transition in ^{3}He (which we designate as $f - \Delta_2$). Δ_1 and Δ_2 are related by the equation:

$$\begin{aligned} \Delta_1 &= \Delta_2 - (\alpha_1 + \alpha_2) \\ &= \Delta_2 + (2246.5873 - 2162.785)\ \text{MHz} \\ &= \Delta_2 + 83.802\ \text{MHz} \end{aligned} \tag{6.1}$$

Four series of measurements were made for the frequencies of the transition in ^{4}He and ^{3}He. The weighted average of the measurements performed yields $\Delta_2 = 42100.388(9.6)(13)$ MHz. Applying equation 6.1, we obtain Δ_1.

6.2.3 Recoil Correction

We consider the contribution of the differential recoil frequencies of the two atoms on absorbing and emitting a 389 nm photon on the isotope shift. This recoil frequency is given by $f_{rec} = \hbar k^2/4\pi M$, with ^{3}He $\mathrm{f_{rec}}$ $-^4$ He $\mathrm{f_{rec}} = 108$kHz. This is rather large (due to the light mass of the isotopes involved) and is a substantial fraction of our measurement uncertainty.

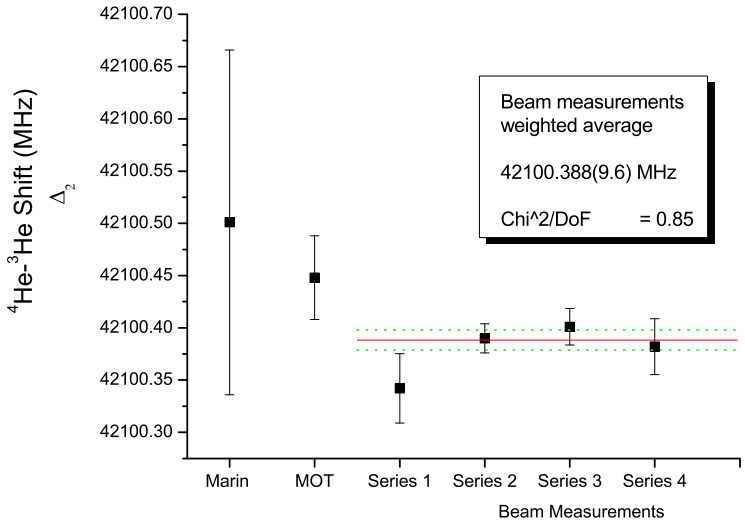

Figure 6.6: Results of the measurements of ^{4}He and ^{3}He denoted as Δ_2. This is compared with the result from [105] and [164]. The quoted uncertainty is purely statistical.

We therefore add a correction of 108 kHz to Δ_1, obtaining a final value of the isotope shift, $\Delta_1 = 42184.298(16)$ MHz

Our derived isotope shift value is compared with the value obtained by the trap based method, and with the literature value in table 6.2

Table 6.2: 3He - 4He Isotope Shift for the 2S - 3P transition. In MOT, the error is dominated by the uncertainty in the hyperfine shift α_2 shown in figure 6.2.

Method	Frequency in MHz	reference
Vapor Cell	42184.321(165)	Marin *et al.* [105]
MOT	42184.268 (100)	Wang [164]
Atomic Beam	42184.298 (16)	this work

Table 6.3: Hyperfine interval measurement results. The quoted uncertainty is the combined statistical and systematic uncertainty. The statistical errors for the intervals I, II, and III were 37, 31 and 68 kHz respectively.

Interval	Transition	This Work (MHz)	Marin *et al.* (MHz)
I	$3\ ^3\mathrm{P}_2, F = 5/2$ - $3\ ^3\mathrm{P}_2, F = 3/2$	542.343(38)	
II	$3\ ^3\mathrm{P}_2, F = 3/2$ - $3\ ^3\mathrm{P}_2, F = 1/2$	3165.042(32)	
III	$3\ ^3\mathrm{P}_1, F = 1/2$ - $3\ ^3\mathrm{P}_0, F = 1/2$	8510.725(68)	8150.864(276)
I+II		3707.380(49)	3706.902(240)

6.2.4 Hyperfine Interval Results

We measured the hyperfine intervals of levels in the 3P manifold indicated in figure 6.2. Each hyperfine interval that we measured was obtained as an average of two or three series of measurements. Like in the determination of the hyperfine shift, Each series comprises of a set of power dependent measurements with an extrapolation to zero intensity. Systematic errors are accounted for as described in section 6.2.1. Table 6.3 gives a summary of results obtained. The quoted uncertainties in parenthesis are the combined statistical and systematic errors.

CHAPTER 7

HYPERFINE SUPPRESSION OF TRANSITIONS IN HE-3

We have published the contents of this chapter before in [154]. The text is reproduced verbatim.

Due to its simplicity, the helium atom has been a proving ground for precision atomic measurements and calculations of few-body quantum systems. The knowledge gained from this effort is used to test bound-state quantum electrodynamics [112, 113, 121], determine the fine structure constant [173, 70], and explore exotic nuclear structure [165, 114, 147, 105]. We report results of a combined theoretical and experimental study on the strengths of $2\ ^3\mathrm{S}_1 - 3\ ^3\mathrm{P}_J$ transitions in ^{3}He.

Surprisingly, we observe that the strengths of two "allowed" transitions, $2\ ^3\mathrm{S}_1, (F = \frac{3}{2}) - 3\ ^3\mathrm{P}_1, (F = \frac{3}{2})$ and $2\ ^3\mathrm{S}_1, (F = \frac{1}{2}) - 3\ ^3\mathrm{P}_2, (F = \frac{3}{2})$, are 1,000 times weaker than that of the strongest transition $2\ ^3\mathrm{S}_1, (F = \frac{3}{2}) - 3\ ^3\mathrm{P}_2, (F = \frac{5}{2})$. The level scheme showing these transitions is presented in Fig 7.1. This dramatic suppression of transition strengths is due to a rare atomic phenomenon: within the $3\ ^3$P manifold, the hyperfine interaction is comparable to or even stronger than the fine structure interaction. Consequently the conventional model based on LS-coupling is no longer applicable. Rather, we find that an alternative model where the fine structure interaction is treated as a perturbation on states obtained by first coupling nuclear spin to the total electron spin provides a good qualitative explanation of the observed suppression. We refer to this coupling scheme as IS-coupling. We start by discussing the details of the experiment and compare the data with the predictions from the different coupling schemes. Finally, we discuss an exact diagonalization method to account for the small differences between experiment and the IS-coupling scheme.

We measure the ratio of transition strengths using a cross-beam laser induced fluorescence method. A beam of metastable helium atoms in the $2\ ^3\mathrm{S}_1$ state is prepared in a liquid-

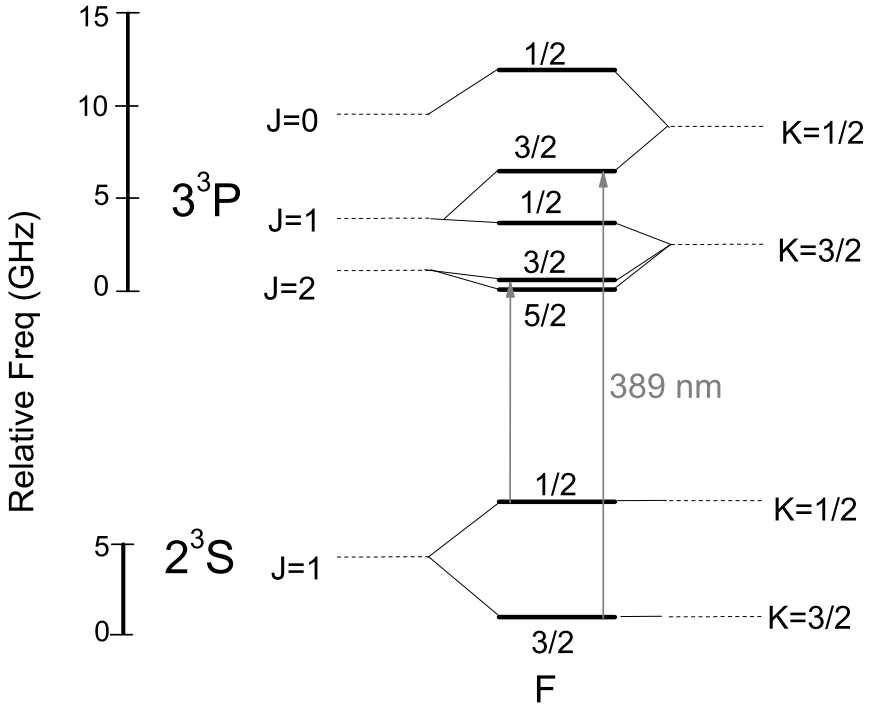

Figure 7.1: Level scheme of ^{3}He showing the levels investigated, with the arrows indicating the suppressed transitions observed. The level positions are drawn to scale within each manifold. The large hyperfine splitting with respect to the fine structure splitting is evident. With a nuclear spin $I = 1/2$ for ^{3}He, the levels are designated by the familiar term symbols, with $\mathbf{J} = \mathbf{L} + \mathbf{S}$, $\mathbf{F} = \mathbf{J} + \mathbf{I}$ on the left. The levels are labeled on the right using the quantum number $\mathbf{K} = \mathbf{I} + \mathbf{S}$, $\mathbf{F} = \mathbf{K} + \mathbf{L}$.

nitrogen cooled RF-driven discharge. A retro-reflected beam of linearly polarized 389 nm light is incident perpendicular to the atomic beam. The polarization of the light is along the direction of the atomic beam. A uniform external magnetic field of 5 Gauss is applied along the direction of the laser to provide an axis of quantization. As the frequency is scanned across different resonances, the atoms are excited, and fluorescence from the atoms is detected in the direction normal to the atomic and laser beams. The metastable atomic beam is collimated using a collimator, made of a stack of microscope cover slips which provides high collimation in the direction along the laser beam [71]. We are able to obtain Doppler broadened lines of 20 MHz line width. The natural line width of the transitions is

1.6 MHz. Approximately 4 mW of 389 nm light is obtained by frequency doubling infrared light at 778 nm. The frequency of the 778 nm light is referenced to a temperature stabilized Fabry-Perot cavity. The power of the laser and its wavelength are monitored continuously.

The nine E1 allowed transitions are repeatedly probed in a random order and the spectra are recorded. Each spectrum is fitted using a statistically weighted Voigt profile. The integrated area of the profile divided by the power of the probing laser beams is taken as a measure of the transition strength. As the absolute atomic beam flux and efficiency of detecting the fluorescence photons are not measured in this experiment, only the ratios of transition strengths are determined. By defining the strength of the strongest transition, $2\ ^3\mathrm{S}_1, (F = \frac{3}{2})\ -\ 3\ ^3\mathrm{P}_2, (F = \frac{5}{2})$, to be unity, we determine the relative strengths of the other eight transitions. The results are presented in Fig. 7.2 and in Table 7.1.

The intensity of the probing laser beam is varied depending on the transition under study. For example, when probing the two highly suppressed transitions, the intensity of the probe is increased by two orders of magnitude. In all cases, however, the laser intensity is kept well below the saturation intensity of the particular transition under study. Indeed, the intensity is chosen so that on average less than one photon is scattered by each atom as it passes the laser beams in approximately 2 μs. This is to avoid nonlinear effects in the measurements due to optical pumping and mechanical effects of the light on the atomic beam. Such systematic effects are studied by examining the dependence of transition signal on the laser beam power. Additional corrections are made and systematic errors generated due to changing background in the measured laser power and the anisotropic angular distribution of the fluorescence emission. The final error estimates are given in Table 7.1.

The textbook strategy [150] to estimate theoretically the atomic transition strengths is based on the presumed hierarchy that hyperfine splittings be small in comparison with fine-structure splittings. Consequently approximate eigenstates of the total Hamiltonian may be constructed by first coupling L (total orbital angular momentum quantum number) and

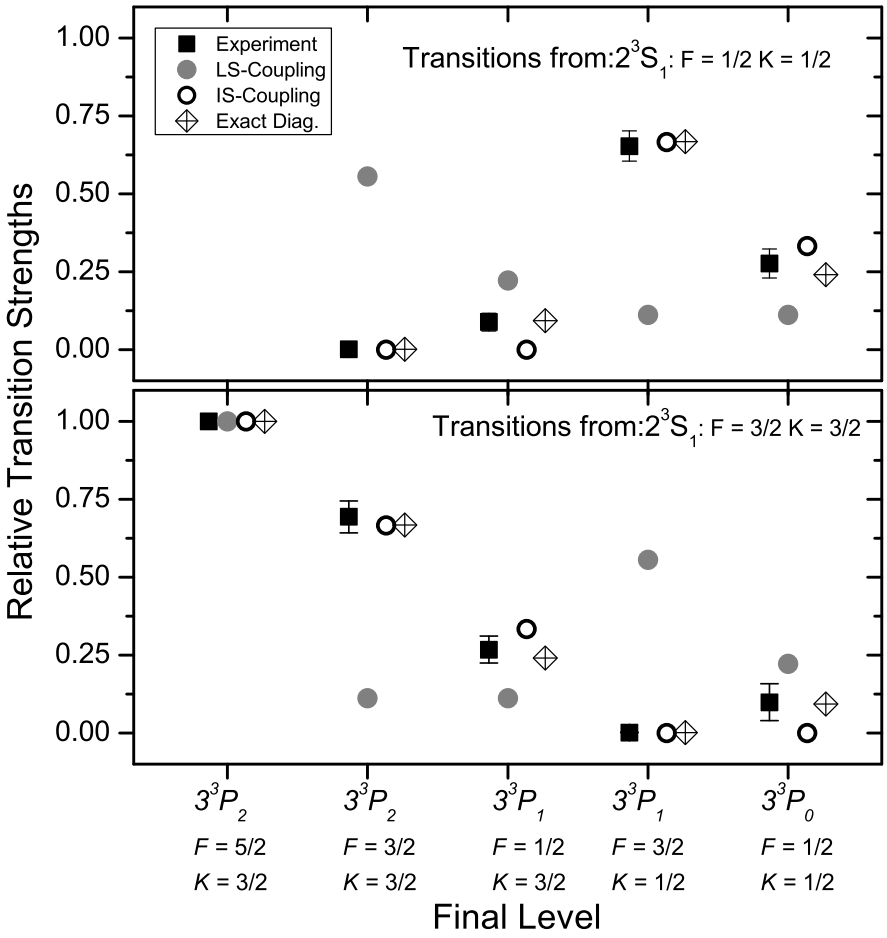

Figure 7.2: Comparison of relative transition strengths for all E1 allowed transitions between the 2 ^{3}S$_1$ and 3 ^{3}P$_J$ manifolds. All values are normalized with respect to the 2 ^{3}S$_1$, $(F = \frac{3}{2}) - 3\ ^3P_2$, $(F = \frac{5}{2})$ transition.

S (total electronic spin quantum number) to form the total electronic angular momentum J; coupling J and I (nuclear spin quantum number) then gives the total atomic angular momentum F. Within this LS-coupling model, the total strength for an electric dipole transition may be evaluated using standard angular momentum algebra [60].

The results of this LS-coupling model are compared with the experimental data in Fig. 7.2. It is apparent that there is not even qualitative agreement. The origin of the failure of the LS-coupling model may be understood as follows. In ^{3}He, the hyperfine struc-

Table 7.1: Relative transition strengths for all E1 allowed transitions between the $2\ ^3\mathrm{S}_1$ and $3\ ^3\mathrm{P}_J$ manifolds. All values are normalized with respect to the $2\ ^3\mathrm{S}_1, (F = \frac{3}{2}) - 3\ ^3\mathrm{P}_2, (F = \frac{5}{2})$ transition.

Initial (J,F) $2\ ^3\mathrm{S}_J$	Final (J,F) $3\ ^3\mathrm{P}_J$	Experiment	LS	IS	Exact Diag.
(1,3/2)	(2,5/2)	1	1	1	1
	(2,3/2)	0.69(5)	0.11	0.67	0.67
	(1,1/2)	0.26(4)	0.11	0.33	0.24
	(1,3/2)	0.0012(2)	0.55	0	0.0010
	(0,1/2)	0.10(5)	0.22	0	0.093
(1,1/2)	(2,3/2)	0.0011(4)	0.55	0	0.0010
	(1,1/2)	0.08(3)	0.22	0	0.093
	(1,3/2)	0.65(4)	0.11	0.67	0.67
	(0,1/2)	0.27(4)	0.11	0.33	0.24

ture is almost entirely due to the magnetic dipole interaction of the tightly bound $1s$ electron with the nucleus. The fine structure is a consequence of both one-body spin-orbit coupling of the excited nL electron and two-body spin-other-orbit and spin-spin interactions of the nL electron with the $1s$ electron [17]. As n increases, the fine-structure splittings decrease as n^{-3}. The hyperfine interaction of the $1s$ electron, on the other hand, tends for large n to the constant hyperfine interaction strength in $^3\mathrm{He}^+$. Note that the hyperfine splitting in the ground state of $^3\mathrm{He}^+$ is 8.7 GHz [66], which is comparable to, or larger than, the level spacings within the $2\ ^3S$ and $3\ ^3P$ manifolds (see Fig. 7.1).

The relative strength of the hyperfine interaction in ^{3}He has been recognized before [67, 159, 46, 68, 25, 131, 161] and has been taken as an indication that a simple angular momentum coupling model describing transitions in ^{3}He is not available and that a numerical diagonalization of an effective Hamiltonian is necessary. We demonstrate in the following

that although n is quite small in the 3 ^{3}P manifold, the assumption of relatively weak fine structure interactions does provide a simple model that allows us to understand qualitatively the strengths of transitions from 2 ^{3}S to 3 ^{3}P.

For 3 ^{3}P, S is still a good quantum number, since the separation of this manifold from 3 ^{1}P is large ($\sim 10^4$ GHz) in comparison with the hyperfine and fine structure splittings. Therefore, the basic idea underlying what we refer to as the IS-coupling model is that the electrostatic exchange interaction between the two electrons preserves **S**; the hyperfine interaction couples **S** and **I** to form a new intermediate angular momentum **K**; and **F** is then obtained by coupling **L** and **K**. In this picture, the ^{3}He eigenstates of relevance here are not labeled in terms of $nLS(J)I, F$, but in terms of $nIS(K)L, F$. An immediate consequence of the fact that the electric dipole operator acts on neither S nor I is that K must be conserved in an $E1$ transition, i.e., $|\langle \Psi^{(n'L'S'I)}_{K'F'} \parallel \hat{D} \parallel \Psi^{(nLSI)}_{KF} \rangle|^2$ vanishes if K differs from K'. A similar model was used in 1933 for a case in which S is not conserved [73], but that appears to be the only other study employing an extreme hyperfine-coupling picture to develop a basic understanding of transition strengths involving hyperfine multiplets.

As shown in Fig. 7.2, there is good qualitative agreement between experiment and the IS-coupling model, thus suggesting that already for $n = 3$, the fine-structure interactions may be considered perturbations to the hyperfine structure. For instance, within the IS-coupling model, the suppression of the transition from 2 ^{3}S$_1$, $F = \frac{3}{2}$ ($K = \frac{3}{2}$) to 3 ^{3}P$_1$, $F = \frac{3}{2}$ ($K = \frac{1}{2}$) follows from the K-selection rule in $E1$ transitions. On the other hand, according to experiment, the transition from 2 ^{3}S$_1$, $F = \frac{3}{2}$ ($K = \frac{3}{2}$) to 3 ^{3}P$_0$, $F = \frac{1}{2}$ ($K = \frac{1}{2}$) is weakly allowed, in slight deviation from the IS-coupling model. We note that the observed suppressions for certain transitions from 2 ^{3}S to 5 ^{3}P [25, 161] are fully consistent with the K-selection rule.

In order to characterize the nature of the perturbations to the IS-coupling model for ^{3}He, and account for the slight deviations, we have performed an exact diagonalization of

the total Hamiltonian H within the manifold of 3 ^{3}P and 3 ^{1}P states, including both fine and hyperfine structure. The total Hamiltonian of ^{3}He in the absence of external fields is of the form

$$H = H_{\rm NR} + H_{\rm fs} + H_{\rm hfs} \tag{7.1}$$

where $H_{\rm NR}$ is the non-relativistic Hamiltonian, $H_{\rm fs}$ represents the fine structure interaction for helium as described by many authors (see Drake [50, 51] for a review), and $H_{\rm hfs}$ represents the hyperfine structure interaction, see for example, Bethe and Salpeter [17]. In this picture, $H_{\rm hfs}$ is treated as a small perturbation relative to the large electrostatic splitting between states with different principal quantum number n, and by exact diagonalization within the manifold of strongly mixed states with the same n. The technique is basically the same as that described by Hinds, Prestage and Pichanick [82].

Using these methods, a comprehensive investigation of the fine and hyperfine structure of ^{3}He has recently been carried out by Morton, Wu, and Drake [113]. All fine structure and hyperfine structure parameters required to diagonalize the complete fine and hyperfine interaction matrix in the basis set of singlet and triplet states are accurately calculated by using double basis set variational wave functions in Hylleraas coordinates as described by Drake [50, 51]. For the $3P$ state, instead of using directly the theoretical energies for ^{3}He, we combined the theoretical isotope shifts for ^{3}He relative to ^{4}He [113] with the best experimental ionization energies for ^{4}He.[115, 113]. This gives higher accuracy due to cancellations of the mass-independent QED uncertainties in the calculated isotope shifts.

The final step is to calculate the electric dipole transition line strengths between the perturbed hyperfine states of 2 ^{3}S and 3 ^3P in terms of standard angular momentum theory, in which the perturbed hyperfine states are linearly expanded in terms of unperturbed eigenstates. The expansion coefficients are obtained by the above diagonalization of the

complete matrix. The final results and the comparison with experiment are given in Table 7.1. The calculations show that the mixing between hyperfine states of 3 ^{3}P with different K but the same F of ^{3}He precisely accounts for the deviations shown in Table 7.1 from the *IS*-coupling model. This mixing is due to the fine structure interactions. We find that both the one-body spin-orbit, and the two-body spin-spin and spin-other-orbit interactions must be included, in order to accurately reproduce the strengths. In the case of the $2S$ state, this hyperfine mixing is also important for hyperfine structure, as shown by Riis *et al.* [139], but its contribution to the transition strength is negligible in the present work.

In summary, the hyperfine suppression of 2 $^3\mathrm{S}_1, (F = \frac{3}{2})$ to 3 $^3\mathrm{P}_1, (F = \frac{3}{2})$ and 2 $^3\mathrm{S}_1, (F = \frac{1}{2})$ to 3 $^3\mathrm{P}_2, (F = \frac{3}{2})$ radiative transitions in ^{3}He is caused by a selection rule that emerges in the limit of strong hyperfine mixing between states with the same F but different J. In this limit, the radiative transitions are better described by a coupling scheme in which **I** and **S** are coupled to form **K**, and then **L** is coupled to **K** to form **F**. In this limit, the eigenvalue K is approximately preserved as a good quantum number. The small deviations from the *IS*-coupling scheme are well accounted for by an exact diagonalization for the intermediate coupling case. However, with increasing n, the *IS*-coupling scheme should rapidly become more accurate because the fine-structure interactions decrease in proportion to $1/n^3$, while the hyperfine interactions tend to a constant at the series limit. The surprise is that it already works so well for $n = 3$.

Part II: Studies with Radium

CHAPTER 8

DISCRETE SYMMETRY TESTS WITH PERMANENT ELECTRIC DIPOLE MOMENTS

The symmetry present in a physical system is reflected in the character of the Lagrangian (or Hamiltonian) of the system and the equations of motion used to describe its dynamics. In classical physics, we encounter *continuous* symmetries such as those to do with the isotropy of space, or due to space and time translation. These lead to the conservation of angular momentum, momentum and energy respectively.[1] Other types of symmetries which arise in quantum mechanics are the *discrete* symmetries of charge-conjugation (C), parity (P) and time-reversal (T). Like their continuous counterparts, they also have deep consequences on the dynamics of the systems they describe. The main motivation of the experiments described in Part-II of this thesis is to find evidence for, or set limits on possible T-violation in radium atoms. As we will describe below, we do so by searching for a non-vanishing permanent electric dipole moment (EDM).

We start by briefly considering the symmetry operations of P, C, and T.

(i.) **Parity (P)**: This operation refers to an inversion of space, in which $x \to -x,\ y \to -y,$ and z $\to -$z. In effect, a left handed coordinate system under parity is transformed to a right handed coordinate system. In quantum mechanics, parity is described by the unitary operator P where $|\psi(t,\mathbf{r})\rangle \to P\,|\psi(t,\mathbf{r})\rangle = |\psi(t,-\mathbf{r})\rangle$. If parity is conserved, then the Hamiltonian H commutes with the P. Atomic and nuclear states can be classified based on their parity eigenvalue $\eta = \pm 1$. i.e. $P\,|\psi(t,\mathbf{r})\rangle = \eta\,|\psi(t,\mathbf{r})\rangle$. When the parity operation is applied twice, we return to the initial state. In the same manner

1. The connection between conserved quantities and continuous space-time symmetries is made by Noether's theorem. It is worthwhile noting though that Noether's theorem does not apply to the discrete symmetries. There are therefore no associated conserved quantities associated with discrete symmetries in the same sense.

as for atomic states, one can consider the intrinsic parity of hadrons, which are bound states of quarks and anti-quarks. If parity is conserved in a decay process, then the intrinsic parity of the initial and final state must be the same.

(ii.) **Charge Conjugation (C)**: This operation exchanges a particle with its (charge conjugate) antiparticle. All charges, i.e. electric, lepton number, baryon number etc are exchanged as a result. The concept of charge conjugation assumes a full meaning only in the context of relativistic quantum mechanics, which allows for 'negative energy states' which are identified as anti-particles. Consider for example the pions π^+ and π^-. Under the charge-conjugation operation, $C\,|\pi^+\rangle = |\pi^-\rangle$. We can assign a charge-conjugation eigenvalue (C-parity) $\eta^C = \pm 1$ for particles which are their own anti-particles such as the photon or π^0. For example, a photon has $\eta^c = -1$ because under charge conjugation, electric charges switch sign and therefore so do electric and magnetic fields. Because π^0 can decay into two photons via the EM interaction, $\pi^0 \to \gamma + \gamma$, we infer the C-parity of π^0 to be $\eta^c = +1$. Charge conjugation symmetry therefore limits the available decay modes of particles. Consequently, a class of tests of charge conjugation symmetry involves looking for decays which violate C.

(iii.) **Time-Reversal (T)**: This refers to the operation where $t \to -t$. As a consequence, under this operation, $v \to -v$; which results in the reversing of the direction of time flow. In quantum mechanics, the time-reversal operation is represented by an anti-unitary operator $T = KU$, where U is a unitary operator which transforms $t \to -t$ and K is the complex conjugation operator [143]. Under the time-reversal operation, T, $|\psi(t, \mathbf{r})\rangle \to T\,|\psi(t, \mathbf{r})\rangle = |\psi(-t, \mathbf{r})\rangle$. In a sense, a time reversal operation is equivalent to motion reversal. However, when considering internal degrees of freedom such as spin, the notion of motion reversal will be inadequate as there is really nothing moving per se [143].

8.1 Lorentz invariance considerations

For a fermion field described by $\psi(x)$, a relativistic quantum theory can be written in terms of a Lagrangian density $\mathcal{L}$, where the Lagrangian

$$L = \int d^3x \ \mathcal{L}(\mathbf{x}, t). \tag{8.1}$$

As in classical mechanics, the equations of motion are obtained from the Euler-Lagrange equations.[2] In general, a Lorentz invariant observable can be written as $\overline{\psi}\Gamma_\alpha\psi$, where the Γ_α refer to the elements of the set of linearly independent anti-symmetric combinations of the Dirac gamma matrices [123].

$$\Gamma \equiv \{1, \gamma_\mu, \sigma_{\mu\nu}/2, \gamma_\mu\gamma_5, i\gamma_5\} \tag{8.2}$$

Based on how Lorentz invariant observables transform under rotations, reflections and boosts, they can be classified as scalar, vector, tensor, axial vector, and pseudo-scalar. These correspond to each of the Γ_α. We give in table 8.1 the transformation properties of the different forms under the transformations C, P, and T.

Consider for example, the QED Lagrangian for a spin-1/2 particle, say an electron, coupled to an electromagnetic field:

$$\mathcal{L}_0 = -\frac{1}{4}F_{\mu\nu}F^{\mu\nu} - \bar{\psi}_e\gamma^\mu[\partial_\mu + ieA_\mu]\psi_e - m_e\bar{\psi}_e\psi_e \tag{8.3}$$

where $F_{\mu\nu}$ are the field strength tensors of the electromagnetic field. $\mathcal{L}_0$ consists of terms which are all Lorentz scalars, and therefore even under C,P, T and combinations of them.

2. We can similarly define a Hamiltonian density $\mathcal{H}$, where the conjugate variable, $\Pi(x) = \frac{\partial\mathcal{L}}{\partial\dot{\psi}(x)}$ and $\mathcal{H} = \Pi\dot{\psi}(x) - \mathcal{L}$ [123]. The equations of motion then follow from Schroedinger's equation

Table 8.1: Transformation properties of fermion bilinears under C, P and D. We use the shorthand $(-1)^\mu \equiv 1$ for $\mu = 0$, and $(-1)^\mu \equiv -1$ for $\mu = 1, 2, 3$ [123]

		C	P	T	CPT
Scalar	$S(x) \equiv \overline{\psi}(x)\psi(x)$	+1	+1	+1	+1
Vector	$V^\mu \equiv \overline{\psi}(x)\gamma^\mu\psi(x)$	-1	$(-1)^\mu$	$(-1)^\mu$	-1
Pseudoscalar	$P(x) \equiv \bar{i}\psi(x)\gamma_5\psi(x)$	+1	-1	-1	+1
Tensor	$T^{\mu\nu}(x) \equiv \overline{\psi}(x)\sigma^{\mu\nu}\psi(x)$	-1	$(-1)^\mu(-1)^\nu$	$-(-1)^\mu(-1)^\nu$	+1
Axial Vector	$A^\mu(x) \equiv \overline{\psi}(x)\gamma^\mu\gamma_5\psi(x)$	+1	$-(-1)^\mu$	$(-1)^\mu$	-1

Now, consider the interaction of the magnetic moment of the particle with a magnetic field

$$\mathcal{L}_\mu = \frac{\mu}{2}\bar{\psi}\sigma_{\mu\nu}\psi F^{\mu\nu} \xrightarrow{non-rel} -\mu\mathbf{B}\cdot\frac{\mathbf{S}}{S} \tag{8.4}$$

Like $\mathcal{L}_0$, $\mathcal{L}_\mu$is also even under P and T.

Assume for a moment that this spin 1/2 particle has a permanent electric dipole moment $\mathbf{d}$. Now, $\mathbf{d} = d\mathbf{S}/S$, since an eigenstate of the particle is characterized by its total angular momentum. In other words, the dipole moment is aligned parallel or anti-parallel to the spin. Were this not so, then an additional quantum number would be required to designate the state. The dipole moment will then couple to an electric field much like a magnetic dipole moment couples to a magnetic field.

$$\mathcal{L}_d = \frac{i}{2}d\bar{\psi}i\sigma_{\mu\nu}\gamma_5\psi F^{\mu\nu} \xrightarrow{non-rel} d\mathbf{E}\cdot\frac{\mathbf{S}}{S} \tag{8.5}$$

In equations 8.4 and 8.5, the non-relativistic limit of the more general Lorentz invariant interaction are also given. Only the space component of the 4-vectors are necessary for expressing the non-relativistic quantum mechanics interaction. In table 8.2, we give the

transformation properties of a number of dynamical variables under P and T. In particular, we note that:

$$\begin{aligned} P^\dagger \; d\mathbf{E} \cdot \frac{\mathbf{S}}{S} \; P &= -d\mathbf{E} \cdot \frac{\mathbf{S}}{S} \\ T^\dagger \; d\mathbf{E} \cdot \frac{\mathbf{S}}{S} \; T &= -d\mathbf{E} \cdot \frac{\mathbf{S}}{S} \end{aligned} \tag{8.6}$$

This implies that though $\mathcal{L}_d$ is Lorentz invariant, it is a psuedo-scalar and odd under P and T. Therefore, if parity and time-reversal are good symmetries, then the electric dipole moment $\mathbf{d}$ must vanish.

In general, we note that it is possible to write down a term in $\mathcal{L}$ which is Lorentz invariant, but yet violates C, P, or T individually. However, any quantum field theory which is unitary (i.e., has a Hermitian Hamiltonian for its time-evolution generator), local (i.e., the Lagrangian contains only derivatives up to a finite order), and Lorentz-invariant, must have CPT as a symmetry. This is known as the CPT theorem [143, 151].

In the brief discussion above, we outlined the argument for why an electron is forbidden from having a permanent EDM. This reasoning applies to any non-degenerate quantum mechanical eigenstate which has spin such as neutron, proton, atoms, molecule etc. All permanent EDMs are forbidden if T and P are both conserved.

The connection between the existence of an EDM and the conservation of parity was appreciated by Purcell and Ramsey in 1950 [135]. They initiated a search for the permanent EDM of the neutron. This experiment triggered the beginning of a series of permanent EDM searches which continue till date.

Table 8.2: Transformation of some common dynamic variables under P, and T

	parity	time-reversal
$\mathbf{r}$	$\mathbf{r} \to -\mathbf{r}$	$\mathbf{r} \to \mathbf{r}$
$\mathbf{p}$	$\mathbf{p} \to -\mathbf{p}$	$\mathbf{p} \to -\mathbf{p}$
$\mathbf{J} = \mathbf{r} \times \mathbf{p}$	$\mathbf{J} \to \mathbf{J}$	$\mathbf{J} \to -\mathbf{J}$
$\mathbf{E}$	$\mathbf{E} \to -\mathbf{E}$	$\mathbf{E} \to \mathbf{E}$
$\mathbf{B}$	$\mathbf{B} \to \mathbf{B}$	$\mathbf{B} \to -\mathbf{B}$

8.2 Experimental Demonstration of Symmetry Violation

8.2.1 P-violation

The discrete symmetries C, P and T were, until the late 1950s believed to all be good symmetries. In constructing Lagrangians to describe the interactions of nature therefore, terms that violated P, C or T were necessarily excluded. Questions as to the conservation of parity were raised by C. N. Yang and T. D. Lee, as they sought to explain the so-called $\theta - \tau$ puzzle. This is well reviewed in [151]. C. S. Wu and collaborators, following the suggestion by Yang and Lee [101], tested for the violation of parity in the beta decay of spin-polarized cobalt-60 [171]. Their experiment involved measuring the angular distribution of the emitted electrons in the beta decay. They observed a distribution which depended on the pseudo-scalar $\langle \mathbf{I} \rangle \cdot \mathbf{p}$, where $\mathbf{I}$ is the direction of the nuclear polarization and $\mathbf{p}$ is the momentum of the emitted electrons. This was a clear signature for parity violation, as it indicated that the rate of emitted electrons in the direction of the nuclear polarization differed (was less), than the rate of emission in the direction opposite the direction of nuclear polarization. The notion of left/right was therefore not merely conventional. The decay process clearly had a preferred handedness as it were. A detailed review of the experiment is provided in [151].

The observation of parity violation in beta decay was shortly followed by observations of parity violations in other weak interaction processes. In order to reflect this, the theory of the

weak interaction was reformulated in terms of left handed current-current interaction with the currents having a vector minus axial vector character.[3] The weak interaction therefore acts on left handed particles and right handed anti-particles

Beta decay, described above is mediated by the charged weak currents given by the W-bosons $W^{\pm}$. As a result of their work on the unification of the electromagnetic and weak interactions, Glashow, Salam and Weinberg predicted the existence of a neutral Z boson, and therefore a neutral weak current. It turns out that processes mediated by the weak neutral current can interfere with processes mediated by the photons which are also neutral. With the detection of the neutral weak current, it was therefore realized that parity violation effects might be detectable in atoms [30]. Atomic parity violation has been seen in a variety of systems, and provides values of the weak mixing angle at low momentum transfer. Reviews of atomic parity violation can be found at [30]. We note in passing that the atomic parity violation observed arises from interactions which are odd under parity but even under time reversal symmetry. Hence, they do not lead to permanent electric dipole moments.

8.2.2 CP-violation

The observations of parity-violation as outlined above were accompanied by the violation of charge-conjugation as well—implying that the combined operation CP was conserved. This meant that all of the weak interaction processes observed involved a transition from an initial state with a given CP eigenvalue to a final state with the same CP eigenvalue.

In 1964, Christenson, Cronin, Fitch and Turlay [39] observed a CP violating process in the decay of the neutral K mesons. Two species of neutral K mesons were known to exist $|K_1\rangle$ and $|K_2\rangle$ with CP eigenvalues of -1 and +1 respectively. Neutral kaons have a 2-pion decay mode ($\pi^{\circ}\pi^{\circ}$ and $\pi^{+}\pi^{-}$) with associated CP eigenvalue +1, and a 3-pion decay mode

3. In saying the current is left handed, we are referring to the chirality of the current given by the projector $P_{R,L} = \frac{1}{2}(1 \pm \gamma_5)$

($\pi^\circ\pi^\circ\pi^\circ$ and $\pi^+\pi^-\pi^\circ$) with CP eigenvalue -1. (Recall that the π has an intrinsic parity of -1). If CP is always conserved, then $|K_1\rangle$ must only decay via the 2-pion decay mode, and similarly $|K_2\rangle$ must only decay via the 3-pion decay mode. The 3-pion decay mode has a lower Q value than the 2-pion decay mode. Hence, there is less phase space available for the 3-pion decay, which implies that the $|K_2\rangle$ is expected to have a longer lifetime [151]. Indeed two species of neutral kaons were observed, with the short lived kaon having a lifetime of $8.95 \times 10^{-11}s$, and the long lived kaon having a lifetime of $5.1 \times 10^{-8}s$.

Christenson, *et al.* [39] discovered that, in violation of CP symmetry, K_2 decayed to 3-pions. Their conclusion then was that the CP eigenstates $|K_1\rangle$ and $|K_2\rangle$ were not the weak interaction eigenstates. Rather, the weak interaction eigenstates are the linear combinations

$$\begin{aligned} |K_S\rangle &= \frac{1}{\sqrt{1+|\epsilon|}}\left(|K_1\rangle + \epsilon\,|K_2\rangle\right) \\ |K_L\rangle &= \frac{1}{\sqrt{1+|\epsilon|}}\left(|K_2\rangle + \epsilon\,|K_1\rangle\right) \end{aligned} \tag{8.7}$$

where $|K_S\rangle$ and $|K_L\rangle$ refer to the short-lived and long lived neutral Kaons respectively. The fact that $\epsilon \sim 10^{-3}$ is finite indicates CP violation in the weak interaction.

What we have described above is flavor changing CP violation. It is explained in the Cabibo-Kobayashi-Maskawa model as being due to the fact that the mass eigenstates are different from the weak interaction eigenstates. The CKM matrix defines the mixing angles, and has a single complex phase. The single CP violating phase in the CKM model accurately predicts the observed CP violation in the B sector as well as in the K sector. Reviews of flavor violating CP violation can be found at [26, 151, 24]

An open question in physics is whether or not the flavor violating CP violation in the weak interaction as accounted for by the CKM model is the only source of CP violation. This question is connected to the so called 'Strong CP problem' as well as to the observed matter-anti matter asymmetry in the universe. The Strong CP problem refers to the presence of a

CP violating term in the QCD Lagrangian

$$\mathcal{L}_{QCD} = \mathcal{L}_0 + \theta_{QCD} G^{\mu\nu} \tilde{G_{\mu\nu}} \tag{8.8}$$

where $G^a_{\mu\nu}$ are the field strength tensors of the gluon fields. $\mathcal{L}_0$ is the part of the Lagrangian which is even under P and T. However, the additional term—parametrized by the angle θ_{QCD} is odd under T and P. [4] If $\theta_{QCD} \neq 0$, then we would observe CP violation in the strong sector. The observation is that θ_{QCD} is vanishingly small. There is no satisfactory reason why that is so. A plausible idea that would explain the apparently zero value of θ_{QCD} posits the existence of an additional symmetry which predicts the existence of axions. To date, no axions have been detected [151].

A. Sakharov, in 1967, considered the question of the relative abundance of matter and anti-matter in the universe. There is a clear abundance of matter over anti-matter. This can be quantified in terms of the baryon number of the universe ($B > 0$). Recall, that the baryon number for anti-matter is < 0. How such an asymmetry could arise from a Big bang initial condition B = 0 is presently not well understood. Sakharov's proposal was that such an asymmetry could be generated if the following necessary though not sufficient conditions were satisfied:

(i.) At least one Baryon number violating process

(ii.) interactions outside of thermal equilibrium

(iii.) C and CP violating processes

The CP violation observed in the weak sector, as described by the CKM model is insuf-

4. θ_{QCD} is an angle that the quark fields are rotated by under a gauge transformation. In principle, such a term also exists in QED. It is however a total derivative and has no physically observable consequences in QED because QED is an Abelian theory. The fact that QCD is non-Abelian means that among other things, this term has physically observable consequences [123]

ficient to generate the observed baryonic asymmetry. There is reason to believe therefore that there is more to the CP violation in physics than is included in the standard model.

8.2.3 EDMs as probes of physics beyond the standard model

We have described how P, C, and CP are violated in the weak interaction. What this means is that the standard model (SM), within the context of the CKM model allows for non - zero EDMs. However, it turns out that the SM predictions for EDMs are extremely small. In particular, the SM value for the electron EDM due to the complex phase in the CKM matrix arises as 4th order electroweak contributions [85], and is on the order of 10^{-38} ecm. Similarly, the standard model value for the neutron EDM is $\sim 10^{-32}$ ecm [40]. Similarly, the EDMs of other species are likewise suppressed in the SM.

Because the standard model CP violation leads to EDM values which are so small, then any EDM which is detected at present levels of experimental sensitivity is evidence for physics beyond the standard model. In other words, EDMs are effectively background free signals of new physics. This is a very attractive feature for an experiment. There are a variety of EDM search experiments looking for P and T violation in different sectors. They share many common features, and so we describe the idea behind the generic EDM experiment in a neutral atom. We next describe the nature of typical experiments designed to detect EDMs.

8.3 General idea of a permanent EDM experiment

Consider an atom in a state with total angular momentum $\mathbf{F} = 1/2$, and an electric dipole moment $\mathbf{d}$. The goal of a permanent EDM experiment is determine the magnitude of $\mathbf{d}$. Because of the non-zero angular momentum of the state, the atom would have a magnetic dipole moment $\boldsymbol{\mu}$ which would couple linearly to the magnetic field as would an EDM to an

electric field. In the presence of a non-zero magnetic field $\mathbf{B}$, the degeneracy between the magnetic sub-levels is lifted. The states with $m_F = 1/2$ and $m_F = 1/2$ defined with respect with the $z-$axis given by $\mathbf{B}$ are designated as $|+\rangle$ and $|-\rangle$ respectively. If an electric field $\mathbf{E}$ is applied in addition to $\mathbf{B}$, any coupling between $\mathbf{d}$ and $\mathbf{E}$ would look like an addition to the usual linear Zeeman effect. The levels will be perturbed as shown in figure 8.1. This is because $\mathbf{d}$ must be aligned with the angular momentum $\mathbf{F}$ as required by the Wigner-Eckhart theorem. A small non-zero EDM will therefore lead to a correspondingly small energy difference, which an EDM experiment is designed to detect.

One strategy of increasing the sensitivity of an EDM experiment is to move the signal away from DC, and to convert the signal to a frequency measurement as frequencies can be very precisely measured. In order do so, the atom is spin polarized transverse to the magnetic field by optical pumping using circularly polarized light as shown in figure 8.1. Angular momentum from the circularly polarized light is transferred to the atom. The atom can then said to be polarized in the x-direction—the direction of the k-vector of the light. Transverse optical pumping is equivalent to creating a coherent superposition of the two magnetic sub-levels such that the wavefunction of the atom can be represented as

$$\psi(t) = \frac{1}{\sqrt{2}} \left(|+\rangle + \mathrm{e}^{i\omega_{\pm} t} |-\rangle \right) \tag{8.9}$$

where, depending on the relative orientation of $\mathbf{E}$ and $\mathbf{B}$, the levels are split by $2\hbar\omega_{\pm}$, with

$$\omega_{\pm} = 2\pi f_{\pm} = 2 \left(\frac{\boldsymbol{\mu} \cdot \mathbf{B}}{\hbar} \pm \frac{\mathbf{d} \cdot \mathbf{E}}{\hbar} \right). \tag{8.10}$$

Now, $\psi(t)$ is not in a stationary state of the Hamiltonian. The probability of being in either of the two magnetic sub-levels will oscillate with a frequency given by the Larmor frequency. This can be pictured in the language of a dipole precessing in a magnetic field.

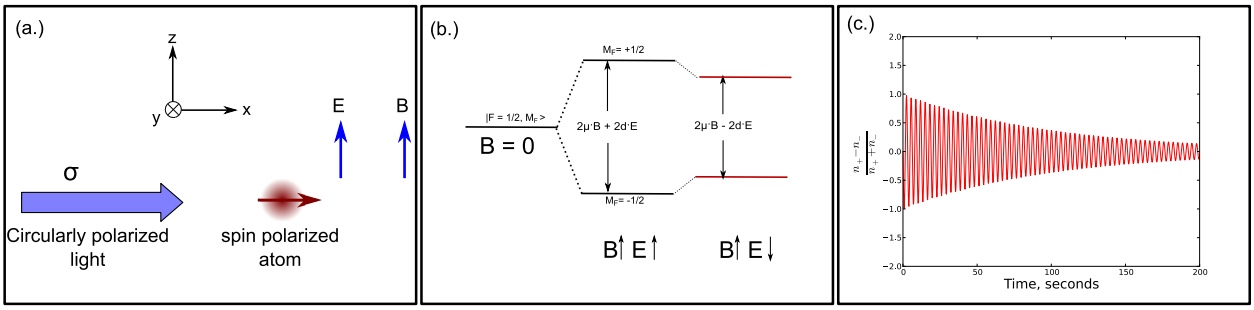

Figure 8.1: Measuring an EDM. In the panel (a.), we depict the transverse optical pumping of the atom using circularly polarized light. The atoms will be polarized in the X direction. Both the magnetic and electric fields will be in the z direction. (b.), Displacement of the magnetic sub levels in the presence of electric and magnetic fields. In panel (c), we show a cartoon of the expected signal, which is a measure of the polarization $(n_+ - n_-)/(n_+ + n_-)$, where $n_\pm$ is the population in the $M_F = \pm 1$ levels. The polarization precesses at the Larmor frequency. The envelope of the precession is given by the coherence time.

In this coordinate system, we can talk about $\langle\psi|\,\boldsymbol{\mu_x}\,|\psi\rangle$ precessing in the magnetic field. All references to precession henceforth is of this expectation value. A non-zero $\mathbf{d}$, is therefore detectable as a shift in the Larmor frequency, Δf which is correlated with the relative orientation of $\mathbf{E}$ and $\mathbf{B}$.

$$|f_+ - f_-| = 4\mathbf{d}\cdot\mathbf{E}/h \tag{8.11}$$

The fundamental limit of the precision with which we can determine this frequency difference is given by the shot noise due to the discreteness of the atoms and photons that make up the signal. For a sample of N atoms precessing in a magnetic field with frequency f, coherence time τ and a total integration time T, the shot noise limit of the frequency determination is

$$\delta f = \frac{1}{2\pi\sqrt{N\tau T}}. \tag{8.12}$$

The statistical figure of merit of EDM experiments is then given by the precision δf with which the frequency difference in equation 8.11 can be determined.

8.4 Best Limits from Permanent EDM Experiments

We have sketched out above some key steps in performing a permanent EDM experiment with a spin 1/2 atom. A large class of EDM experiments in other species are variations on this theme. In effect, a coherent superposition of two spin states is prepared in the presence of a magnetic field transverse to the polarization. As a result, this superposition acquires a phase with time which is proportional to the magnetic field, as well as with the electric field. A non-zero EDM leads to a correlation of the precession frequency with the direction of the electric field. The experimental challenge is then to measure the Larmor precession frequency as precisely as possible. In addition, systematic effects which are correlated with the E field define the systematic uncertainty that can be achieved in determining f. We briefly review some EDM searches in different sectors—highlighting their limitations and indicating their primary sensitivities.

8.4.1 Neutron EDM Experiments

The neutron EDM is the oldest in this family of searches and was initiated shortly after Ramsey and Purcell's suggestion of the neutron EDM as a test of partity non-conservation [95]. Their sensitivity then was on the order of $|d_n| < 10^{-20}e$ cm. Since then, the limit has been reduced by up to 6 orders of magnitude. The current limit is $|d_n| < 2.9 \times 10^{-26}e\ cm$ The present experiments and the next generation neutron EDM experiments rely on Ultra Cold Neutrons. There are parallel efforts with large collaborations in Europe at the ILL [15], and at the Paul Scherer Institute [7], and a U. S. collaboration which is based at the Spallation Neutron Source at Oak Ridge [90]. The advantage of using UCN is that because the velocities of the neutrons are substantially reduced, systematic effects due to motional magnetic fields due to the neutrons moving in an electric field are reduced. The aim of the next generation experiments is to improve the current limits by two orders of magnitude [40].

Neutron EDM searches are especially sensitive to CP violation of hadronic orgin, for example θ_{QCD}, the EDM of quarks, chromo EDMS etc. The different contributions are nicely treated in [130]. An appeal of neutron EDM experiments is that the neutron is a relative clean system. Unlike searches in atoms and molecules, there is no atomic or molecular structure that must be folded in in interpreting the result.

8.4.2 Paramagnetic Atom EDM Experiments

Atomic EDM experiments with species possessing an unpaired electron, are predominantly sensitive to the EDM of the electron. Such atoms are said to be paramagnetic, and EDM experiments have been performed in a number of paramagnetic species ranging from Cesium, metastable xenon and thallium [40].

The best limit to date of the electron EDM experiment using a paramagnetic atom is derived from a molecular beam experiment using Thallium atoms [138]. Regan et. al. report a result $|d_e| < 1.6 \times 10^{-27} e$ cm. Their experiment made use of multiple atomic beams to keep systematic errors under control, and to serve as a co magnetometer. There is also an ongoing effort to perform an electron EDM search using optically trapped Cesium [64].

There is a lot of activity in developing the next generation electron EDM experiments. In particular, polar molecules having an unpaired electron have been recognized as attractive systems. This is because polar molecules can be fully polarized with modest electric fields, and when polarized, the unpaired electron will be subject to the internal electric field of the molecule. This is advantageous because the the internal electric fields can be substantially larger than can be applied in the lab [40, 163]. In fact, the recent result of the electron EDM reported by Hudson et al. [87], currently sets the best limit of the EDM of the electron.

8.4.3 Diamagnetic Atom EDM Experiments

Diamagnetic atoms are those atoms which have all electrons paired. A diamagnetic atom can acquire an EDM from a variety of different sources. One important source is the so called nuclear Schiff moment S. It is a T and P odd moment of the nuclear charge distribution which couples with an applied external electric field. We will define it more precisely in 9.1.1. Diamagnetic atoms are also sensitive to the EDM of the electron were it to have one. This sensitivity is indirect—due to the closed electron shell structure of diamagnetic atoms. However, as a result of the hyperfine interaction, there is a sensitivity nonetheless and this is parametrized by the constant η_e. This is treated in more detail in [95]. In general, one can write the atomic EDM as

$$d_A = k_s S + \eta_e d_e + (k_T C_T + k_S C_S + k_P C_P) \tag{8.13}$$

where C_T, C_S, and C_P refer to the CP-violating tensor, scalar and pseudo-scalar couplings of the electron to the current density of the nucleus [40], and the k coefficients represent the strength of the different couplings, and depend on the details of the fundamental CP violating interaction.

Experiments using ^{129}Xe and ^{199}Hg have over the years yielded the lowest limits. Currently, the best limit is set by the ^{199}Hg experiment at the University of Washington [74]. The atoms are held in vapor cells, and can be readily spin polarized.

8.4.4 Summary of limits

We list in table 8.3 some of the best experimental limits for CP violation derived from EDM searches in different sectors. As given in the table, different experimental systems studied to date are sensitive primarily CP violation from different sectors. To date, no evidence

for CP violationnot accounted for in the SM model has been detected. These systems are therefore yield complementary information. In addition, theoretical effort in the form of nuclear, atomic and molecular structure is required in order to interpret experimental limits in terms of the fundamental CP vilolation.

Table 8.3: Limits of permanent EDMs in different sectors

System	Primary sensitivity	d (e-cm)	References
^{205}Tl	d_e, C_S	$(-4.0 \pm 4.3) \times 10^{-25}$	[138]
Neutron	θ_{QCD},quark-EDMs	$(0.2 \pm 1.7) \times 10^{-26}$	[16]
^{199}Hg	$\theta_{QCD}, g_{\pi NN}, C_T$	$(0.49 \pm 1.50) \times 10^{-29}$	[74]

CHAPTER 9

EDM SEARCH IN RADIUM-225

9.1 Enhanced Sensitivity to T and P odd interactions in radium - 225

As mentioned in chapter 8, the best EDM limit in the diamagnetic sector for CP violation in atoms is obtained from the ^{199}Hg experiment. Diamagnetic atoms are predominantly sensitive to CP violation of hadronic origin.

Haxton and Henley [80] and Sushkov *et al.* [155] articulated the idea that atoms with pronounced octupole and quadrupole deformations would have an enhanced sensitivity to T and P odd interactions of hadronic origin. More recent treatments of this enhancement can be found in [14, 62] and references therein. In order to understand the origin of this increased sensitivity, we note that atomic EDM measurements using diamagnetic atoms are sensitive to the so called nuclear "Schiff moment". These experiments involve addressing the electronic degrees of freedom of the atom optically. Any permanent EDM or T and P odd interaction in the nucleus induces an EDM on the atom. A relevant question to ask then is to what extent is the nucleus sensitive to an externally applied electric field? When the atom is placed in this field, the nucleus is shielded from it due to the rearrangement of the atomic electron cloud, such that the average force on the nucleus is zero. We know that this screening occurs, because otherwise, the positively charged nucleus would be accelerated. That also means that in this picture, any EDM in the nucleus, due to say, a neutron or proton EDM would be similarly shielded from the external electric field and would not couple to it. Schiff considered this question and arrived at the conclusion that actually an EDM in the nucleus is not completely shielded from the external field. His results are referred to as Schiff's Theorem [145]. He defines a 'Schiff moment' which is the lowest order T and P odd

moment which couples with the applied electric field that can induce an atomic EDM.

9.1.1 Schiffs Theorem

Following very closely the treatment of [62], we consider an atom in an external electric field $\mathbf{E_0}$. If the nucleus of the atom has a permanent EDM $\mathbf{d}_0$, then the Hamiltonian of the atom in the field is

$$H_{\text{atom}} = \sum_{i=1}^{Z} [K_i + V_i + e\phi(\mathbf{r}_i) - e\mathbf{E}_0 \cdot \mathbf{r}_i] - e_p \mathbf{E}_0 \cdot \mathbf{d}_0 \tag{9.1}$$

where K_i is the kinetic energy of the electrons, V_i is the electron - electron repulsive interaction, and

$$\phi(\mathbf{r_i}) = \frac{e_p}{4\pi} \int \frac{d^3x\rho(x)}{|x - r_i|} \tag{9.2}$$

is the electrostatic potential felt by each electron due to the complete nuclear charge distribution. The last two terms on the RHS of equation 9.1 encode the interaction of the induced polarization of the atom, and that of the permanent EDM of the nucleus with the external field respectively.

In order to discuss the shielding of the external field, we consider the following unitary transformation on the Hamiltonian $H_{\text{atom}} \rightarrow \overline{H}_{\text{atom}} = e^{-U} H_{\text{atom}} e^{U}$. Thus,

$$\overline{H}_{\text{atom}} \simeq H_{\text{atom}} + i[H, U] + \ldots \tag{9.3}$$

If the Unitary operator U is defined as

$$U = \frac{\mathbf{d}_0}{Z} \cdot \sum_{i=1}^{Z} p_i, \tag{9.4}$$

where $p_i = -i\hbar\nabla_i$, equation 9.3 yields

$$\overline{H}_{\text{atom}} = \sum_{i=1}^{Z} \left[K_i + V_i + e\phi(\mathbf{r}_i) - e\phi(r_i) - \frac{e_p}{Z}\mathbf{d_0} \cdot \nabla_i \phi(r_i) \right]. \tag{9.5}$$

The form of the operator U in equation 9.4 is used because

$$\begin{aligned} \left\langle \frac{i}{\hbar}[\mathbf{p}, H_{\text{atom}}] \right\rangle &= 0 \\ \Rightarrow \left\langle \frac{i}{\hbar}[U, H_{\text{atom}}] \right\rangle &= 0 \end{aligned} \tag{9.6}$$

This holds because there is no *average* force on the atom in an external field.

As a result, the difference between equation 9.5 and 9.1 must not lead to any energy shift to first order in $\mathbf{d}_0$.

$$\Delta = e_p \mathbf{d}_0 \cdot \left(\mathbf{E}_0 - \frac{1}{Z} \sum_{i=1}^{Z} \nabla_i \phi(\mathbf{r}_i) \right) = 0 \tag{9.7}$$

We now have the Hamiltonian in equation 9.5 representing a neutral atom in an external electric field. Next, we need an expression for $\phi(r)$. As noted in [62], if the nucleus is point-like, then $\rho(x) = Z\delta^3(x)$, and equation 9.7 assumes the form $\Delta = e_p \mathbf{d}_0 \cdot (\mathbf{E}_0 + \mathbf{E_e}) = 0$, where $\mathbf{E_e}$ is the electric field at the nucleus caused by the electrons.

In reality though, the nucleus has finite spatial extent, and so we expand $\rho(x)$ in a power series; bearing in mind that it has a total charge Z, a dipole moment $\mathbf{d_0}$, and a mean square charge radius $\langle r^2 \rangle$.

Keeping the monopole and dipole terms in the expansion, we get

$$\rho(\mathbf{x}) = \underbrace{\left[Z\delta^3(\mathbf{x}) + Z\frac{\langle r^2 \rangle_{ch}}{6}\nabla^2\delta^3(\mathbf{x}) \right]}_{\rho_{\text{mon}}(\mathbf{x})} - \underbrace{\left[\mathbf{d_0} \cdot \nabla\delta^3(\mathbf{x}) + \frac{\mathbf{O_0} \cdot \nabla}{10}\nabla^2\delta^3(\mathbf{x}) \right]}_{\rho_{\text{dip}}(\mathbf{x})} + \ldots \tag{9.8}$$

which is written in terms of the following moments of the charge distribution

$$\begin{aligned}
\int d^3r\ \rho(x) &= Z \\
\int d^3r\ r^2\rho(r) &= Z\left\langle r^2\right\rangle_{ch} \\
\int d^3r\ \mathbf{r}\rho(r) &= \mathbf{d}_0 \\
\int d^3r\ \mathbf{r}r^2\rho(r) &= \mathbf{O}_0.
\end{aligned} \tag{9.9}$$

$\overline{H}_{\text{atom}}$ can be separated into a part that is independent of the dipole moments $\mathbf{d}_0$ and $\mathbf{O}_0$, as well as another part which is proportional to them, and therefore odd under P and T.

$$\overline{H}_{\text{atom}} = H^{\circ}_{\text{atom}} + H^{PT}_{\text{atom}} \tag{9.10}$$

where

$$H^{\circ}_{\text{atom}} = \sum_{i=1}^{Z} K_i + V_i - e\mathbf{E_0}\cdot\mathbf{r_i} - \frac{Z\alpha}{\mathbf{r_i}} + \ldots \tag{9.11}$$

and

$$H^{PT}_{\text{atom}} = -\alpha\sum_{i=1}^{Z}\Delta h(\mathbf{r_i}) \tag{9.12}$$

with

$$\Delta h(\mathbf{r_i}) = \int \frac{d^3x\ \rho_{\text{dip}}(\mathbf{x})}{|\mathbf{x}-\mathbf{r}|} + \frac{\mathbf{d_o}\cdot\nabla}{Z}\int \frac{d^3x\ \rho_{\text{mon}}(\mathbf{x})}{|\mathbf{x}-\mathbf{r}|} \tag{9.13}$$

Substituting equation 9.8 into 9.13, we get that the T and P odd interaction with the electric field is

$$\Delta h(\mathbf{r_i}) = 4\pi\mathbf{S}\cdot\nabla\delta^3(\mathbf{r}) + \ldots \tag{9.14}$$

The Schiff moment $\mathbf{S}$ is given by

$$\begin{aligned}\mathbf{S} &= \frac{1}{10}\left[\mathbf{O_0} - \frac{5}{3}\mathbf{d_0}\left\langle r^2\right\rangle_{ch}\right] \\ &= \frac{1}{10}\int \rho(r)\left(r^2 - \frac{5}{3}\left\langle r^2\right\rangle_{ch}\right)\mathbf{r}d^3\ r\end{aligned} \tag{9.15}$$

As noted in [62], it is like a radially weighted dipole moment. Also, Engel makes a connection between the expression for the Schiff moment in equation 9.15 with that originally presented by Schiff.

9.1.2 Effect of Static Deformations

Nuclei assume shapes which minimize the energy of the ground state. In terms of the liquid drop picture, the destabilizing coulomb energy competes with the stabilizing nuclear surface tension—such that the equilibrium shape could be non-spherical.

In describing deformed nuclear shapes, it is useful to consider an intrinsic or body fixed nuclear frame. As discussed in [1, 72], the surface of an axially deformed nucleus can be parametrized in terms of the deformation parameters β as

$$R(\theta) = R_N\left(1 + \sum_{l=1}\beta_l Y_{l0}(\theta)\right) \tag{9.16}$$

In order to eliminate the center of mass displacement (i.e. keep the center of mass at r = 0), it is required that the β_1 term be set to

$$\beta_1 = -3\sqrt{\frac{3}{4\pi}}\sum_{l=2}\frac{(l+1)\beta_l\beta_{l+1}}{\sqrt{(2l+1)(2l+3)}}. \tag{9.17}$$

as prescribed in Bohr and Motelson [27]. β_2 is the quadrupole deformation parameter, β_3 the octupole deformation parameter and so on. An important property of deformed nuclei

is that they can rotate. Rotational bands are detectable in the nuclear level structure much like the rotational bands of molecules. For a reflection symmetric molecule, all the levels in a given rotational band have the same parity [1]. Likewise for nuclei. However, nulei that have a non zero octupole deformation are not reflection symmetric. As a result, it is possible to have states in the same rotational band which have opposite parity. In fact, one of the signatures for the existence of possible octupole deformation is the existence of parity doublets. That is states with the same spin but opposite parity which lie close to each other. A nice review of the theory and experimental results for octupole deformed nuclei is the review article [34].

An important question that often arises is how can a nucleus which has spin $I = 0$, or $I = 1/2$ still have a non-zero octupole deformation? We are familiar with the result that nuclei with $I \leq 1$ can not have quadrupole or higher moments. The key difference is that these deformations are in the intrinsic frame of the nucleus. Isotropy of space implies that there is no unique direction. Consequently, in the lab frame, the quadrupole, octupole, and higher moments vanish for these nuclei. We give in equation 9.18 the expression of the quadrupole moment in the intrinsic nuclear frame and the lab frame [132].

$$Q_{\text{spect}} = \frac{3I^2 - I(I+1)}{(I+1)(2I+3)} Q_{\text{int}} \tag{9.18}$$

We note from equation 9.18 that the spectroscopic Quadrupole moment vanishes for $I \leq 1$ as expected. However, this means that a nucleus with spin 0, or spin $1/2$ can still have a marked quadrupole, octupole and higher order deformations in the *intrinsic* frame.

There are two effects which lead to the enhancement of the Schiff moment in the lab frame for an octupole deformed nucleus over a spherical nucleus. Firstly, following the treatment of Ginges and Flambaum [72], we can relate the Schiff moment in the lab frame to the Schiff

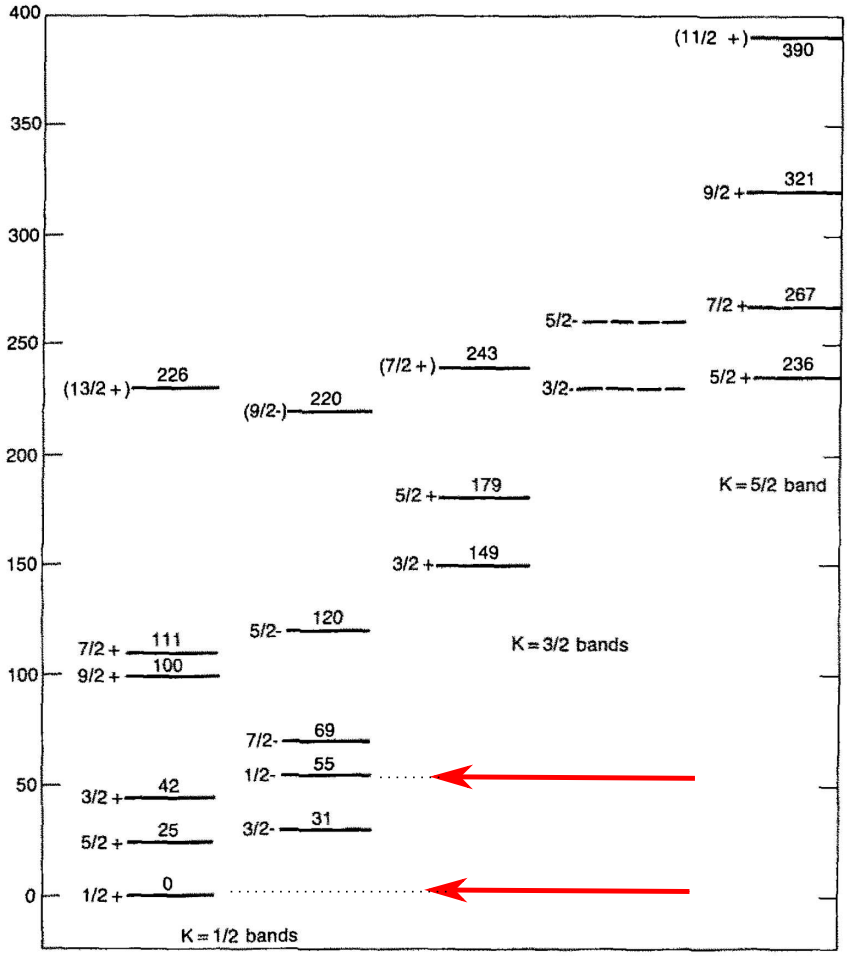

Figure 9.1: Nuclear Levels of ^{225}Ra. Adapted from [81]. This gives the proposed grouping of the low-lying states of ^{225}Ra into rotational bands. The presence of levels with opposite parity in the same rotational band is indicative of the breaking of reflection symmetry, such as would arise in the case of octupole deformation. We indicate with the red arrows the ground state and its parity doublet approximately 55 kEV away.

moment in the intrinsic nuclear frame as,

$$\mathbf{S}_z = \mathbf{S}_{\text{intr}} \frac{2KM}{I(I+1)} \frac{\langle \psi_- | \mathbf{W} | \psi_+ \rangle}{E_+ - E_-} \tag{9.19}$$

where $\mathbf{W}$ is some T and P odd interaction. What this expression illustrates is that for a nuclear ground state with a definite parity, the Schiff moment in the lab frame is enhanced,

by a factor proportional to the admixture of a nearby state of opposite parity which is mixed in by the T and P odd interaction. This interaction could be some exotic interaction that is not described by the standard model. Recall that we said that octupole deformed nuclei exhibit parity doubling of their nuclear states. Because of this, the energy denominator can be small—leading to an enhancement of the Schiff moment in the lab frame.

Secondly, as given in [61], for ^{225}Ra, the ground state ($J^\pi = \frac{1}{2}^-$)and the nearby excited state of opposite parity ($J^\pi = \frac{1}{2}^+$) are 55 keV apart. They are furthermore understood to be projections onto good parity and angular momentum of the same "intrinsic state" [47]. As a result, the intrinsic state expectation value $\langle S_z \rangle_{\text{intr}}$ is larger than in a spherical nucleus. In particular,

$$S_{\text{intr}} = eZR_N^3 \frac{3}{20\pi} \sum_{l=2} \frac{(l+1)\beta_l \beta_{l+1}}{\sqrt{(2l+1)(2l+3)}} \approx eZR_n^3 \frac{9\beta_2\beta_3}{20\pi\sqrt{35}}. \tag{9.20}$$

Thus we note that the collective intrinsic Schiff moment is magnified for nuclei with static quadrupole and octupole deformations. Similarly octupole deformed nuclei that have been considered for EDM searches are ^{223}Rn, ^{223}Ra, ^{223}Fr [40].

We have described above some signatures of nuclear deformation—namely the presence of rotational bands and of parity doublets. Other signatures allow for the precise determination of the deformation parameters. For example, as treated in [1], a nucleus with a pronounced octupole deformation is expected to have enhanced E1 and E3 transition rates. For example, the matrix elements of the E3 transitions from the ground state, as given by B(E3) [1] can be related to β_3.

$$B(E3) = \frac{3}{4\pi}(zeR^3)^2\beta_3^2 \tag{9.21}$$

where R is the RMS radius of the nucleus. A compilation of the derived and measured

1. For an electric or magnetic multipole transition described by the operator $\mathbf{O}_\lambda$,

$$B(\lambda; J_i\zeta \to J_f\xi) = \frac{1}{2J_i+1} \left|\langle J_f\xi\zeta \,||\, \mathbf{O}_\lambda \,||\, J_i\rangle\right|^2$$

deformation parameters for a number of nuclei is given in [96]

We note here that the ^{225}Ra has deformation parameters $\beta_2 = 0.138, \beta_3 = 0.104$, while ^{199}Hg is nearly spherical, with $\beta_2 = -0.122, \beta_3 = 0$. The intrinsic shapes of the two nuclei are given in figure 9.2.

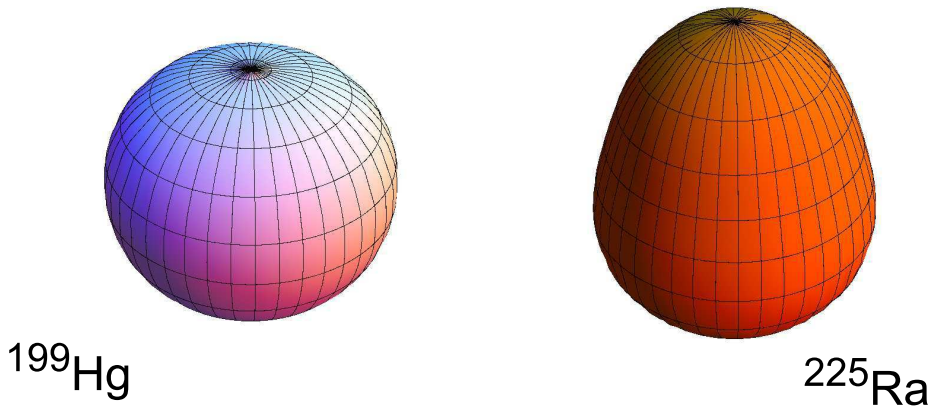

Figure 9.2: Shape of the nucleus of ^{199}Hg and ^{225}Ra, as given in equation 9.16. We use the deformation parameters from [110].

The contributions to the Schiff moment can also be expressed as a sum of terms with different isospin as in equation 9.22

$$S = g_{\pi NN}\left(a_0\bar{g}^0 + a_1\bar{g}^1 + a_2\bar{g}^2\right) \tag{9.22}$$

$g_{\pi NN}$ is the strong π nucleon-nucleon couping constant, and $\bar{g}^i$ are the isoscalar, isovector and isotensor contributions to the CP violating $g_{\pi NN}$. For example, θ_{QCD} is related to the isoscalar coupling $\bar{g}^0 \approx 0.027\theta_{QCD}$, quark EDMs contribute to the isovector coupling etc [40].

There have been a variety of calculations for the Schiff moment for ^{199}Hg and ^{225}Ra [61, 13, 152] with varying levels of sophistication. Qualitatively, there is an expectation

for an enhancement, for the reasons outlined above. The magnitude of the enhancement depends on the nature of the CP violating nucleon-nucleon interaction. That is whether the coupling is scalar, pseudo scalar etc. In [92] and [47], Jon Engel and collaborators calculated the Schiff moments of ^{225}Ra and ^{199}Hg using the SkO Skyrme model.

$$\begin{aligned} S_{^{199}Hg} &= g_{\pi NN}\left(0.01\ \bar{g}^0_{CP} + 0.074\ \bar{g}^1_{CP} + 0.018\ \bar{g}^2_{CP}\right) \\ S_{^{225}Ra} &= g_{\pi NN}\left(-1.5\ \bar{g}^0_{CP} + 6.0\ \bar{g}^1_{CP} - 4.0\ \bar{g}^2_{CP}\right) \end{aligned} \tag{9.23}$$

They note that the uncertainty of the coefficients of the CP violating couplings could be up to a factor of two. However it is clear that were any of the CP violating πNN to be non-zero, the ^{225}Ra Schiff moment would be larger than the ^{199}Hg Schiff moment by factors of up to a couple hundred.

9.2 Search for permanent EDM in ultracold radium atoms

As described in section 9.1, ^{225}Ra has an enhanced sensitivity to CP-odd interactions and is an attractive system to search for an EDM in. Technically however, it differs from ^{199}Hg in two fundamental ways which make an experiment of the style of the ^{199}Hg - EDM reported in [74] untenable. Firstly, it has a very low vapor pressure and an experiment can therefore not be performed in a vapor cell. Secondly, it is radioactive with a lifetime of 14.9 days. as a result, the number of atoms available to work with is substantially less, and would decay away over the course of a couple of weeks.

Our scheme is to load radium atoms into a one dimensional optical lattice which is located in a region of strong electric field **E** as well as a uniform and stable magnetic field. There the atoms will be spin polarized transverse to the magnetic fields and allowed to precess for some time as described in section 8.3. An EDM signature will be determined by looking for a correlation in the frequency with the direction of the electric field.

We use a magneto-optical trap (MOT) to accumulate atoms from an effusive source of radium atoms. In a MOT, the atoms will be cold and dense enough to be efficiently loaded into an optical dipole trap (ODT). The ODT is used as a shuttle to move the atoms away from the region of the MOT to a magnetically shielded region—the science chamber. There, the atoms will be handed off to a one-dimensional optical lattice (formed by a standing wave) which is located between a pair of field plates. It is then that the atoms will be spin polarized transverse to the **E** and **B** fields and allowed to precess for some time T.

Using an optical lattice to perform and EDM experiment was first discussed by [140]. For the electron EDM, Chin *et al.* [38] also carried out a thorough study of the possibility of using Cs in an optical lattice for an electron EDM experiment–quantifying the expected levels for systematic effects. By trapping the atoms, we can obtain large interrogation times–enabling high precision frequency determination. As we will discuss below, the systematic

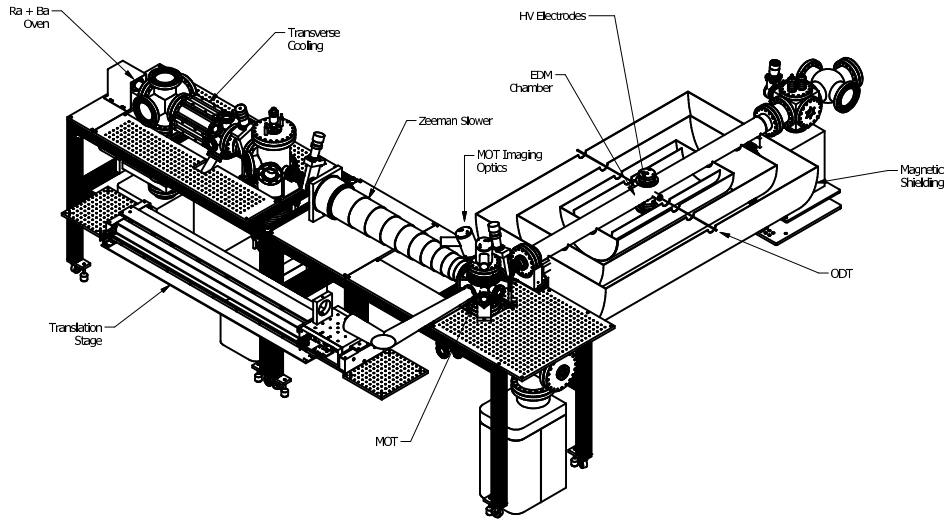

Figure 9.3: Schematic of experimental layout of Radium-EDM experiment. A radium atomic beam is created by an effusive oven source. Atoms are slowed down with zeeman slower and accumulated with MOT. They are then transferred into an ODT formed with a lens on a long translation stage. As the stage is translated, the atoms will be moved into the science region which is enclosed in a magnetically shielded region. The top half of the cylindrical shields have been cut away to show the interior details.

effects due to trapping the atoms in an optical lattice should be sufficiently small in order to make a competitive experiment using this scheme feasible.

9.3 Sensitivity Estimates

In an EDM experiment, the total sensitivity to the underlying CP violating physics is determined by (1.) The relative enhancement of time and parity odd moments in the atom, (2.) the total statistical error achieved, and (3.) the total systematic errors. The sensitivity to the T and P odd interactions is given by the choice of atom, and as we described in chapter 9.1, ^{225}Ra has an enhancement factor between 2 and 3 orders of magnitude larger than ^{199}Hg. The limit of the ^{199}Hg experiment is $|d_{^{199}Hg}| < 0.49 \times 10^{-29} e$ cm [74]. Assuming an enhancement factor of 100, this means that a measurement on the order of $10^{-27} e$ cm would be sensitive to T and P odd interactions on the same scale as the ^{199}Hg experiment.

Statistical errors can be minimized by integrating for a long time, and by using more atoms. The noise floor is given by the atom shot noise limit. Systematic errors can be minimized by good experimental design, such that possible sources of systematic errors are eliminated or monitored with sufficient accuracy such that appropriate corrections can be made.

9.3.1 Magnetic field stability considerations

In order to achieve the shot noise limited frequency determination given in equation 8.12, we define the frequency stability *per shot* as

$$\xi = \frac{1}{2\pi\sqrt{N\varepsilon\tau}} \tag{9.24}$$

This means that in order to have a shot noise limited frequency error, within a time interval τ the magnetic field must be stable to the level δB where $\mu_N \delta B = h\xi\sqrt{\tau}$. For $N = 10^4$ atoms, with a coherence time $\tau = 100s$, and $\varepsilon = 0.5$, the efficiency with which we can detect the N atoms contributing to the signal, we have $\xi = 225\ \mu Hz/\sqrt{Hz}$, and we require a temporal magnetic field stability of $\delta B < 2.9 \times 10^{-6}$ Gauss in 100 s.

9.3.2 Statistical Errors

Consider the case where for a time $T/2$, we measure f_-, and for an equal amount of time, we measure f_+. An EDM $\mathbf{d}$ would correspond to a frequency shift $f_+ - f_-$, with

$$\begin{aligned} |\mathbf{d}| &= \frac{h}{4E}\,|f_+ - f_-| \\ \delta\mathbf{d} &= \frac{h}{4E}\delta f \end{aligned} \tag{9.25}$$

From equations 8.12 and 8.11, the shot noise limited sensitivity to an EDM $\delta\mathbf{d}$ is then given by

$$\delta \mathbf{d} = \frac{\hbar}{2E\sqrt{N\varepsilon T\tau}} \tag{9.26}$$

The near term goals for our experiment, using readily achievable experimental conditions are given in table 9.1.

Table 9.1: Goals for experimental parameters, and projected sensitivity

Atoms in holding ODT	N	1×10^4
Electric Field	E	100 kV/cm
Total Integration time	T	10 days
Spin Coherence Time	τ	100 seconds
Detection Efficiency	ε	0.5
Frequency difference	δf	0.3 μHz
Limit on $\mathbf{d}$	$\delta \mathbf{d}$	$< 1 \times 10^{-26}$ e cm

9.3.3 Anticipated Systematic Errors and Trap Effects

Systematic errors refer to those effects which if present would mimic a real EDM signal. They share the common feature that they are correlated with the sign of the electric field. Two such effects which are particularly important for all EDM experiments are

(1.) **The motional magnetic fields:** When an atom moves in a non-zero electric field, it experiences a magnetic field in its rest frame given by $\mathbf{B}_m = \mathbf{v}/c \times \mathbf{E}$. Now, if there is an additional externally applied magnetic field B_0 in the lab frame, and if this field forms a small angle θ_{EB} with the applied electric field, then the total magnetic field felt by atoms is

$$\mathbf{B} = \mathbf{B}_0 + \theta_{EB}\mathbf{B}_m + \frac{1}{2}\frac{\mathbf{B}_m}{\mathbf{B}_0} \tag{9.27}$$

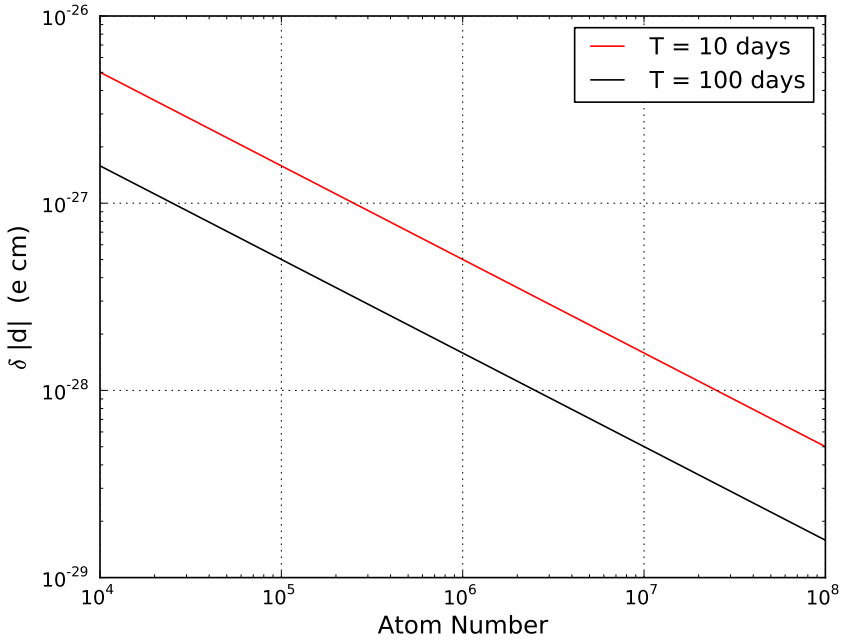

Figure 9.4: Shot noise limited sensitivity as a function of atom number for measurements lasting 10 days and 100 days. We plot out equation 9.26, using the values given in Table 9.1 for the electric field E, detection efficiency ε, and the coherence time τ

We note from equation 9.27 that we can have a systematic error associated with $\mathbf{B}_m$ if $\theta_{EB} \neq 0$. In this case, the total magnetic field at the atoms is directly correlated with the electric field, and would mimic a real EDM. If $\theta_{EB} \neq 0$ however, we a systematic error can still arise if the field reversal is not exact. This arises because the third term on the RHS of equation 9.27 would lead to a magnetic field whose magnitude is correlated with the sign of the electric field [156]. Our sensitivity to motional magnetic fields is grossly reduced in comparison to experiments in atomic beams [138]. The average velocity of the atoms in the volume of the optical lattice is 0. To first order, the contribution to the motional magnetic fields is therefore vanishing. This is also the case with the ^{199}Hg experiment which is performed in a closed vapor cell. Their error budget due to motional magnetic field is on the order of $1.8 \times^1 0{-}31e$ cm [74]. We expect to be less

sensitive to motional magnetic fields than the Hg experiment since our RMS velocities, and effective volume of the cells are significantly smaller. Therefore, in order to achieve a statistical limit given in table 9.1, we do not expect the motional magnetic fields to be a limitation.

(2.) **Leakage currents** When a high voltage is applied between electrodes in order to generate a strong electric field, there is a chance that currents would flow between the field plates if there is a path for the current to go. This leads to a systematic error as there is a magnetic field associated with the leakage current, and the sign of the induced magnetic field is correlated with the sign of the electric field. This was particularly troublesome for the ^{199}Hg experiment which was performed in a vapor cell. Leakage currents were responsible for the largest item in their error budget–$4.53 \times 10^{-30} e$ cm . Because our field plates are in vacuum, there is no direct path for current to flow near the atoms contributing to the signal. Furthermore, in vacuum, we are able to apply larger electric fields without dielectric breakdown. Making very conservative assumptions about the current path, we believe that we can apply fields up to 100 kV/cm, and achieve the sensitivity outlined in table 9.1 without being limited by the leakage currents

(3.) **Drifting Magnetic Fields** The local magnetic field sampled by the radium atoms contributing to the EDM signal must be well controlled in order to achieve the shot noise limited uncertainty. We therefore need local magnetometry to monitor the magnetic fields in order to make appropriate corrections.

(4.) **Vector Stark Shift due to Trapping Light** In [140], the authors discussed the impact of a vector stark shift on the performance of an optical lattice in serving as a trap for atoms in an EDM experiment. It turns out that if the trapping light has some residual circular polarization, there is a vector stark shift which leads to a differential shift of the magnetic sub levels $M_F = \pm 1/2$. This in effect looks like a magnetic field

$\tilde{\mathbf{B}}$, where $\tilde{\mathbf{B}} \propto (|\varepsilon_L|^2 - |\varepsilon_R|^2)\mathbf{k}$ The magnitude of the effective shift goes as

$$\Delta f = f_v(|\varepsilon_L|^2 - |\varepsilon_R|^2)m\cos\theta \tag{9.28}$$

where θ is the angle between $\mathbf{k}$, the direction of propagation of the laser forming the lattice and and the static magnetic field $\mathbf{B_0}$. Importantly though, this vector shift does not lead to a systematic effect, as it is not correlated with the sign of the electric field. It however can lead to enhanced sensitivity to the intensity noise of the trapping laser. This is because intensity noise would look like magnetic field noise. Magnetic field noise on the other hand could lead to shortened coherence times. As treated in [140], it turns out that the diamagnetic atoms are substantially less sensitive to this effect than the alkali atoms. Technically, to reduce sensitivity to this effect, we arrange the axes such that $\theta \to 0$.

(5.) **E1 M1 interference** Romalis and Fortson in [140] consider a systematic effect which might arise in an optical lattice EDM experiment. The effect arises because in the presence of a non zero electric field, atomic levels acquire small admixtures of opposite parity states. Consequently, previously forbidden transitions (based on parity selection rules) such as M1 transitions are suddenly allowed, and can interfere with the allowed E1 transition. As for the vector stark shift above, this effect was calculated to be strongly suppressed ($\sim 10^{-5}$ in mercury over the alkali cesium. Radium will also be similarly suppressed.

CHAPTER 10

LASER COOLING AND TRAPPING OF RADIUM

Radium (Z = 88) has the electronic configuration [Rn]$7s^2$ in its ground state. It is an alkaline-earth element and lies immediately below barium in the periodic table. There are 43 known isotopes of radium, four of which are naturally occurring, and none of which are stable. The four longest lived isotopes of radium are (A = 223, 224, 225, and 226).

Table 10.1: Isotopes of radium with the longest lifetimes along with their nuclear ground state spins and parities

nuclide	half-life	spin-parity
^{223}Ra	11.43 d	$\frac{3}{2}^+$
^{224}Ra	3.63 d	0^+
^{225}Ra	14.9 d	$\frac{1}{2}^+$
^{226}Ra	1600 y	0^+

Like most of the other alkaline-earth elements, radium can be laser cooled and trapped. General treatments of laser cooling and trapping can be found in textbooks [108, 65]. We will first consider some of the specific features of the atomic structure of radium that are pertinent for laser cooling.

The earliest atomic spectroscopy of radium was performed in 1934 [137]. In analyzing a radium arc spectrum, E. Rasmussen identified 13 even and 28 odd parity levels in ^{226}Ra. H. N. Russell, motivated by the desire to understand astrophysically observed lines [141], modified some of the assignment of Rasmussen by comparing general trends between the spectrum of Ra-I and the other alkaline-earth elements.

In the 1980s, with the availability of radioactive beams of radium isotopes at ISOLDE at CERN, a series of experiments were performed using collinear laser spectroscopy to determine

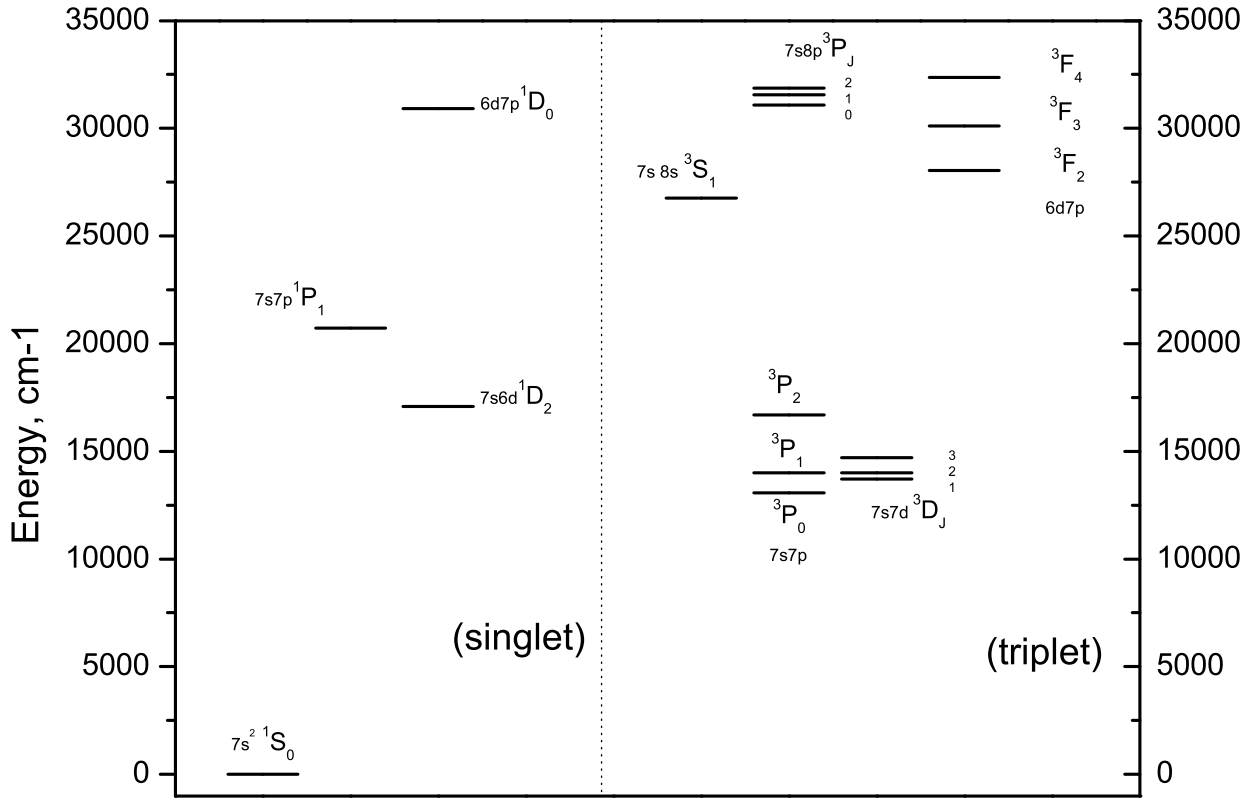

Figure 10.1: Level Scheme for ^{226}Ra, showing its low lying energy levels. For reference, the ionization energy of radium is 42573.01 cm^{-}1.

the nuclear moments of the different isotopes of radium [2, 3, 166, 116]. Currently, atomic spectroscopy of radium is driven by the promise of radium as a sensitive system for studying P and T violation, as well as for astrophysics reasons [136]. There has also been quite a bit of effort in calculating the atomic structure of radium [59, 58, 21, 22, 18]. As more experimental values of relevant observables become available, the calculations are better constrained.

Consider the level scheme for the radium atom shown in figure 10.1. Laser cooling is most efficient on a strong transition that is 'closed'. This means that when an atom is excited, it has a high probability of returning to the state from which it was excited. When such a transition is driven repeatedly, a force is applied to the atom which is proportional to the excitation rate of the transition and the momentum transfer per photon. Starting from the

$7s^2\ ^1S_0$ ground state, the strongest E1 transition is to the $7s7p^1P_1$ level at 483 nm. Another accessible E1 transition is from the ground state to the $7s7p^3P_1$ level at 714 nm. This singlet - triplet intercombination line is not fully forbidden due to relativistic effects. Both of these transitions are quasi-cycling. The branching ratios to dark states are non-negligible, and active repumping is required in order to maintain the atoms in the cooling cycle.

We compare the values of the parameters relevant for laser cooling using the 714 nm and 483 nm transitions in table 10.2. While the transition to $^1P_1$ is stronger, and would consequently be better for capturing atoms, it is less desirable for laser cooling because the atom is pumped into dark states after only about 500 cycles of the $^1S_0$ to $^1P_1$ transition. Branching ratios from the $^1P_1$ to lower lying levels are given in figure 10.2, and as can be seen from the figure, in order to close the leak channels, at least three repump lasers are required. On the other hand, ground state atoms excited using the 714 nm transition are pumped into dark states after $\sim 2.4 \times 10^4$ cycles. This can be extended to greater than 3×10^7 cycles with a single repumping laser from the $7s6d^3D_1$ to $7s7p^1P_1$ level at 1428 nm. For the laser cooling and trapping work described here, we make use of the 714 nm transition for laser cooling, along with a laser at 1428 nm to repump the atoms back into the cooling cycle.

In other alkaline-earth (and alkaline-earth like) atoms like strontium [94] and ytterbium [106], the ^3D metastable levels are higher lying than the ^3P_J levels. Consequently the $^3P_1 -^3 D_J$ leak channel is non-existent when cooling using the inter-combination transition for those atoms. Also, the $^1S_0 -^1 P_1$ line can be used with no repump, as the branching ratios from the $^1P_1$ to the ^3D_J levels is small. Barium and radium atoms however have the ^3D_J levels lower than the ^3P_J manifold along with rather large branching ratios from $^1P_1$ to ^3D_J. Barium trapping nonetheless has been realized by [45], using the strong $^1S_0 -^1 P_1$ line along with repump lasers at four different wavelengths.

Table 10.2: Atomic Properties of Radium Relevant for Laser Cooling

Parameters	${}^1S_0 - {}^1P_1$	${}^1S_0 - {}^3P_1$	Units	Description
λ	483	714	(nm)	Transition Wavelength
$k = 2\pi/\lambda$	130000	87999	(cm^{-1})	Wavenumber
τ	5.5	420	(ns)	Atomic State Lifetime
$\sigma_{ge} = 3\lambda^2/2\pi$	111	243	(10^{-15} m^2)	Absorption cross section
$\Gamma = 1/2\pi\tau$	28.8	0.38	(MHz)	Natural linewidth
$I_s = \pi hc/3\lambda^3\tau$	33.5	0.136	($\mathrm{mW/cm}^2$)	Saturation Intensity
$a_{max} = \hbar k/2M\tau$	33.0	0.29	(10^4 $\mathrm{m/s}^2$)	Maximum Acceleration
$\omega_r/2\pi = \hbar k^2/4\pi M$	3.76	1.73	(kHz)	Recoil frequency
$v_r = \hbar k/M$	0.36	0.24	(cm/s)	Recoil velocity
$V_D = \sqrt{k_B T_D/M}$	15.9	1.8	(cm/s)	Doppler Limit Velocity
$T_D = h\Gamma/2k_B$	694	9.1	(μK)	Doppler Temperature
$T_r = \hbar^2 k^2/Mk_B$	0.36	0.16	(μK)	Recoil Temperature

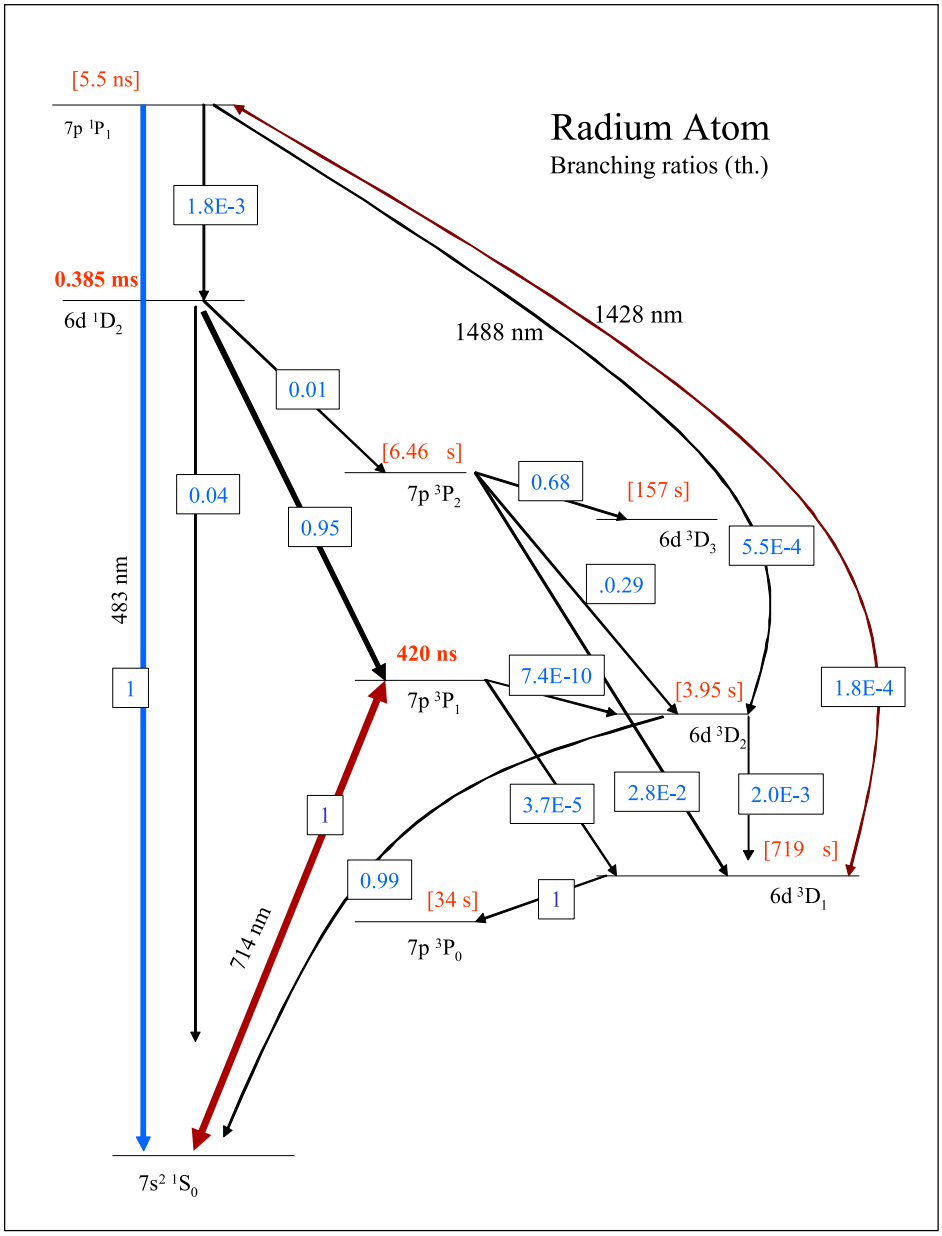

Figure 10.2: Level Scheme of the nine lowest states of ^{226}Ra showing the branching ratios of state to state transitions. Experimentally measured lifetimes are written in bold font. The theoretical lifetimes noted in the figure (in square brackets) and branching ratios indicated are obtained from Bieron *et al.* [22]. Calculations have also been made by Dzuba *et al.* [59].

10.1 Laser Systems

10.1.1 714 nm Laser System

We obtain 714 nm light from a Coherent MBR 110, titanium-sapphire laser. With 15 W of 532 nm pump light (using a Spectra Physics Millenia Laser), we get $\sim$ 800 mW of light at 714 nm which is distributed to multiple beams for the experiment after being appropriately frequency shifted. Long term frequency stability of the 714 nm light is achieved by locking the titanium-sapphire laser to a molecular iodine saturation spectroscopy line. We show a basic layout of the laser table used in distributing the 714 nm light in figure 10.3.

10.1.2 1428 nm Laser System

We generate 1428 nm light from a diode laser (Sacher LaserTechnik), which can supply up to 10 mW at 1428 nm. The light is amplified by injection locking an additional diode laser from QC Photonics, which can supply up to 150 mW. The nominal operating wavelength of the slave laser is 1425 nm, though with the injection locking, we get it to lase at the desired 1428 nm. The 1428 nm system is locked to a frequency stabilized Helium Neon Laser(Melles Griot 05-STP-901), which has a specified frequency stability of $\pm$2.0 MHz per hour. This is implemented via a transfer lock to a hermetically sealed, temperature stabilized Fabry-Perot cavity.

10.1.3 483 nm Laser System

We generate up to 5 mW of 483 nm light, to excite the $^1S_0$ - $^1P_1$ transition. We make use of a $\sim$ 1 cm long PPLN waveguide (From HC Photonics) for frequency doubling 966 nm from a diode laser. It has a specified doubling efficiency of $150\%/W/cm^2$. With approximately 50 mW of 966 nm light coupled into the waveguide, we generate $\sim 4.5mW$ of 483 nm light.

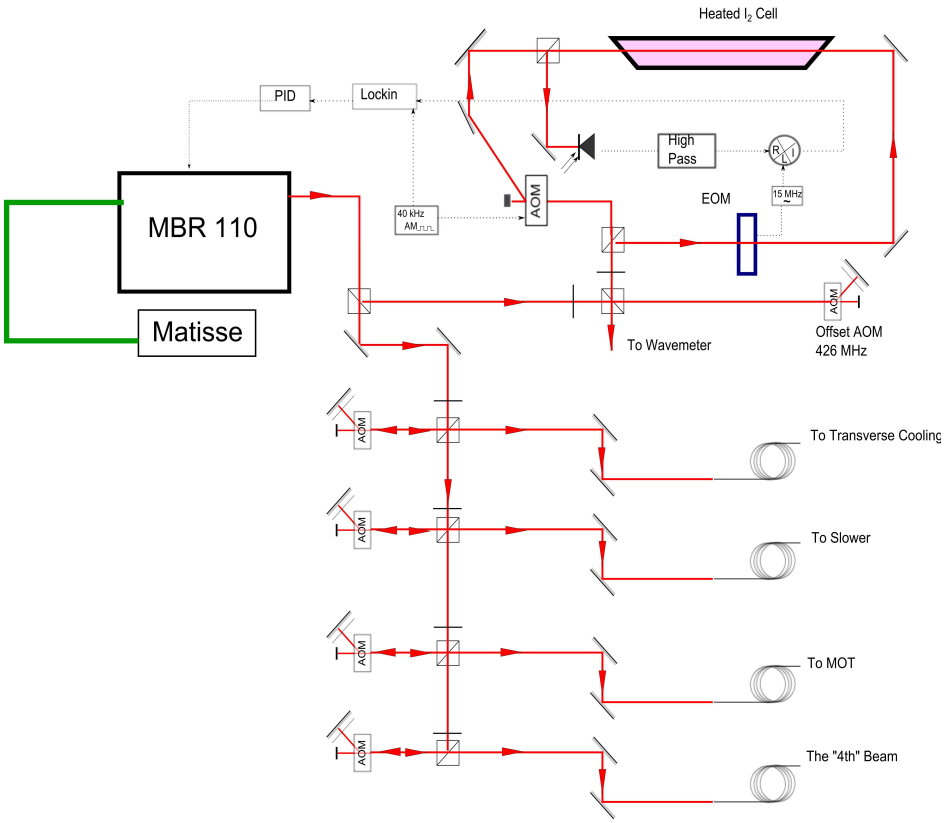

Figure 10.3: Setup of optics used for generating 714 nm light. The titanium-sapphire laser generates about 800 mW light at 714 nm, which is distributed to different parts of the experiment. Long term frequency stability is attained by locking to an FM saturation spectroscopy line in molecular iodine. The AOMs on the paths of the transverse cooling, slower, MOT, and the '4th' beam are all around 80.0 MHz; deviating from 80 MHz slightly depending on the detuning desired.

We achieve long term frequency stability of the 483 nm light by locking the 966 nm laser to the same frequency stabilized He-Ne laser used for stabilizing the 1428 nm light. As in the case of the 1428 nm system, this is achieved by a transfer lock via a dual wavelength hermiticaly sealed Fabry-Perot cavity. A schematic of the optics layout for generating and stabilizing light at 483 nm is given in figure 10.6

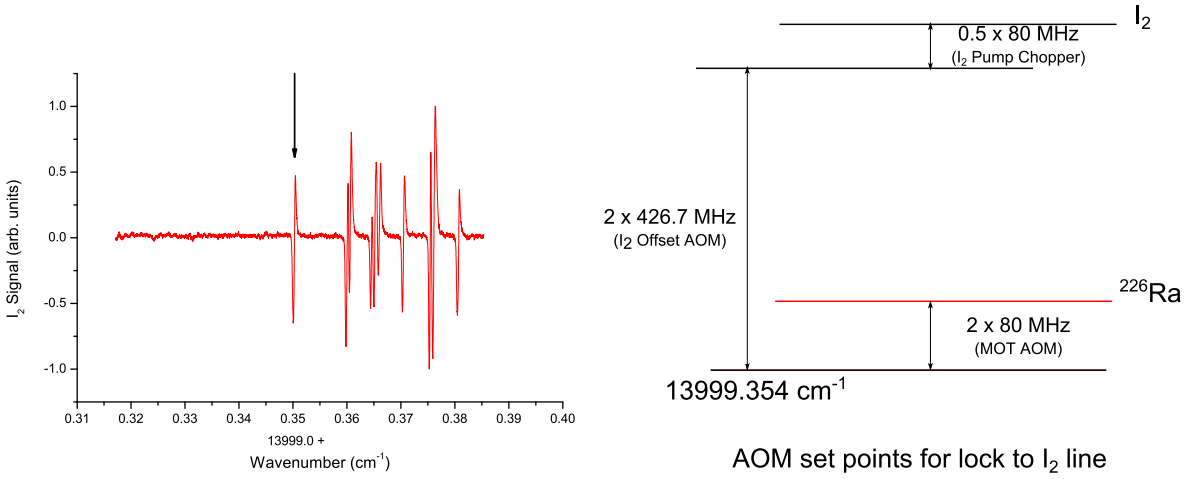

Figure 10.4: Iodine Saturation spectroscopy line and set points for trapping ^{226}Ra. We lock the 714 nm laser system to the iodine line indicated by the arrow on the left figure.

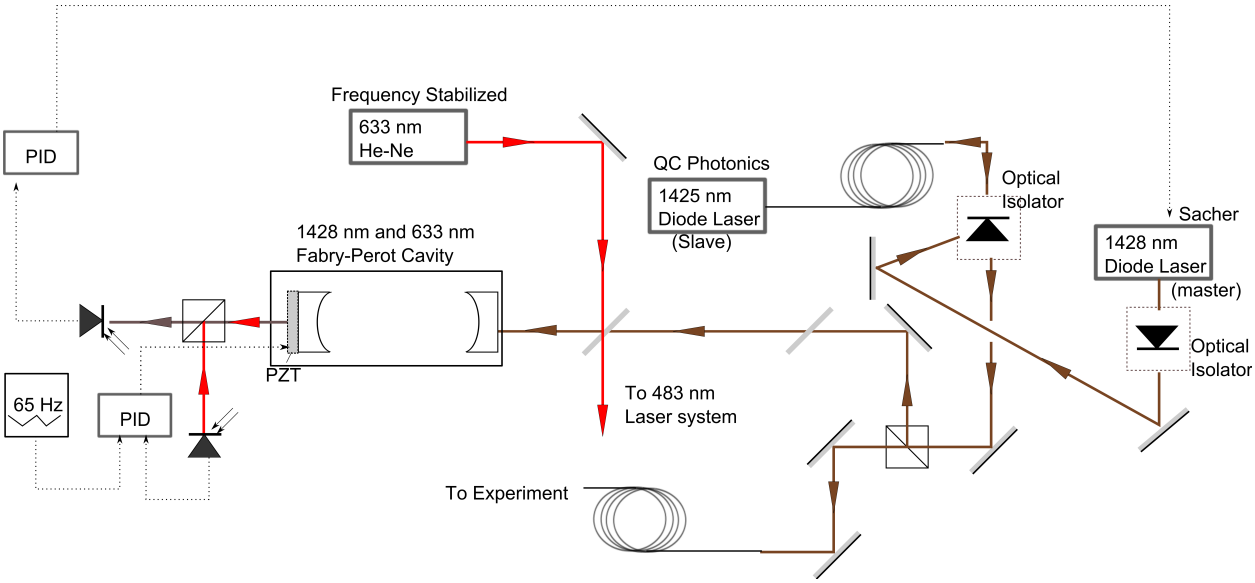

Figure 10.5: Setup of optics used for generating 1428 nm light. The Fabry-Perot is locked to the He-Ne, and the 1428 nm laser is locked to the cavity. Approximately 40 mW of 1428 light is available for use at the atomic beam line.

10.2 Vacuum System

The vacuum hardware is made of standard Type-316 and Type-304 stainless steel parts. We make use of a number of ion pumps which are shown in figure 10.7. We also make use of

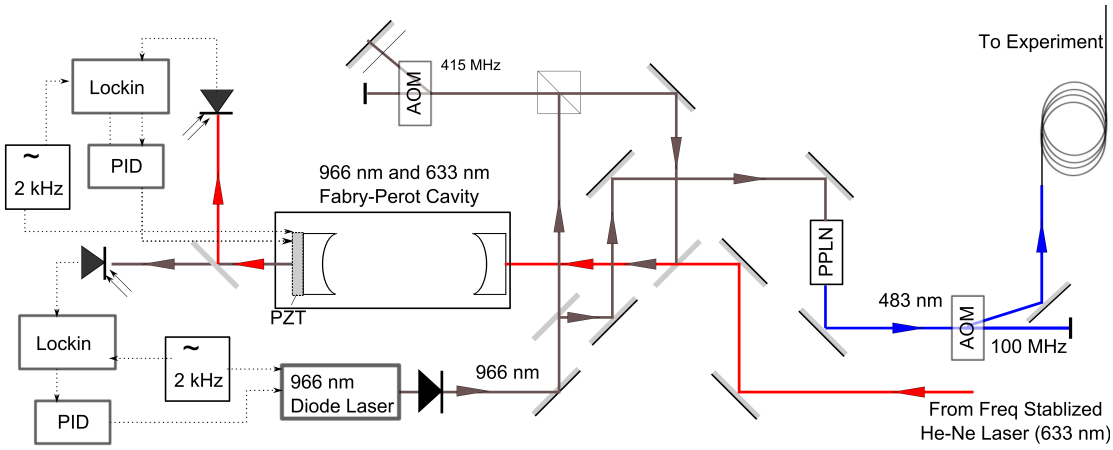

Figure 10.6: Setup of optics used for generating 483 nm light. We use a PPLN waveguide to frequency double 966 nm light. The frequency stabilization is achieved by locking the 966 nm to a frequency stabilized He-Ne. Up to 2 mW of 483 nm light is available for use at the atomic beam line

a non-evaporable getter pump, as well as a titanium sublimation pump in order to pump the hydrogen from the chamber. The Transverse cooling/oven chamber (known as the 'front end')is the higher pressure part of the beam line. This is due to elevated out-gassing rates from the heated parts of the oven. Also, the 'front end' is frequently vented when the source is being reloaded. We have some degree of differential pumping between the two chambers, as the Zeeman slower serves as a conductance limiter. With the oven operating at $500°C$, we maintain equilibrium pressures of $\sim 3 \times 10^{-8}$ Torr in the transverse cooling chamber, and $\sim 1 \times 10^{-9}$ Torr in the MOT chamber. Most of the residual gas in the vacuum system is hydrogen as indicated by a residual gas analyzer (RGA) scan.

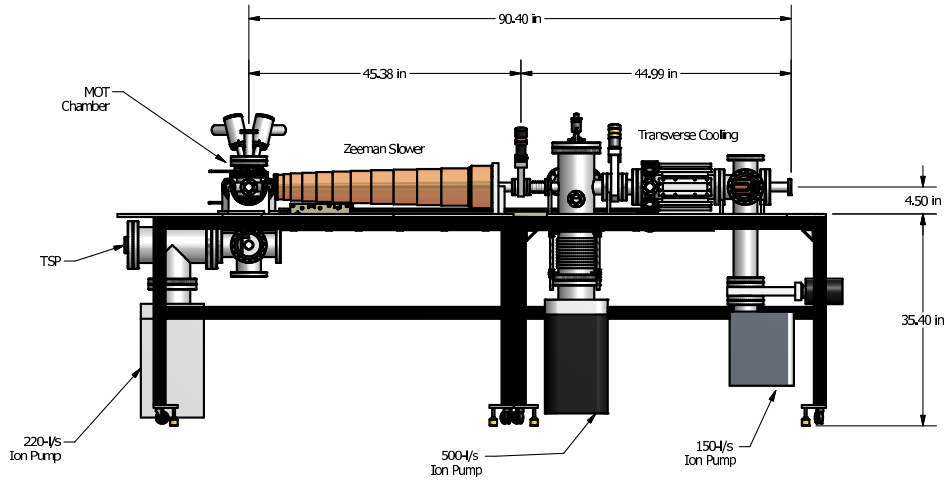

Figure 10.7: Schematic of atomic beam line

10.3 Atomic Beam Generation and Slowing

10.3.1 The Oven

We obtain ^{226}Ra and ^{225}Ra in the form of $RaNO_3$ dissolved in 0.1M nitric acid. In order to create a beam of metallic radium, we must

(1.) chemically reduce the radium salt to elemental radium.

(2.) heat up the sample so that the vapor pressure is high enough to yield an effusive beam which we can work with for a couple of weeks, but not too high that the source is consumed very quickly.

For all the studies described here ^{226}Ra is used. Even though the interesting isotope for EDM studies is ^{225}Ra, the long lifetime of ^{226}Ra makes it a convenient isotope for understanding and perfecting techniques for handling radium in optical traps. Up to 500 μCi (i.e. 500 μg) of ^{226}Ra in the form of $RaNO_3$ in 0.1M Nitric acid is pipetted onto a piece of aluminum foil. The acid is allowed to evaporate, and then the foil containing the radium along with a piece of metallic barium, ($\approx$ 50 mg) is placed in a crucible. The crucible is made

of titanium, and serves as a sample holder while the sample is heated. There is a nozzle on the output (i.e. front) end of the crucible. On the rear end of the sample holder is a slot for a thermocouple, which we use to monitor the temperature. See figure 10.8 for details.

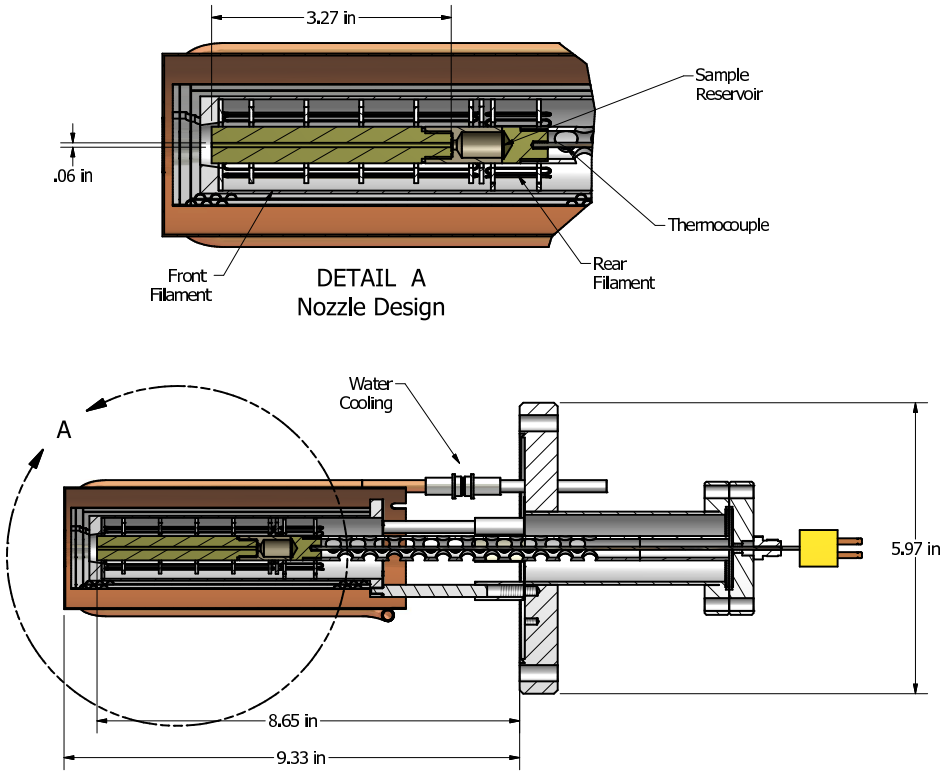

Figure 10.8: Schematic of the oven along with the the crucible, which holds the radium atoms. The heater elements are operated such that the crucible is radiatively heated to temperatures of $\sim 500°$ C, as recorded by the thermocouple shown in the figure

The heater element for the oven consists of a pair of windings of tantalum wire, which surround the crucible assembly. By running ~ 3.5 Amps through the heater element, we can radiatively heat the crucible to temperatures over 600 °C. Surrounding the heater element is a copper heat shield around which cooling water flows. A schematic of the oven and crucible assembly is shown in figure 10.8.

The very first time we insert a new sample, we need to 'break-in' or 'crack' the load. This involves heating the crucible while monitoring the flux of atoms in the emerging atomic

beam. Initially, no beam is detected. At a critical temperature $\sim 620°C$, we believe that the chemical reaction leading to the reduction of the $RaNO_3$ by barium occurs. This leads to the release of metallic radium atoms. Thereafter, we can operate the oven at more modest temperatures and still have a strong flux of radium atoms. For day to day operations, we typically operate the oven at $\sim 500\,°\mathrm{C}$. As we use up the inventory of radium loaded, we gradually increase the operating temperature in order to maintain a comparable atomic flux to when the oven was newly loaded.

10.3.2 Transverse Cooling / Zeeman Slowing

We increase the forward brightness of the atomic beam that emerges from the oven by having it pass through a stage of transverse laser cooling [108]. We typically use about 60 mW of 714 nm light for cooling the two transverse dimensions. When optimally aligned, the transverse cooling stage leads to an increase in the loading rate of the magneto - optical trap by up to a factor of 80.

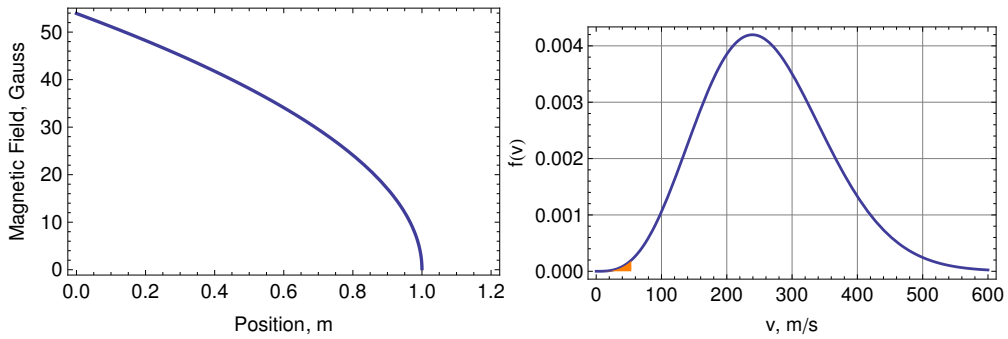

Figure 10.9: Designed field of the zeeman slower is shown on the left panel. The atomic beam velocity distribution at T = 500 ° C. The shaded region shows the fraction of the atoms emitted from the atom that are slowed down with a 1 m long 714 nm Zeeman slower. With a most probable velocity of 250 m/s, this corresponds to $\approx 3 \times 10^{-3}$ of the forward flux. In the future, we expect to capture a larger fraction of the atoms in the distribution by making use of 483 nm slowing stage.

Radium atoms emerge from the transverse cooling region with a longitudinal velocity

profile given by a Boltzmann distribution characteristic of the oven temperature.

$$f(v) = \frac{M^2}{2k_B^2 T^2} v^3 \ \mathrm{Exp}\left[\frac{-\mathrm{Mv}^2}{2\mathrm{k_B T}}\right] \tag{10.1}$$

At $\sim 500\,^{\circ}\mathrm{C}$, the most probable velocity of the atoms is 250 m/s. On the other hand, the maximum acceleration of the atom due to the scattering of 714 nm photons is 2900 ms^{-2}. With MOT beams approximately 40 mm in diameter, this leads to a MOT capture velocity of $\sim$ 30 m/s. With the constraint of the Zeeman slower being 1 m long, we can at best slow down $\sim 3 \times 10^{-3}$ of the atoms effusing from the oven. The magnetic field profile of our Zeeman slower, along with the thermal velocity distribution of radium atoms emerging from the oven is shown in figure 10.9.

10.4 Magneto-Optical Trap of Radium

We construct a MOT of radium atoms from the combination of a 3-dimensional optical molasses formed from 714 nm light, a quadrupole magnetic field with a field gradient of 1 Gauss/cm near the field minimum, and a single repump laser at 1428 nm. The first radium MOT was reported from our group in 2007 by Guest *et al.* [77].

We detect atoms in the MOT by collecting fluorescence onto a photo-multiplier tube, or by imaging the atoms with a CCD camera (Andor Luca-R). For PMTs, we use photon counting modules (H7421) from Hamamatsu which have a quantum efficiency of 10 % at 714 nm. The advantage of using the PMT over the camera is that we can get very fast response. Because the lifetime of the $^3P_1$ level is 420 ns, we can excite the atoms, and turn off the light before all of the atoms spontaneously decay back to the ground state. In order to implement this, we amplitude modulate the light going to the MOT beams at 1 MHz, with a on/off duty cycle of 0.5. We then only consider the photons that are scattered in

coincidence with the 'off' phase of the MOT beam chopping. This yields excellent background reduction. Using this scheme, we can have sensitivity to a few atoms in the MOT. However, the fast modulation scheme is still very useful in a time of flight temperature measurement as described in Appendix A, and for atomic beam fluorescence measurements because of the dearth of signal carrying photons compared with scattered light.

10.4.1 Blackbody Repump Dynamics

As mentioned above, we repump atoms in the MOT using the ${}^3D_1 - {}^1P_1$ transition. The ${}^3D_1$ level is fed from the ${}^3P_1$ level with a branching ratio of 5×10^{-5}. Once in an average of 20000 cycles on the 714 nm transition, a radium atoms falls into the ${}^3D_1$ level. If the atoms are not repumped from the ${}^3D_1$, they begin to fall freely under gravity, and to decay to the ${}^3P_0$ level. With no repumping, the mean lifetime of the atoms in the ${}^3D_1$ level is $\sim 700\mu s$.

Now, because of the relative spacing of the states in the ${}^3D_J$ and ${}^3P_J$ manifold, it turns out that there is a significant overlap in the room temperature blackbody photon spectrum with the frequencies for transitions between the metastable levels. In other words, atoms which fall into the ${}^3P_0$ level have a significant probability of being repumped to ${}^3D_1$ by room temperature blackbody photons. Likewise, atoms can be repumped by blackbody photons from ${}^3D_1$ to the ${}^3P_1$ level. Guest *et al.* [77] reported results that support this picture of blackbody repumping. The blackbody repumping mechanism also helped explain the performance of the ^{225}Ra MOT with only one repump laser. Because of its hyperfine structure, the ${}^3D_1$ and ${}^1P_1$ levels are both split into two levels (F = 3/2 and F = 1/2) in ^{225}Ra. Instead of having one transition from ${}^3D_1$ to ${}^1P_1$, there are consequently four. Guest *et al.* were able to sustain a ^{225}Ra MOT by repumping on only one of the four available transitions from ${}^3D_1$ to ${}^1P_1$ [77]. They could get away with doing so because the room temperature blackbody photons remixed the population, such that those atoms which had

fallen into an un-pumped hyperfine level were given a second chance at being repumped by being excited back to $^3P_1$ by the ambient photons.

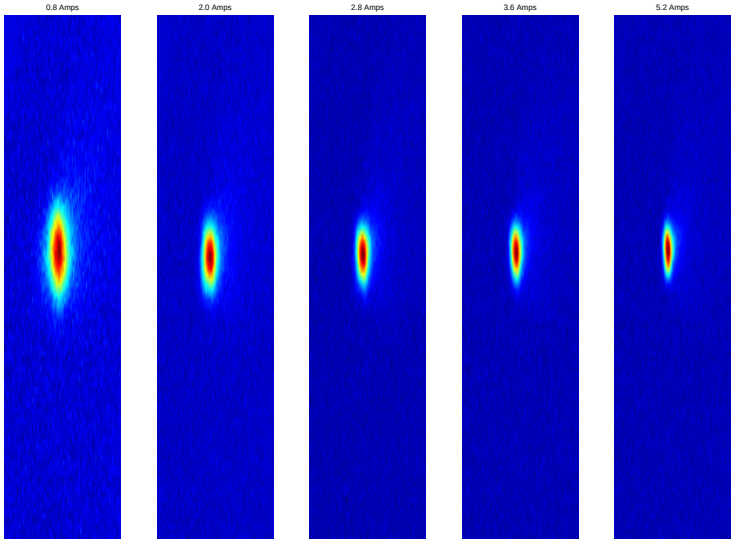

Figure 10.10: Compressing Atoms in MOT by increasing Magnetic field gradient [124]. This enables us to have increased sensitivity in detecting the presence of atoms, and also in increasing the spatial overlap with an optical dipole trap.

10.4.2 Operating Modes

As we described in section 9.2, the purpose of the MOT is to serve as an atom accumulator which is used to load an optical dipole trap. We have three basic operating conditions namely

Loading In this mode, we operate the MOT in a manner whereby we optimize the loading rate of atoms into the MOT. The magnetic field gradient of the MOT is ~ 1 Gauss/cm, and the laser is detuned to ~ 3 linewidths.

Probing In the probing mode, we optimize the signal to noise ratio with which we can detect the atoms in the MOT. This is particularly important when we need to detect

very few atoms. We increase the magnetic field gradient to up to 5 Gauss/cm because it leads to a more compact cloud and a consequently higher SNR. Furthermore, having a compact MOT is advantageous when we transfer atoms from the MOT into an optical dipole trap (ODT), as it enlarges the spatial overlap of the MOT cloud with the dipole trap. This will be treated in chapter 12.

Cooling In this operating mode, we tune the system in order to minimize the temperature of the atomic cloud. It is in this stage that the atoms are transferred into a far off resonance optical dipole trap.

We give a table of the set points for the different modes of operation in 10.4.2.

Table 10.3: Settings for lasers and magnetic field gradients during the loading and probing and cooling phases of the ^{226}Ra MOT. The given intensities for the MOT are for a single beam. $\Gamma = 2\pi \times 380$ kHz, $I_s = 140$ mw/cm^2

	Slower		MOT		T C		B-Field Gradient
	Δf	I	Δf	I	Δf	I	(Gauss/cm)
Loading	-3Γ	$20I_s$	-3Γ	$20I_s$	0	$20I_s$	1
Probing	Off		-1.5Γ	I_s	Off		5
Cooling	Off		$-\Gamma$	I_s	Off		5

10.4.3 Outlook for Improvement

Large atom numbers are critical for the success of an EDM search with trapped radium atoms. Presently, depending on the age of the oven load and the operating temperature, we can accumulate up to 10^5 atoms in the MOT. The measured lifetime of the MOT is about 25 seconds, and is limited predominantly by collisions with background gas. Future work to improve the total number of atoms available would include improving the quality of the

vacuum from 10^{-10} Torr to 10^{-11} Torr. This would allow for the accumulation of atoms over a longer period. Another step that would improve the loading rate of the apparatus involves using the 483 nm transition to slow atoms down. Because it is two orders of magnitude stronger than the 714 nm transition, a larger fraction of the thermal velocity distribution can be captured. We consider the relative gains that would be made for a slower of length L_0 by integrating equation 10.1 up to a maximum velocity $v_0 = \sqrt{L_0\ a_{\max}/2}$. For example, with a 10 cm long slower, a capture velocity of 181 m/s is obtained. In order for this to be feasible however, repumping from the $^3D_1$, $^3D_2$ and $^1D_2$ must be implemented due to the large branching fractions to them from the $^1P_1$ level.

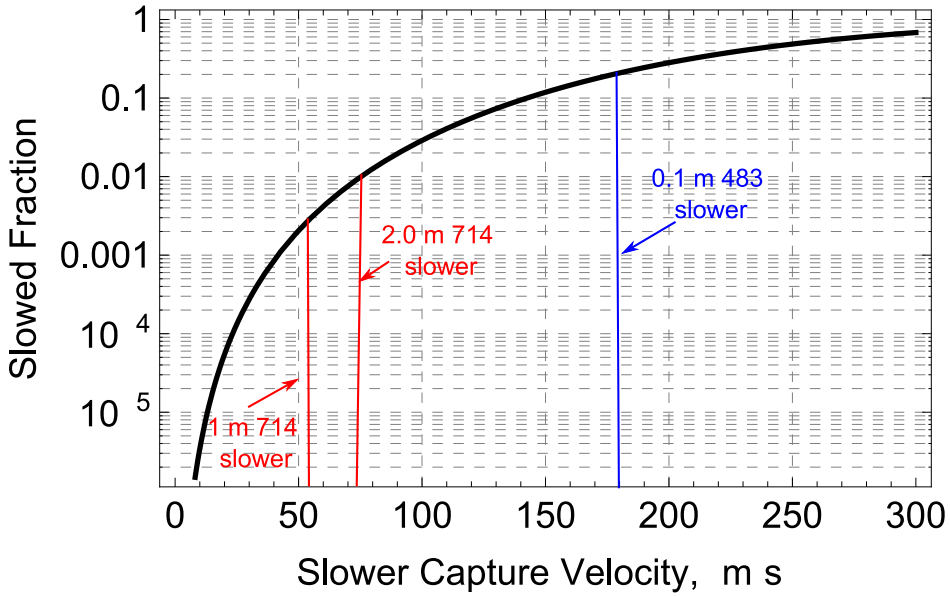

Figure 10.11: The fraction of atoms emitted by the oven which are slowed down by the Zeeman slower as a function of the capture velocity. The oven is assumed to be operating at 500 ° C. We use an average deceleration of $a_{\max}/2$ for 714 nm and 483 nm, as given in table 10.2

In chapter 11, we will describe a measurement of the $7s6p^1D_2$ atomic lifetime of ^{226}Ra. This measurement was our first use of the ultracold sample of radium atoms to study radium atomic structure. We will also, in chapter 12 describe our proposal to further study radium

atomic structure by determining the differential DC polarizabilities of two transitions in the radium atom.

CHAPTER 11

LIFETIME OF THE 1D2 ATOMIC STATE OF RADIUM

We have published the contents of this chapter before in [160]. Some sections of the text are reproduced verbatim.

11.1 Motivation

Radium is the highest-Z neutral atom for which laser cooling and trapping have been demonstrated [77]. This makes it an attractive candidate for tests of fundamental symmetries, since relativistic and finite-size-nuclear effects are enhanced in heavy atoms and since laser techniques permit long observation times and potentially precise measurements with small samples.

There are two transitions from the ground state that can be used for laser trapping and cooling of atomic radium (see figure 10.1). The intercombination transition $^1S_0$ - $^3P_1$ (τ = 422 ns) at 714 nm can be repeatedly excited to provide a maximum acceleration of $3{\cdot}10^3$ m s^{-2}. This transition is quasi-cycling, with an estimated branching ratio of $5{\cdot}10^{-5}$ to $^3D_1$. This causes illuminated atoms to decay to $^3D_1$ in about 20 ms, but a single repump laser tuned to the $^3D_1$ - $^1P_1$ transition at 1428 nm is sufficient to bring the atoms back into the cooling cycle. The other possible transition is the allowed $^1S_0$ - $^1P_1$. Compared to the intercombination transition, the singlet-to-singlet transition has a stronger transition strength and a shorter wavelength, consequently it can be used to achieve an acceleration as large as $3{\cdot}10^5$ m s^{-2}, 100 times larger than the first scheme. However, the $^1P_1$ state has much stronger leak channels. The branching ratio to $^1D_2$ and triplet D states is estimated to be $2{\cdot}10^{-3}$. Consequently, a radium atom can scatter on average only 500 483 nm photons before going dark. Recent work demonstrating the trapping of neutral barium has shown that manipulation of such "leaky" atomic systems is possible with sufficiently numerous repump

lasers [45]. The work presented here will help evaluating the feasibility of using the $^1S_0$ - $^1P_1$ transition for more efficient slowing and trapping of radium by measuring previously unknown lifetimes and branching ratios of excited states in radium.

The lifetime of the $^1D_2$ has been calculated a number of times and the results range from 129 μs to 1.37 ms (see Table 11.1 for references). The difficulty in atomic theory arises from a near cancellation of two large transition amplitudes [54]. Previous determination of the $^3P_1$ lifetime was performed by our group using a thermal beam of radium atoms [146]. The long lifetime of $^1D_2$ makes that approach difficult. Instead, the measurement presented here is performed on cold ^{226}Ra atoms prepared in a magneto-optical trap (MOT). This work represents only the second experimental determination of an excited state lifetime in atomic radium. It will help anchor atomic theory calculations and better model the interaction between the radium atom and lasers used to manipulate it.

11.2 Experimental Details

The apparatus for laser cooling and trapping of radium atoms is described in detail in [77]. In short, neutral ^{226}Ra ($t_{1/2}$ = 1600 yr) atoms emerging from a thermal atomic beam source at 500 C are transversely cooled, slowed down in a Zeeman slower, and captured in a MOT, all by exciting the intercombination transition, $^1S_0$ - $^3P_1$, at 714 nm. A diode laser at 1428 nm is tuned to the $^3D_1$ - $^1P_1$ transition and overlapped with one of the MOT beams to repump atoms from $^3D_1$. Typically 500-1000 cold ^{226}Ra atoms are captured in the MOT with a trap lifetime of 2 s.

Light at 483 nm was produced by frequency doubling a 100 mW diode laser at 966 nm in a 1.0 cm periodically poled lithium niobate waveguide. This laser was stabilized to a helium-neon-laser referenced Fabry-Perot cavity. Blue light with an intensity of 100 mW cm^{-2} was directed into the MOT at a 5 degree angle to one of the MOT beams and was retro-reflected

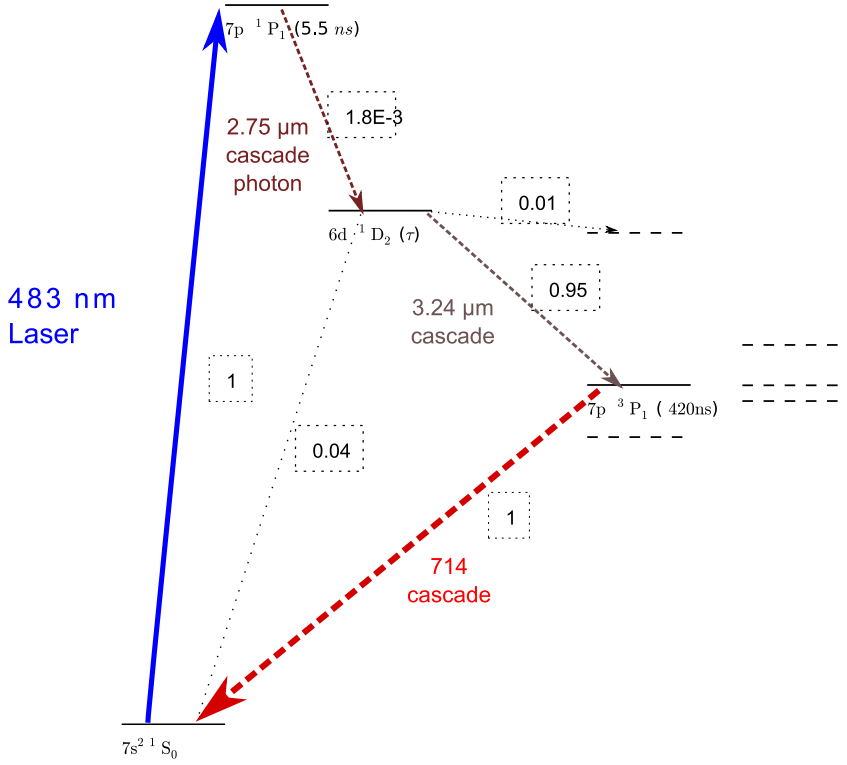

Figure 11.1: In measuring the ^{1}D$_2$ lifetime, we populated the ^{1}P$_1$ level by turning on a resonant 483 nm beam for some time. Thereafter, the excited atoms cascaded down to the ground state. The longest lived state on the path was the $^1D_2$ level. By measuring the arrival time of 714 nm photons after the 483 nm pulse, we determined the ^{1}D$_2$ lifetime ,τ. Branching ratios are obtained from theory [22, 58]

using a lens and mirror to adjust the intensity of the reflected beam. When tuned to the ^{1}S$_0$-^{1}P$_1$ resonance, the blue laser pumps atoms to the metastable states, causing loss from the trap. The 483 nm laser frequency and beam pointing is adjusted for maximal trap loss at low intensity. The ^{1}S$_0$-^{1}P$_1$ resonance frequency in ^{226}Ra was measured to be 20715.598(4) cm^{-1} using a laser wavelength meter (Bristol Instruments 621). This value is 0.1 cm^{-1} below the

Table 11.1: Summary of theoretical estimates of the value of the $^1D_2$ lifetime.

Work	Theory	Experiment
[58]	710 μs	
[59]	129 μs	
[22]	1.37 ms	
This work		385(45) μs

value determined from grating spectrometer measurements in the 1930s [111, 137] and places the $^3D_1$ level at 13715.76 cm^{-1} based on the measurement of the $^3D_1$-$^1P_1$ wavelength [77].

For the lifetime measurement, the trapping light at 714 nm and the repump light at 1428 nm are kept on for 990 ms in the atom capture phase, and are then blocked by mechanical shutters for 10 ms in the measurement phase. The two phases cycle at 1 Hz rate. To keep the detector dark counts low, the detector is shuttered with a mechanical shutter that is opened only after the MOT light is shuttered. During the first 5 ms of the 10 ms measurement phase, the cold atoms fall while the detector shutter opens. They are then excited by a 100μs pulse of 483 nm light on the $^1S_0$ - $^1P_1$ ($\tau \sim 5.5$ ns) transition. Fast amplitude modulation of the 483 nm light is achieved with an acousto-optical modulator. Each excited atom emits either a blue photon at 483 nm or decays to one of the excited metastable states. Those metastable states then eventually decay to the ground state. Theoretical branching ratios predict that most of the atoms pumped to $^1D_2$ will decay by emitting a single red photon at 714 nm while the atoms pumped to other states will not decay rapidly via $^3P_1$. The atomic fluorescence at 714 and 483 nm is separated by color with a dichroic mirror and optical band-pass filters and detected by two separate photo-multiplier tubes. A computer-based data acquisition system records the arrival times of the detected photons.

11.3 Results

Figure 11.2 a shows the red fluorescence collected from the MOT when the blue pulse is applied without shuttering the MOT beams. During each blue flash, the MOT fluorescence promptly decreases, declining to nearly background levels by the end of the pulse. Between 5% and 20% of the MOT fluorescence returns within 1 ms of the end of the blue flash. The relative intensities of the incoming beam and its reflection were adjusted to maximize the fraction of atoms which returned following the flash.

Figure 11.2 b shows the red fluorescence collected from the atoms when the MOT light is blocked. Red fluorescence rises during the blue exposure and falls following it. The delayed red fluorescence is observed only when the blue laser is tuned to the $^1S_0$ - $^1P_1$ resonance.

The arrival-time histograms were fitted using maximum likelihood and weighted least-squares. Data from 1 ms before and 3.5 ms after the blue exposure were used, while the rising red fluorescence during the blue flash was ignored in finding the lifetime. Since the count rates in the detector were low, maximum likelihood was chosen as the more appropriate algorithm, though the two techniques agreed within their uncertainties. Data taken under the same experimental conditions were summed; three separate experimental conditions were fitted separately. The data taken with the blue beams imbalanced and with the repump on during the blue pulse, had longer but insignificantly different fitted lifetimes. A weighted average of the three fits gives a lifetime of 385(22) μs.

The observed delayed red fluorescence could be influenced by factors other than the $^1D_2$ lifetime. In a previous work it was observed that room-temperature blackbody radiation pumps atoms from $^3P_0$ to $^3D_1$ at a rate of 200 Hz[77]. The radiation should also pump atoms from $^3D_1$ to $^3P_1$ at approximately 40 Hz. This would introduce an additional decay mechanism for the red fluorescence and could bias the lifetime as much as 5% toward longer lifetimes if the population in the $^3D_1$ state is as large as 75%. In order to test whether the

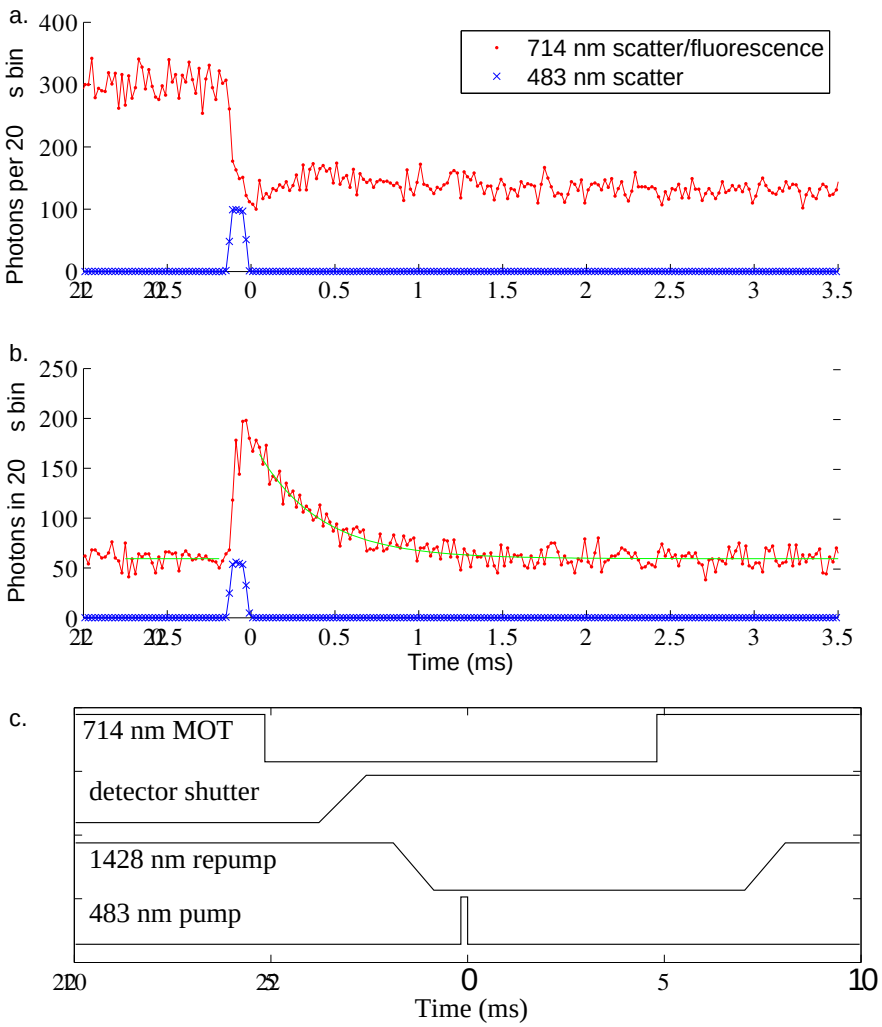

Figure 11.2: (a) Suppression of MOT fluorescence at 714 nm caused by 483 nm light pumping radium to metastable states. This panel represents data accumulated for 11 minutes with the MOT beams kept on. (b) 714 nm flash following 483 nm excitation of radium atoms shows the decay of $^1D_2$. The MOT beams are off for the collection of these data. This panel represents data accumulated for 10 hours with the timing structure in (c). (c) Timing diagram of the measurement procedure.

population of cold atoms in the $^3D_1$ state affected the lifetime measurement, some of the data were taken with the 1428 nm laser on during the blue pumping. No effect was resolved.

The scattering of blue light pushes the atoms, and the motion of the atoms out of the viewing area of the detector could bias the resulting lifetime measurement. The atoms can

Table 11.2: Error budget.

Effect	Contribution	
black-body repumping from 3D1	19	
motion from recoils	31	
motion from gravity	5	
statistical	26	
Total	45	μs

scatter an average of 500 blue photons before decaying to the $^1D_2$ metastable state. 500 single-photon recoils at 483 nm confer an average velocity of 2 m s^{-1} to the atoms. During the duration of the delayed red flash the recoiling atoms can move an average of 1 mm, comparable to the 4 mm diameter viewing area of the detector. To test whether the atoms were leaving the viewing area before the decay was finished, we took some of the data with the retro-reflection blocked, providing a maximum imbalance in the momentum imparted by the blue pump beam. The lifetime measured with a maximally imbalanced blue excitation was longer by 8% than the lifetimes taken with balanced beams, less than the 13% statistical uncertainty. The failure of an imbalanced beam to shorten the measured lifetime is evidence that the motion of the atoms out of the field of view of the detector does not influence the lifetime measurement at the 10% level.

The radium atoms can also move away from the viewing region due to its initial velocity ($\sim$3 cm s^{-1}, 150 μm in 5 ms) and to falling under gravity (125 μm in 5 ms). Both effects are small compared to the effect of pushing by the blue light.

11.4 Discussion

The lifetime of $^1D_2$ is expected to be dominated by the decay branch to $^3P_1$. The presence of the former state complicates cooling using the 483 nm transition by sequestering atoms and preventing them from participating in cooling for fractions of a millisecond. this measurement

permits more accurate modeling of the atomic populations in the presence of 483 nm and repumping light.

This measurement of the radium $7s6d\ ^1D_2$ lifetime is limited by statistics; larger numbers of trapped atoms would permit more thorough investigation of systematic shifts to the measured decay, particularly experimental limits on the shifts caused by imbalanced forces and the viewing area of the detector

In addition to excited-state lifetimes, experiments with cold radium atoms can also probe hyperfine splittings in some excited states and atomic polarizabilities to provide experimental anchors for the models of the atomic wave functions. It is interesting to note that the metastable states with the longest radiative lifetimes $^3P_0$ and $^3D_3$, will absorb room-temperature blackbody photons in 5 and 200 ms respectively, limiting the prospects for room-temperature experiments in metastable states of radium. The $^3D_2$ state, only 5 cm^{-1} below$^3P_1$, is only slightly affected by blackbody radiation.

In summary, this lifetime measurement for $^1D_2$ and refinement of the energies of the $7s7d\ ^1P_1$ $7s6d\ ^3D_1$ levels in atomic radium should permit the construction of more accurate models of the atom, both for predicting the distribution of the atoms in their internal states for experiment, and for interpreting the observable signatures of interesting physics arising from interactions with the nucleus.

CHAPTER 12

AC AND DC STARK SHIFTS IN RADIUM

The Stark shift of an atomic level in the presence of an external electric field is a function of the frequency of oscillation of the field, and so we distinguish between DC and AC Stark shifts. Recall from our discussion in chapter 8 that as a consequence of parity and time-reversal symmetry, a non-degenerate eigenstate cannot have a permanent electric dipole moment. In other words, given a state $\psi_a(J)$ with an energy ε_a, The first order perturbation to its energy due to the coupling of a permanent electric dipole moment $\boldsymbol{\mu} = \sum_i e\boldsymbol{r_i}$ to the electric field $\boldsymbol{E}$ vanishes.

$$H_a^{(1)} = \langle \psi_a(J) | \, \boldsymbol{\mu} \cdot \boldsymbol{E} \, | \psi_a(J) \rangle = 0 \tag{12.1}$$

However, a non-degenerate eigenstate can have an *induced* electric dipole moment. This can be seen by considering its coupling to other states in the system in the presence of an external electric field. In second order perturbation theory, the shift of an atomic level as a function of applied electric field which oscillates at a frequency ω is,

$$H_a^{(2)} = \sum_n \frac{\langle \psi_a(J_a) | \, \boldsymbol{\mu} \cdot \boldsymbol{E} \, | \psi_n(J_n) \rangle \, \langle \psi_n(J_n) | \, \boldsymbol{\mu} \cdot \boldsymbol{E} \, | \psi_a(J_a) \rangle}{\varepsilon_a - \varepsilon_n - \omega^2} \tag{12.2}$$

Here $\hbar = c = 1$ and the sum is over eigenstates of the unperturbed states of the system $|\psi_n\rangle$. Following the derivation in [9], the quadratic Stark shift of a state with quantum numbers $(J, M))$ takes the form

$$W(J, M_J) = -\frac{1}{2}\alpha^{(0)}(J)E^2 - \frac{1}{4}\alpha^{(2)}(J)\frac{(3M_J^2 - J(J+1))}{J(2J-1)}(3E_Z^2 - E^2) \tag{12.3}$$

where $\alpha^{(0)}$ and $\alpha^{(2)}$ are the scalar and tensor polarizabilities respectively. The direction of

the electric field is chosen as the quantization axis. In terms of the reduced matrix elements,

$$\alpha^{(0)}(J_a) = \frac{2}{3(2J_a+1)} \sum_n (-1)^{J_a - J_n} \frac{(\varepsilon_a - \varepsilon_n) \left| \langle J_a \,||\, \boldsymbol{\mu} \,||\, J_n \rangle \right|^2}{(\varepsilon_a - \varepsilon_n) - \omega^2} \tag{12.4}$$

and

$$\begin{aligned} \alpha^{(2)}(J_a) =& \sqrt{\frac{5}{6} \frac{J_a(2J_a-1)}{(2J_a+3)(J_a+1)(2J_a+1)}} \\ & \times \sum_n (-1)^{J_a - J_n} \left\{ \begin{array}{ccc} 1 & 1 & 2 \\ J_a & J_a & J_n \end{array} \right\} \frac{(\varepsilon_a - \varepsilon_n) \left| \langle J_a \,||\, \boldsymbol{\mu} \,||\, J_n \rangle \right|^2}{(\varepsilon_a - \varepsilon_n) - \omega^2}. \end{aligned} \tag{12.5}$$

In the case where we have a nuclear spin $I \neq 0$, the good quantum number is $F = I + J$, and each magnetic sub level is shifted an amount given by [88]:

$$\begin{aligned} W(F, m_F) =& -\frac{1}{2}\alpha^{(0)}(F)E^2 \\ & - \alpha^{(2)}(F) \frac{[3M_F^2 - F(F+1)][3X(X-1) - 4F(F+1)J(J+1)]}{(2F+3)(2F+2)2F(2F-1)2J(2J-1)} (3E_Z^2 - E^2) \end{aligned} \tag{12.6}$$

where

$$X = F(F+1) + J(J+1) - I(I+1). \tag{12.7}$$

It follows then from equation 12.5 that the tensor polarizability $\alpha^{(2)}$ vanishes for $J = 0$ or $J = 1/2$. Other slightly different expressions for the scalar and tensor polarizabilities are reported in the literature such as [79]. Their results are equivalent to 12.4 and 12.5 in the second order of perturbation theory.

12.1 Proposal for experimentally determining DC polarizabilities of radium

We propose an experiment to determine the differential DC polarizabilities of two transitions in radium namely the $7s^2\ ^1\mathrm{S}_0 \rightarrow 7\mathrm{s}7\mathrm{p}\ ^3\mathrm{P}_1$ transition at 714 nm, and the $7s^2\ ^1\mathrm{S}_0 \rightarrow 7\mathrm{s}7\mathrm{p}\ ^1\mathrm{P}_1$ transition at 483 nm. The idea is to measure the transition frequency as a function of an applied electric field, and based on which the differential scalar and tensor polarizabilities will be derived.

The motivation for these experiments is two fold. First, it will yield interesting properties of radium atoms that will help anchor atomic structure calculations. Secondly, it is important to understand the induced dipole moments of radium, as we aim at setting limits on the possible existence of its permanent electric dipole moment. Furthermore, many of the experimental techniques that we propose to use in determining the DC polarizabilities are the same as those required for implementing the permanent EDM measurements proposed in section 9.2.

12.1.1 Estimates for DC polarizabilities of low lying states in radium

No measurements of the DC polarizabilities of radium have been performed. Some atomic lifetimes and energy levels have been experimentally determined. With the few experimental results serving as checks, theorists have published compilations of matrix elements for state to state transitions. Atomic structure calculations in radium have been published by Bieron *et al.* [20, 19, 23] and Dzuba *et al.*[56, 57]. Applying the published results from Dzuba *et al.* for the lowest states, as well as some unpublished results we obtained from private communications [55], we use equations 12.4 and 12.5 to calculate the polarizabilities of the lowest lying $^1S_0$, $^1P_1$, $^3P_1$ and $^3D_2$ states in radium. The calculations include their coupling to the 30 lowest lying states. These calculations give us a sense of the scale of the shifts

we need to resolve in order to perform an experimental determination of the differential polarizabilities.

We report our estimates for the DC polarizabilities for select states of ^{226}Ra in table 12.1 given in cgs units [1]

Table 12.1: Estimates for the DC polarizabilities for states in ^{226}Ra, given in cgs units.

	$\alpha^{(0)}$ (cm^3)	$\alpha^{(2)}$ (cm^3)
^{1}S$_0$	3.21×10^{-23}	-
^{1}P$_1$	-1.5×10^{-23}	-2.96×10^{-24}
^{3}P$_1$	-2.8×10^{-20}	2.6×10^{-21}

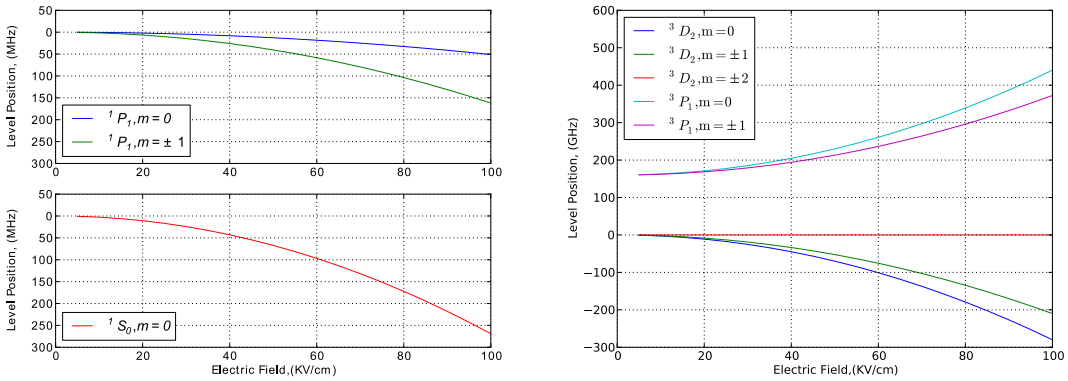

Figure 12.1: On the left panel, we have the calculated DC Stark shift for ground state$^1S_0$ and $^1P_1$ manifold. On the right panel, we have the calculated DC Stark shift for states in the $^3P_1$ and $^3D_2$ manifold. Because of the near degeneracy between $^3P_1$ and $^3D_2$, they are strongly mixed leading t0 the large polarizabilities. The direction of the electric field defines the quantization axis z.

1. Polarizabilities have units of volume. In atomic units, they are given in terms of a_0^3. In cgs, units, they are given in cm^3, while the conversion to SI units is $\alpha(\mathrm{Cm}^2/\mathrm{V}) = 4\pi\varepsilon_0 \times 10^{-6}\alpha(\mathrm{cm}^3) = 1.11265 \times 10^{-16} \times \alpha(\mathrm{cm}^3)$. When measuring polarizabilities using optical methods, it is convenient to represent α in units of MHz/(V/cm)^2. The conversion from cgs units is $\alpha(\mathrm{cm}^3) = 5.95531 \times 10^{-16}\alpha[\mathrm{MHz}/(\mathrm{V/cm})^2]$

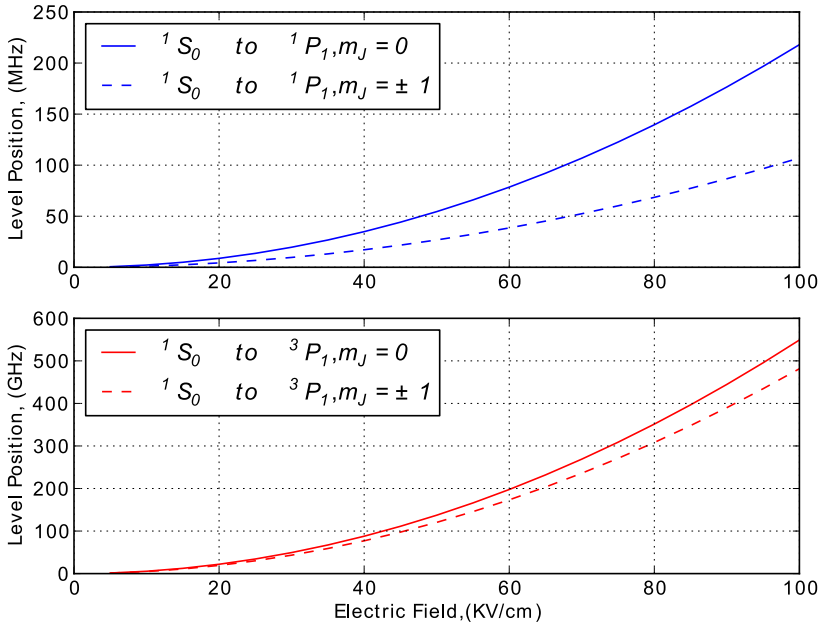

Figure 12.2: Calculated DC Stark Shift for 483nm and 714nm transitions as a function of applied electric field. Note the difference in scale of the vertical axes. The $^3P_1$ level is much more polarizable mainly because of its near degeneracy with the $^3D_2$ level.

12.1.2 Distinguishing between scalar and tensor contributions

In order to discriminate between $\alpha^{(0)}$ and $\alpha^{(2)}$, we propose to measure transitions in the odd isotope ^{225}Ra along side measurements on ^{226}Ra. This is because for ^{225}Ra, the differential polarizability for the transition $[^1\mathrm{S}_0, \mathrm{F} = 1/2 \rightarrow^1 \mathrm{P}_1, \mathrm{F} = 1/2]$ is purely due to the differential *scalar* polarizability of the two levels, whereas in ^{226}Ra, $[^1\mathrm{S}_0 \rightarrow^1 \mathrm{P}_1]$ has contributions from both $\alpha^{(0)}$ and $\alpha^{(2)}$. Likewise $[^1\mathrm{S}_0, \mathrm{F} = 1/2 \rightarrow^3 \mathrm{P}_1, \mathrm{F} = 1/2]$ has vanishing contributions from $\alpha^{(2)}$. The measurement in ^{225}Ra can therefore serve to isolate the scalar and tensor polarizability contributions on both transitions.

12.1.3 Experimental details

The differential DC Stark shifts will be measured by performing absorption spectroscopy on a sample of radium atoms trapped in a one-dimensional optical lattice that is located between a pair of electrodes. A schematic of the experimental arrangement is shown in figure 12.3. An optical lattice is a standing wave optical dipole trap (ODT). We will discuss ODTs in more depth in section 12.2. As a result of the lattice, the atoms contributing to the absorption signal will also experience an AC Stark shift. The AC Stark shift is however independent of the applied DC field and simply serves as a constant offset that can therefore be subtracted out.

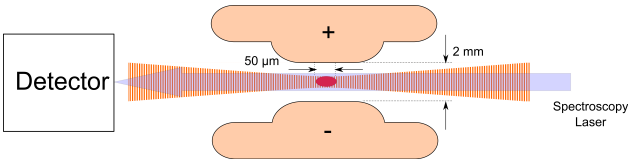

Figure 12.3: Schematic of atoms in optical lattice with radium atoms between high voltage electrodes. By applying ±10 kV on the electrodes, we can apply electric fields up to 100 kV/cm. We shall then measure the absorption spectra as a function of applied electric field.

In order to have the atoms situated in an optical lattice as shown in figure 12.3, we must perform a number of operations which are depicted in frames A to D of figure 12.4. Frame A depicts the accumulation of radium atoms in a MOT. At the same time, an optical lattice is constructed in the science chamber. Accumulating atoms in the MOT involves operating the apparatus in 'Loading Mode' as described in chapter 10. The duration of MOT loading depends on the MOT lifetime, as well as on the desired repetition rate of the experiment.

The next step, shown in frame B, is to transfer the radium atoms from the MOT into a traveling wave ODT (the bus-ODT), and to translate it, along with the atoms from the MOT to the 'science' chamber. We describe in section 12.3.1 our procedure for transferring atoms from the MOT to the ODT. This is typically a very fast operation which takes a few

hundred milliseconds. We report our studies of transporting atoms using the bus-ODT to the science chamber in section 12.3.3.

Once the atoms arrive at the science chamber, the bus-ODT is made to overlap with the optical lattice. We depict in frame C the 'hand-off' of atoms from the bus-ODT to the lattice. This is work that is currently underway. We envision using an optical molasses to provide the necessary cooling needed to transfer the radium atoms from one conservative potential to another.

Finally, the measurement-ready condition is shown in frame D, where the radium atoms are trapped in the optical lattice between a pair of electrodes. The measurement will involve absorption spectroscopy of the atoms by illuminating them with 714 nm and 483 nm light in order to determine the differential polarizabilities of the $7s^2 7s7p^1 S_0 - 7s7p^3 P_1$ and $7s^2 7s7p^1 S_0 - 7s7p^1 P_1$ levels respectively.

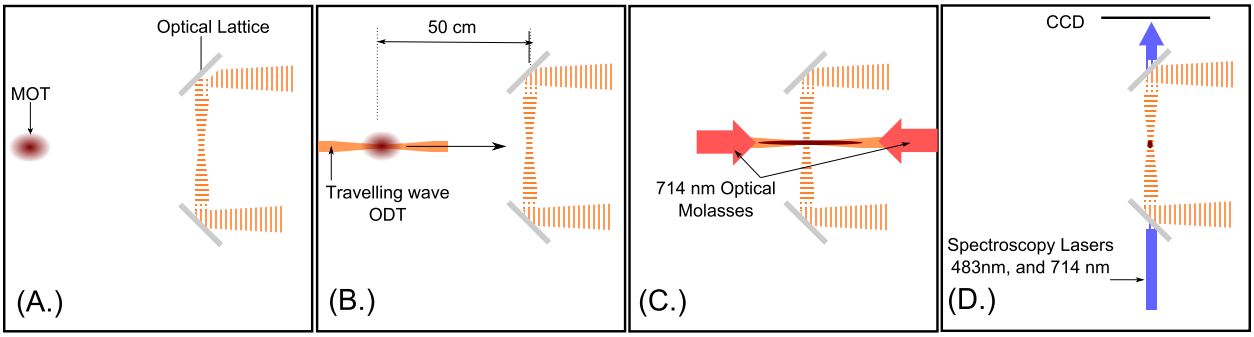

Figure 12.4: Sequence of steps for locating radium atoms in science chamber. In frame (A.) atoms are accumulated in a magneto-optical trap. (B.)The radium atoms are transferred into a traveling wave ODT. (C.) The traveling wave ODT is translated a distance of 50 cm to the science chamber, where it is overlapped with a one dimensional optical lattice. After effecting a 'hand-off' from the traveling wave trap to the optical lattice, the Bus ODT returns to the MOT to pick up the next shuttle of atoms. Absorption spectroscopy will then be performed on the sample of trapped atoms between the electrodes.

12.2 Optical dipole trapping of radium

As given in equations 12.2 to 12.5, the energy levels of an atom are perturbed in the presence of an AC electric field associated with a laser. We define a detuning $\Delta = \omega - \omega_0$, where ω is the frequency of the ODT laser, and ω_0 is the energy required to connect the ground state to the lowest lying excited state by an E1 transition.

The AC Stark shift of the ground state can be exploited such that it serves as a potential that can trap atoms if the electric field is engineered in a manner whereby there is a spatial dependence of the ground state shift that yields a restoring force in all three dimensions. Such a trap is referred to as a far off resonance trap (FORT) or an optical dipole trap (ODT). It can be formed by focusing a laser beam down to a spot. If the laser frequency is red detuned, i.e. $\Delta < 0$, the ground state atoms are attracted to the focus of the light, as that is where the electric field (and consequently AC Stark shift) is greatest. Similarly, if the laser frequency is blue detuned, the atoms will be repelled from the focus of the beam. Excellent reviews of applications of ODTs in different branches of physics are given in [75, 108].

Consider for example a Gaussian laser beam with power P_0 in Watts and wavelength λ that is focused down to a waist w_0, located at the point $z = 0$. The intensity profile of the focused light is[2]

$$|E(x,y,z)|^2 \propto \frac{E_0^2}{1+(\frac{z}{z_R})^2} \exp\left[-\frac{(x^2+y^2)}{w(z)^2}\right] \tag{12.8}$$

where E_0 is the maximum electric field, the spot radius at point z is $w(z)$, and Rayleigh length z_R are given by

$$\begin{aligned} w(z) &= w_0\sqrt{1+\frac{z}{z_R}} \\ z_R &= \frac{\pi w_0^2}{\lambda}. \end{aligned} \tag{12.9}$$

2. For a Gaussian laser beam with power P_0 and intensity profile $I(r,z) = I_0 \exp[-2r^2/w(z)^2]$, the peak intensity $I_0 = 2P_0/\pi w_0^2$, and the peak electric field is $|E_0|^2 = 4P_0/\varepsilon_0 c w_0^2$

From equation 12.3, the electric field induces a dipole moment $\mathbf{p} = \alpha_0 \mathbf{E}$. The interaction potential between the induced dipole and the electric field of the laser is given by

$$U_{dip} = -\frac{1}{2} \langle \mathbf{d} \cdot \mathbf{E} \rangle \tag{12.10}$$

where the factor of $1/2$ is due to the fact that the dipole is induced, and we take the time average of the electric field–picking up an additional factor of $1/2$. Consequently, the potential due to an ODT formed by a Gaussian beam is

$$U_{ODT}(x, y, z) = -\frac{U_0}{(1 + (\frac{z}{z_R})^2)} \exp\left[-\frac{x^2 + y^2}{w(z)^2}\right] \tag{12.11}$$

where $U_0 = -\frac{1}{4}\alpha E_0^2$. We note that equation 12.11 has cylindrical symmetry, and so, setting $r^2 = x^2 + y^2$ and expanding 12.11 for small values of z/z_R and r/w_0, we get

$$U_{ODT}(r, z, \phi) \approx -U_0 + \frac{U_0}{z_R^2} z^2 + \frac{2U_0}{w_0^2} r^2 = -U_0 + \frac{1}{2} M \omega_z^2 z^2 + \frac{1}{2} M \omega_r^2 z^2 \tag{12.12}$$

That is, near the trap minimum, the trap is harmonic and is characterized by a longitudinal frequency $\omega_z = \sqrt{2U_0/m z_R^2}$ and a radial frequency $\omega_r = \sqrt{4U_0/m w_0^2}$. For atoms in a harmonic potential at a temperature T, the phase-space distribution of the atoms is given by the expression

$$W(\mathbf{x}, \mathbf{p}) \propto \frac{n(\mathbf{x})}{(2\pi M k_B T)^{3/2}} \exp\left[\frac{H(\mathbf{x}, \mathbf{p})}{k_B T}\right] \tag{12.13}$$

where $H(\mathbf{x}, \mathbf{p}) = p^2/2M + U(\mathbf{x})$. The spatial distribution can be obtained from integrating over the momentum to get

$$n(\mathbf{x}) = \int W(\mathbf{x}, \mathbf{p})\, d^3 p. \tag{12.14}$$

Using 12.12 for $U(\mathbf{x})$, we obtain

$$\begin{aligned} n(\mathbf{r},\mathbf{z}) &\propto \exp - \left[\frac{r^2}{\sigma_r^2} + \frac{z^2}{\sigma_z^2}\right] \\ \sigma_i^2 &= \frac{k_B T}{2 M w_i^2} \end{aligned} \tag{12.15}$$

which is basically a Gaussian distribution of the position along either axis with widths σ_r and σ_z. Likewise the spread of velocities is given by:

$$n(\mathbf{p}) = \int W(\mathbf{x},\mathbf{p})\, d^3x. \tag{12.16}$$

which also yields a Gaussian distribution,

$$\begin{aligned} n(\mathbf{v}) &\propto \exp\left[-\frac{\mathbf{v^2}}{2\sigma_v^2}\right] \\ \sigma_v^2 &= \sqrt{\frac{k_B T}{M}} \end{aligned} \tag{12.17}$$

12.2.1 Scattering rate calculation for non-resonant light

If atoms are held in the focus of a laser beam, one obvious concern is that the atoms will scatter the photons from the laser forming the ODT, and hence be heated out of the trap. In order to quantify this, we consider the treatment in [140], where for small population of the excited state, the scattering rate is given by the Kramers-Heisenberg formula.

$$\Gamma_{i\to f} = \frac{\alpha^2 w^3 E_0^2}{3\hbar c} \left| \sum_{e,\epsilon} \frac{\langle f| \boldsymbol{\epsilon}_{\boldsymbol{r}}^* \cdot \boldsymbol{r} |e\rangle \langle e| \boldsymbol{\epsilon}_{\boldsymbol{r}}^* \cdot \boldsymbol{r} |i\rangle}{w_e - w} + \frac{\langle f| \boldsymbol{\epsilon}_{\boldsymbol{r}}^* \cdot \boldsymbol{r} |e\rangle \langle e| \boldsymbol{\epsilon}_{\boldsymbol{r}}^* \cdot \boldsymbol{r} |i\rangle}{w_e + w} \right|^2 \tag{12.18}$$

with ϵ_r the polarization of the radiated light. The expression in equation 12.18 describes both the Rayleigh scattering rate $i \to i$ and the Raman scattering rate, where $i \to f$, with

$i \neq f$. The Raman scattering rate leads to spin depolarization [140]. This is particularly important in an EDM measurement, as the observable is the spin precession frequency, and spin-depolarization leads to a loss of signal contrast.

Working in the far off resonance regime where $|\Delta| \ll w$, equations 12.3, 12.4 and 12.18 lead to the observation that while the dipole potential scales as I/Δ, the scattering rate goes as I/Δ^2. Consequently, it is desirable to use high intensities and large detunings in order to keep the potential deep and the scattering rate low.

12.3 Experimental results

We implement an ODT for radium atoms using a 1550 nm laser. At 1550 nm, the AC polarizability of the ground state of radium is calculated to be $\alpha_0 = 3.21 \times 10^{-23}\text{cm}^3$ This means that with 40 W of light focused to a waist of 50 μm, the ODT has a depth of ~ 540 μK. A particularly attractive property of 1550 nm is that the differential polarizability of the $^1S_0$ and $^3P_1$ levels is vanishingly small. In other words, 1550 nm is a near 'magic' wavelength for the 714 nm transition in radium atoms. As we will discuss below, this feature aids significantly in effecting a transfer of atoms from the MOT to the ODT. We will described below our studies of loading an ODT from a MOT, and will follow that with a report of our studies of transporting atoms by moving the ODT.

Because radium is rather heavy, and the trapping ODT potential is quite shallow, the correction of the trapping potential due to gravity is non-negligible.

$$U_{trap}(x, y, z) = U_{ODT}(x, y, z) + mg[x\cos(\theta) + z\sin(\theta)] \tag{12.19}$$

where θ is the angle that the ODT axis forms with the direction of gravity. We show in figure 12.5 the way the trapping potential is perturbed by gravity with $\theta = 90°$. Because

Table 12.2: Trapping parameters for ^{226}Ra in 1550 nm bus-ODT. We use the value $\alpha_0 = 3.21 \times 10^{-23}$ cm^3 for the radium ground state polarizability.

Parameter		Magnitude
Detuning from $7s7p^3P_1$	Δ	1.4×10^{15} Hz
Power	P_0	40 W
Waist	w_0	50 μm
Rayleigh length	Z_R	5 mm
Trap depth	U_0	540 μK
Recoil temperature	T_{rec}	34 nK
Rayleigh scattering rate	Γ_{1550}	5×10^{-1} s^{-1}
Raman scattering rate	$\Gamma_{i\to f}$	5×10^{-6} s^{-1}
Axial trap frequency	$\omega_z/2\pi$	5.5 Hz
Radial trap frequency	$\omega_r/2\pi$	900 Hz

of this, the ODT must be aligned perpendicular to the direction of gravity to a very good degree. In order to achieve less than 1 mrad alignment perpendicular to gravity, we make use of a laser leveler. We align the ODT laser to be parallel to the light from the leveler and therefore transfer the levelness.

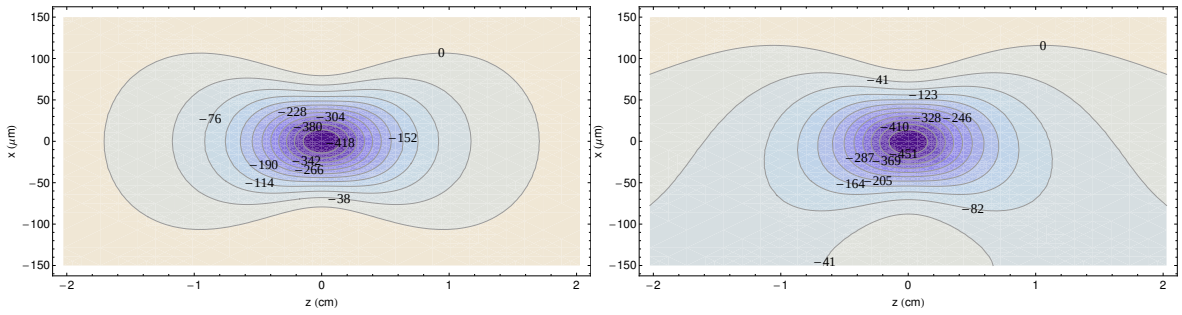

Figure 12.5: Contour plots of the ODT potential in μK. The parameters of the trap are given in table 12.2. The left panel shows the potential sampled by the atoms with no gravity, while the right panel includes the effect of gravity. In the figures, the laser is propagating along the z direction, and is focused at the origin z = 0.

12.3.1 Loading ODT from MOT

The necessary conditions for an efficient transfer of atoms from a MOT to a (conservative) ODT are (1.) large phase space overlap between the MOT and ODT potential, and (2.) the presence of an energy dissipation mechanism. We consider these two conditions below. Thorough studies of MOT to ODT transfer have been published by [98, 118, 157] and references therein.

We say that there is a large phase space overlap between the MOT and ODT when the position and momentum distribution of the atoms in the MOT closely matches the trapping potential of the ODT. While the MOT is roughly spherical in shape with a typical radius on the order of a millimeter, the ODT has a more cylindrical shape—with a diameter of ~ 100 μm and a length of ~ 2 cm. In order to maximize the spatial overlap of the MOT and ODT, we compress the volume of the MOT around the position of the ODT beam. We achieve this by ramping up the gradient of the magnetic fields used for the MOT. An example of the compression achieved was shown in figure 10.10. While this is desirable for optimal overlap with the ODT, it is not so good for achieving an efficient loading of the MOT. But, because our experiment cycles between a 'loading' phase and a 'probing' phase, we are able to optimize both.

As shown in figure 12.5, the ODT formed with parameters given in table 12.2 has a depth of ~ 540 μK. A large momentum overlap is therefore obtained from atoms which are colder than the trapping potential. The measured temperatures of atoms in the radium MOTs we constructed are $T \sim 40 \mu K$.

The presence of an energy dissipation mechanism is necessary for transfer into the ODT because the ODT potential is conservative, and the atoms that 'fall' into the ODT potential will have enough kinetic energy to escape from the well. In order to trap them, some of that kinetic energy must be dissipated while they are in the trap. One way to dissipate this

is collisionally. If the density of atoms is high enough, radium-radium collisions will lead to a loss of energy for some of the atoms allowing them to be bound. More conventionally though, laser cooling is used to dissipate energy, while the atoms are in the ODT potential. Recall that the atoms in the MOT are in a 3D optical molasses. When subjected to the ODT beam, the operating frequency of the molasses is shifted by virtue of the differential AC stark shift of the levels in the transition used for the molasses. In order to maintain the operation of the molasses, one must compensate for this differential AC stark shift. One technique is to temporally chop the ODT beam off and on at a frequency which is high compared to the trap frequency. This means that the atoms will be cooled for one half of the chopping cycle and not cooled during the other half when the ODT is on. This scheme was used for example in trapping rubidium atoms [109]. As noted above, 1550 nm is to a very good approximation a 'magic' wavelength for the 714 nm transition used for optical molasses. The molasses which supports the atoms in the MOT is therefore also very efficient at cooling the atoms which are in the ODT. We show in figure 12.6 an image of the atoms in the combined MOT plus ODT potentials.

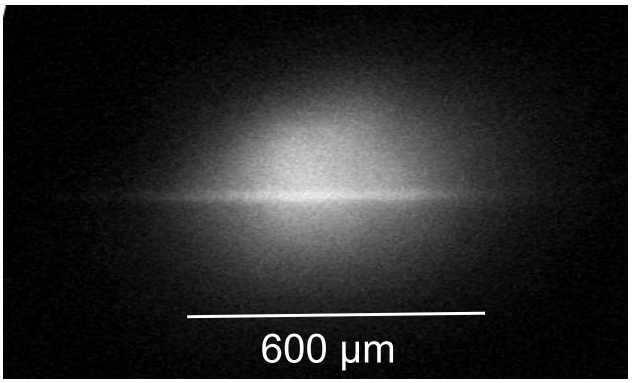

Figure 12.6: Image of Atoms confined in a combination MOT and Dipole trap.

We show a schematic of the timing which we use in transferring atoms for our experiments in figure 12.7.After loading the MOT for a time interval t_{load}, we switch the MOT to 'probing'

mode for an interval t_{probe} during which we take an image of the atoms in the trap. This is to establish the "pre-drop" value. Thereafter, we operate in cooling mode for a duration t_{cool}. To demonstrate that the atoms are indeed transferred, we 'drop' the MOT by shuttering the molasses beams for some time interval t_{drop}. After that time interval elapses, we revert to the probing mode where we recapture the atoms into the MOT and once again take an image of the trapped atoms. The ratio of the number of atoms in the two images is dependent on the initial transfer efficiency, as well as on the lifetime of the ODT. By varying the duration of t_{drop}, we can independently extract both the lifetime and the transfer efficiency. We show some ODT lifetime measurements in figure 12.8.

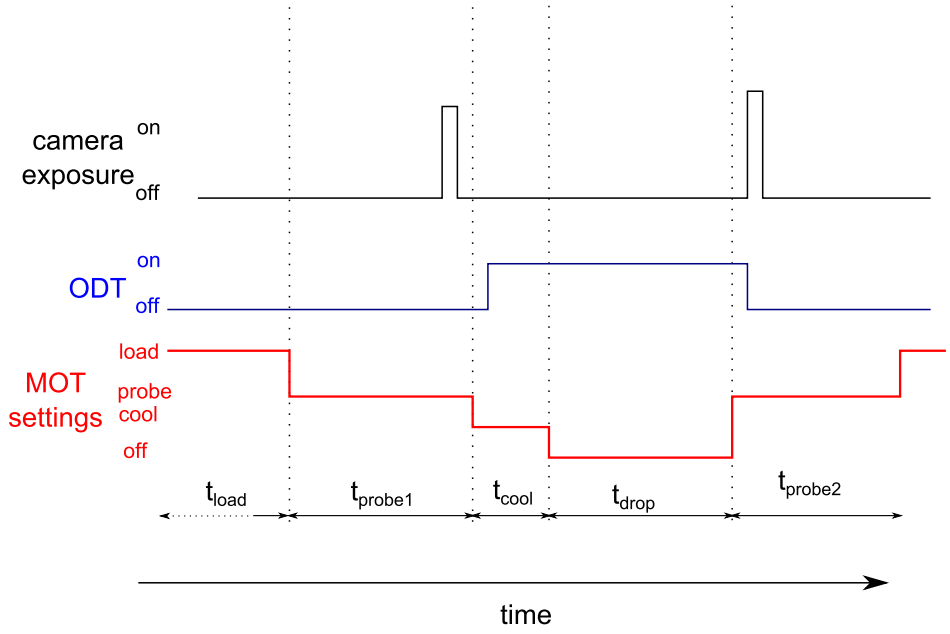

Figure 12.7: Timing Scheme for transferring atoms from MOT to ODT. During the drop phase, the light which forms the molasses is shuttered. The intensities and detunings of the 714 nm light as well as the magnitudes of the magnetic field gradients during the different operating modes are given in table 10.4.2

We determining ODT lifetimes by performing an experiment with a timing scheme given in figure 12.7—varying the drop time t_{drop}. In figure 12.8, we show the measurements of the

ODT lifetime for three different values of the ODT depth which we adjusted by adjusting the intensity of the ODT laser. We note that the MOT to ODT transfer efficiency, given by the y intercept of the exponential decay, is strongly dependent on the depth of the ODT. However, the 1/e lifetime of the trap is roughly constant for all the depths at approximately 7 seconds.

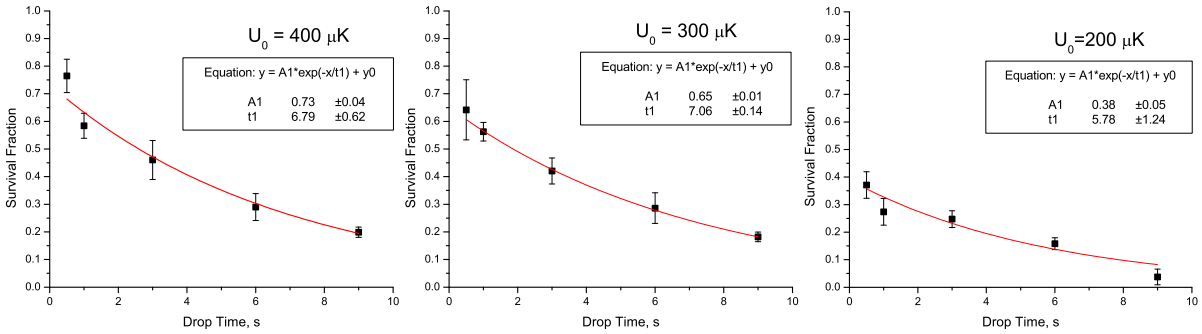

Figure 12.8: ODT lifetime measurement. The top panel shows the timing set for the experiment. The survival fraction plotted below is obtained from the ratio of the number of atoms in the pre-drop and post drop images.

12.3.2 Heating Mechanisms

As shown in figure 12.8, the lifetimes of the atoms in the ODT are on the order of 7 seconds. Heating mechanisms that could limit the trap lifetime are off-resonance excitation by 1550 nm photons, intensity and pointing noise of the ODT laser, and collisions with background gas.

We estimate the rate of heating due to Rayleigh scattering of the off resonant 1550 nm light to be $\Gamma_{1550}\ T_{\rm rec}$, where $T_{\rm rec} = 0.04\mu K$ is the recoil temperature of a scattered 1550 nm photon. This yields a heating timescale necessary for escaping the trap on the order 10^3 s, which is much longer than the 7 seconds we observe. Also, we measured the intensity and pointing noise spectrum of our setup. Using an analysis given by [118], we are able

to estimate the timescale for heating out of the trap due to intensity and pointing noise to correspond to a couple hundred seconds. Moreover, the ODT lifetime limit due to pointing noise should scale inversely with the depth of the ODT. We show in figure 12.8 that the ODT lifetimes are independent of the depth of the ODT. We therefore conclude that neither pointing/intensity noise, nor off resonant excitation are responsible for the observed 7 second lifetime.

We are left with the option of collisions with background gas. At a measured pressure of 1×10^{-9} Torr, the 7 second lifetime follows the 'rule of thumb' observed by other experimenters reported in [75].

12.3.3 Transport of atoms using moving ODT

Once the atoms are successfully transferred from the MOT to the ODT, we need to move them to the science region. We do so by translating the lens which is used to focus the light forming the ODT. The atoms which are trapped at the focus are consequently moved along. We make use of an air bearing translation stage from Aerotech (Aerotech ABL2000 series) in order to move the lens smoothly. It has a total travel of 1.1 meters and has a programmable translation profile. The profile of the velocity, acceleration and jerk employed during the motion is important, and affects the efficiency with which the atoms can be moved. Experiments which have implemented a similar scheme to transfer of atoms are reported in [78, 44]. For the DC Stark shift measurements we discuss, we need to translate the atoms $\sim$ 0.5 m. For the permanent EDM measurements proposed in section 9.2, we plan on moving the atoms a distance of 1 m. To our knowledge, we are the first group to attempt to move atoms using a moving ODT a distance greater than 30 cm.

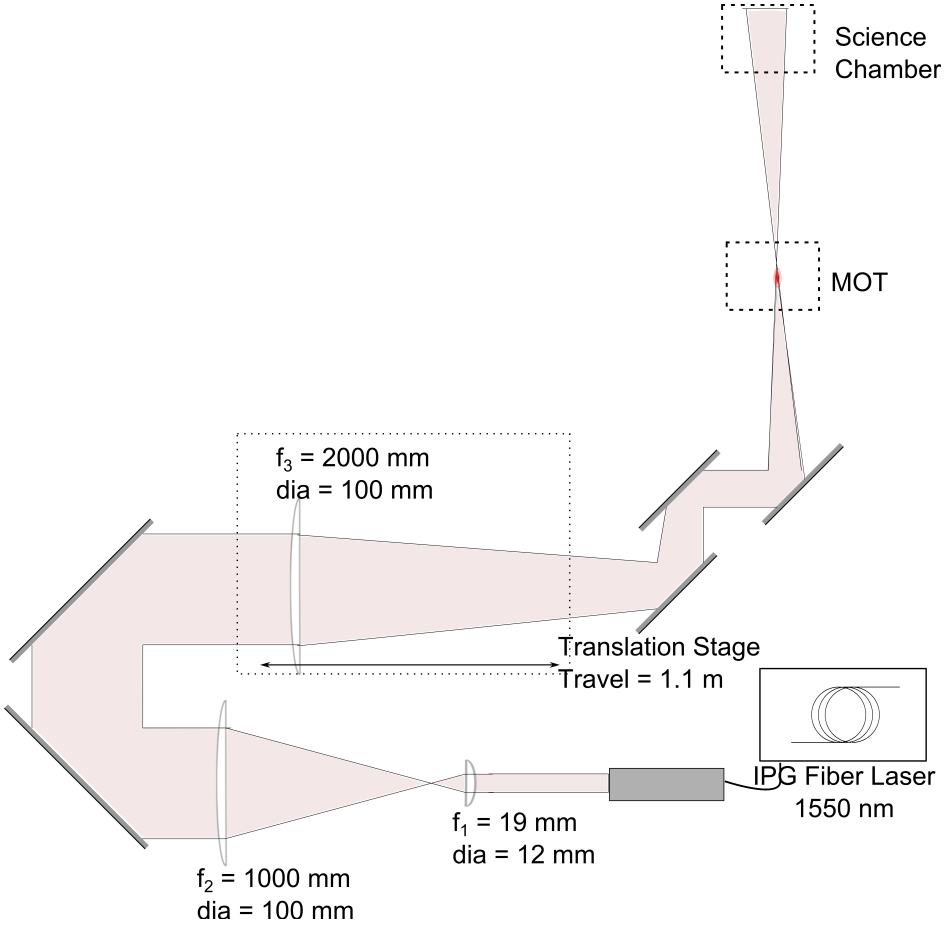

Figure 12.9: Setup of optics for bus-ODT. The emerging beam from the fiber laser launcher is magnified by a single telescope formed by lenses 1 and 2 with focal lengths f_1 and f_2 respectively. It is then focused by a final lens with focal length f3 = 2000 mm. By translating lens 3, we can move the position of the focus from the MOT to the'science chamber

Consider the time dependent ODT potential along the z axis.

$$U(z,t) = \frac{U_0}{1 + ((z - z_0(t))/z_R)^2} \tag{12.20}$$

The time dependence comes from the fact that the focus of the light forming the ODT is being moved with a displacement profile $z_0(t)$. The velocity, acceleration and jerk of the motion are then $\dot{z}_0(t)$, $\ddot{z}_0(t)$, and $\dddot{z}_0(t)$ respectively. We have studied the following motion

profiles to determine the most efficient one for transferring atoms from the MOT to the science chamber.

(i.) **Sine Wave** In this profile, the displacement, and higher derivatives are all sinusoidal functions of time.

(ii.) **Triangle Wave**, In this profile, the displacement is a linear function of time and so there is consequently a constant velocity during the motion. Because the motion abruptly starts and stops, there are spikes of acceleration at the beginning and end of the motion.

(iii.) **Parabolic Wave** This profile involves moving with a constant acceleration to the midway of the trip, and then constantly decelerating on the second half. The net result of this is that but for the star, mid-way point, and end of the motion, the atoms do not experience any jerk. At those three points however, there is a rather large jerk.

(iv.) **Minimal Jerk**. The minimal jerk motion is similar to the parabolic wave. However, it is piecewise defined, such that the acceleration is a smooth function of time, and the magnitude of the jerk is minimized

Representative measurements of the velocity and acceleration for the different profiles are given in figure 12.10.

In order to determine the efficiency with which the atoms are being moved from one point to another, we measured the fraction of atoms that survived after the trap was moved a certain distance and back. We did so by using a timing scheme as depicted in figure 12.7. During the time the MOT was dropped, the translation stage was moved a desired distance with a given motion profile. The ratio of the number of atoms detected before and after the trip was indicative of efficiency of transport—after a correction was made for the trap lifetime. It is important that the motion be initiated when the MOT is dropped. Otherwise,

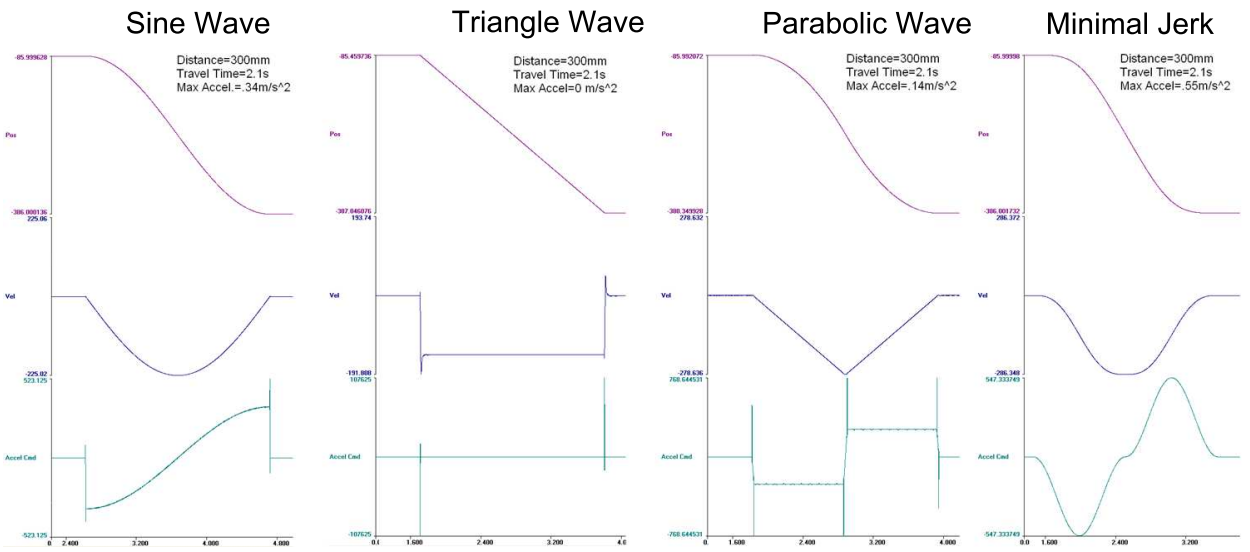

Figure 12.10: Motion profiles used for moving atoms from MOT to ODT. The top graph shows the position as a function of time, the middle graph shows velocity, while the lower graph shows the acceleration profile.

the atoms will not be carried along, as the force due to the molasses is stronger than that due to the ODT along the weak axis, along which the atoms are moved.

We observed that the sinusoidal motion profile was the most efficient of the four that we tried. In effect, the ODT is moved along a sinusoidal path.

$$z_0(t) = \mathrm{Z_{max}}\ \sin(\tilde{\omega}\, t - \tilde{\phi}). \tag{12.21}$$

where $\tilde{\omega} = \pi/T_0$, and $\tilde{\phi} = \pi/4$ with T_0 being the time required to to go from 0 to the maximum displacement $\mathrm{Z_{max}}$.

The profile of the sinusoidal displacement, velocity and acceleration are shown in figure 12.12. In terms of the maximum displacement $\mathrm{Z_{max}}$,

$$\begin{aligned} \mathrm{V_{max}} &= \tilde{\omega}\mathrm{Z_{max}} \\ \mathrm{a_{max}} &= \tilde{\omega}^2\mathrm{Z_{max}} \end{aligned} \tag{12.22}$$

Regardless of the distance traversed, we observed that the survival fraction was determined almost exclusively by the average velocity of the trap. The survival fraction had a form as shown in figure 12.11.

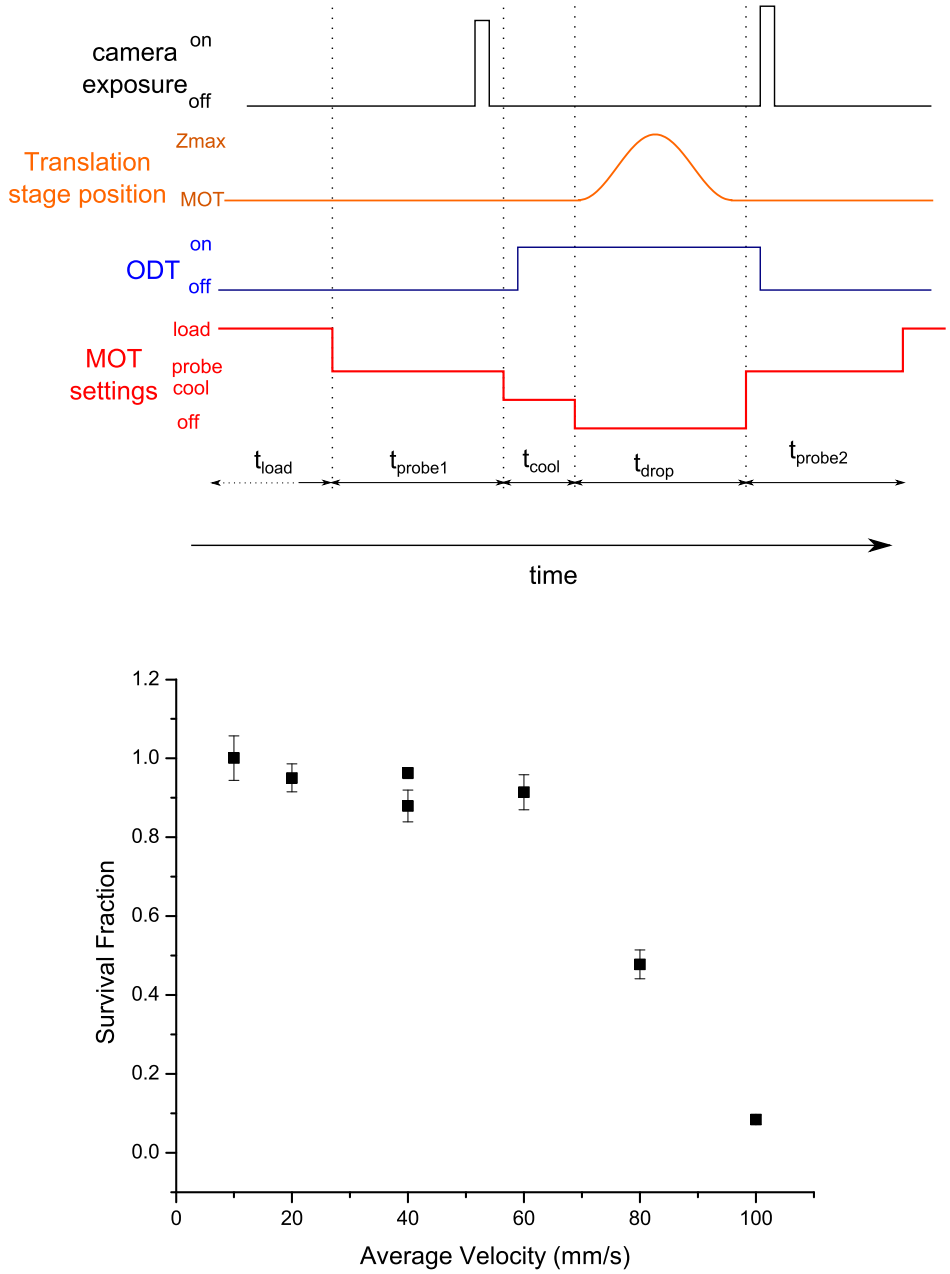

Figure 12.11: Normalized transport efficiencies. The survival fraction was obtained by determining the ratio of the MOT size before and after the round trip.

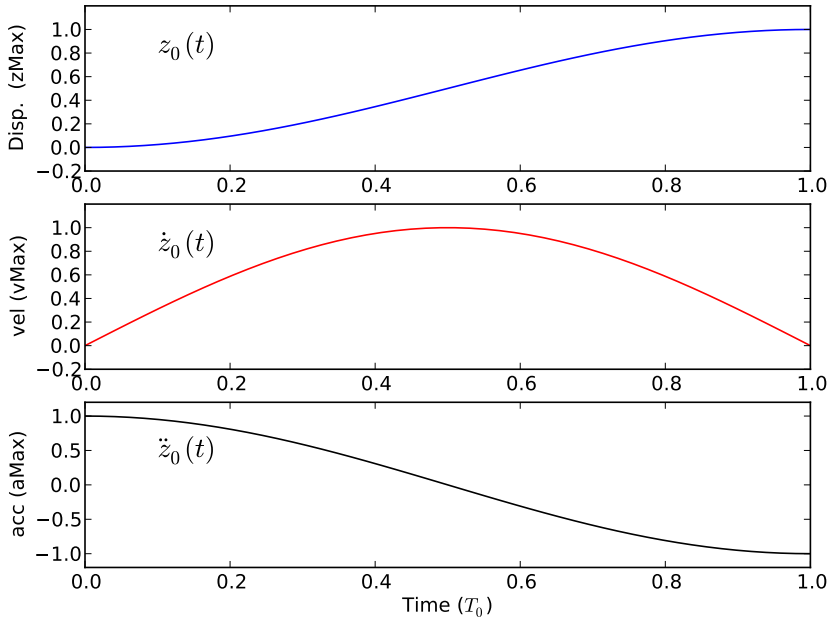

Figure 12.12: Trap motion profiles, in terms of the maximum displacement zMax T_0 is time to go from the start position to the maximum of the motion.

APPENDIX A

TEMPERATURE MEASUREMENT OF TRAPPED RADIUM ATOMS

We determine the temperature of the radium MOT using a time of flight method. We derive below the time of flight signal for a cloud of atoms with a temperature T–following very closely the treatment in [33]. The basic idea of the TOF temperature determination is that the velocity distribution of a cloud with a temperature T has a phase space distribution given by

$$\mathcal{W}(\mathbf{r},\mathbf{v}) = \prod_{i\in\{x,y,z\}} g(i_0,\sigma_0)\; g(v_{i0},\sigma_v) \tag{A.1}$$

where

$$g(x,\sigma) = \sqrt{\frac{1}{2\pi\sigma^2}}\mathrm{Exp}[-\frac{\mathrm{x}^2}{2\sigma^2}]. \tag{A.2}$$

That is, both the spatial and velocity distributions are characterized by Gaussian, with widths σ_i and σ_v respectively. If the sample is isotropic, then $\sigma_x = \sigma_y = \sigma_z$. Likewise, for σ_v. We also have that the temperature in a particular direction is given by

$$T = \frac{M}{k_B}\sigma_v \tag{A.3}$$

When a sample of trapped atoms with this initial distribution is dropped, the atoms will expand freely in two dimensions and fall under the influence of gravity in the other dimension. We then have that after some time interval t, the mean velocities are given by

$$v_{x0} = \frac{x-x_0}{t} - \frac{1}{2}gt, \qquad v_{y0} = \frac{y-y_0}{t}, \qquad v_{z0} = \frac{z-z_0}{t}. \tag{A.4}$$

which yields a phase space distribution

$$\begin{aligned} \mathcal{W}(x,y,z,t) &= g(x - gt^2/s, \sigma_t) g(y, \sigma_t) g(z, \sigma_t) \\ \sigma_t &= \sqrt{\sigma_0^2 + \sigma_v^2 t^2} \end{aligned} \tag{A.5}$$

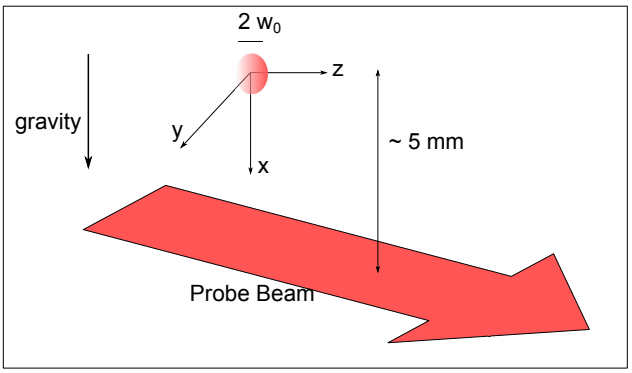

Figure A.1: Setup for experiment to perform a Time of Flight Temperature measurement.

Now consider the probe beam on to which the atoms are dropped. We assume here a Gaussian probe beam characterized by widths σ_{Ix} and σ_{Iy}, located a distance $\tilde{x} = 1/2\ gt_0^2$ from the initial position of the cloud. Then, the intensity distribution of the probe laser beam is given by

$$\mathcal{I}(x,y) = P_0\ g(x - \tilde{x}, \sigma_{Ix})\ g(y, \sigma_{Iy}) \tag{A.6}$$

We can then evaluate $N(t)$, the number of atoms which pass through the probe beam as a function of time from the expression

$$\begin{aligned} N(t) &= \int \int_{-\infty}^{\infty} \int \mathcal{I}(x,y)\ \mathcal{W}(x,y,z,t)\ dx\ dy\ dz \\ &= \frac{P_0}{2\pi\sqrt{(\sigma_{Ix}^2 + \sigma_t^2)(\sigma_{Iy}^2 + \sigma_t^2)}}\ \mathrm{Exp}\left[- \left(\frac{\mathrm{g}(\mathrm{t}_0^2 - \mathrm{t}^2)}{2\sqrt{2}\sqrt{\sigma_{\mathrm{Ix}}^2 + \sigma_{\mathrm{t}}^2}} - \right) \right] \end{aligned} \tag{A.7}$$

In the limit in which $\sigma_{Ix} << \sigma_t$, and $\sigma_{Iy} \to \infty$, equation A.7 reduces to

$$N(t) = \frac{P_0}{2\pi\sigma_v^2 t_0^2} \text{Exp}\left[-\left(\frac{\text{g}(\text{t}^2 - \text{t}_0^2)}{2\sqrt{2}\sigma_\text{t}}\right)^2\right] \tag{A.8}$$

Our temperature determination then simply depends on dropping the atoms, and fitting the time of flight fluorescence to equation A.8. In measuring the temperature, we setup a timing scheme whereby atoms were first accumulated in the MOT. Thereafter, the light going to the MOT was shuttered with a mechanical shutter. At the same time, the light comprising the probe beam was turned on a distance $\tilde{x} \sim 5$ mm below the MOT. Our probe beam was generated by on resonance 714 nm light, which was focused in the z direction ($\sigma_{Ix} \sim 100\mu$ m but expanded in the y direction ($\sigma_{Iy} \sim 300$ mm. We made use of the same imaging optics used to detect the MOT in detecting the TOF fluorescence. It these experiments, it was extremely important that we had very low backgrounds, as the interaction time between the atoms and the light is so short (few ms), and our collection efficiency was sub optimal. In order to get a signal with sufficient signal to noise to fit, we integrated for time intervals on the order of 20 minutes in order to obtain a TOF signal as shown in A.

We obtained minimum temperatures between 40 μK and 50 μK. We studied the dependence on the the intensity and detuning of the molasses. There is gross agreement, in particular with the intensity dependence. Some of the systematic temperature trends we observed are shown in figure A. Recall that from Doppler cooling theory, the Doppler temperature for a sample of atoms in an optical molasses made of 714 nm light is $T_D \sim 10\mu K$. For our radium MOT, our measured temperatures have consistently been higher. We suspect that this might partly be due to the fact that our 714 nm laser has a rather large linewidth of a few hundred kHz.

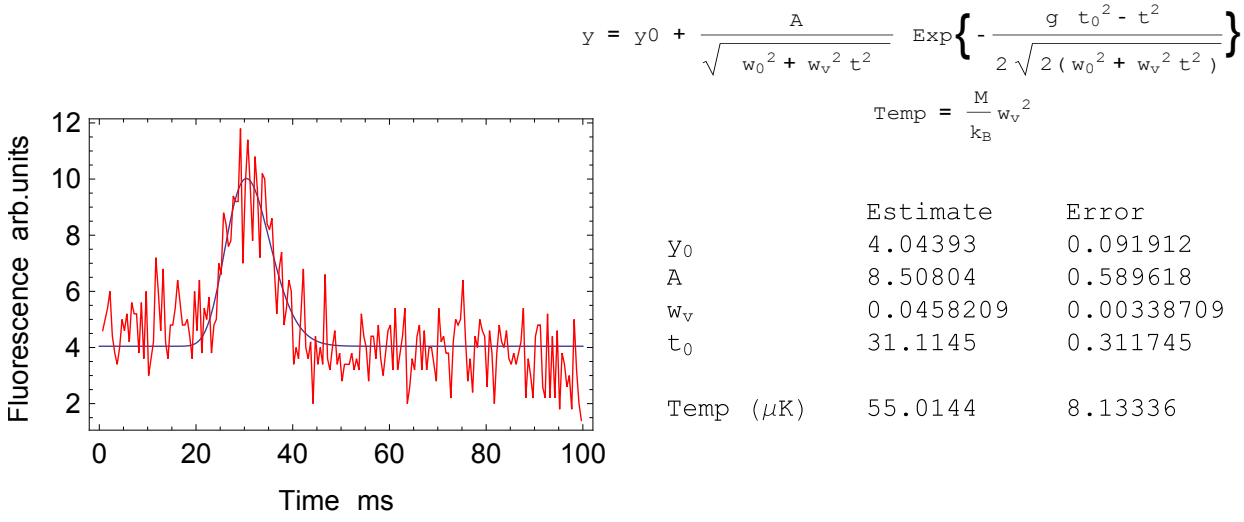

	Estimate	Error
y_0	4.04393	0.091912
A	8.50804	0.589618
w_v	0.0458209	0.00338709
t_0	31.1145	0.311745
Temp (μK)	55.0144	8.13336

Figure A.2: Data from a Time of flight determination of the temperature

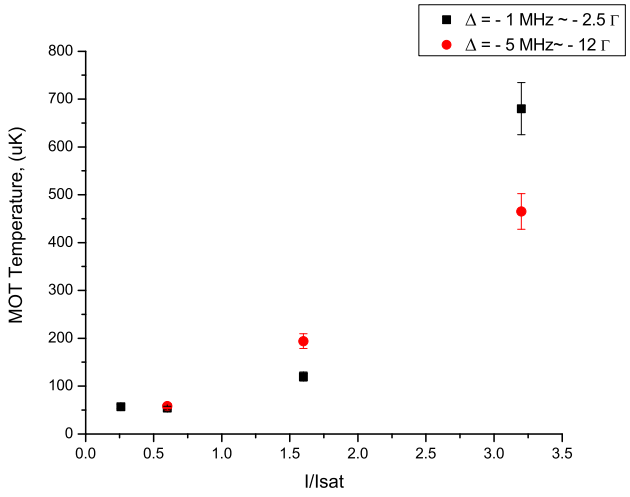

Figure A.3: Dependence of the MOT temperature with the intensity of the cooling light. We noticed a minimum temperature of 50 $\sim \mu K$ for the MOT temperature. This was obtained for weak probe intensities $\sim 0.2 I_{sat}$, and detuning.

REFERENCES

[1] I Ahmad and P. A Butler. Octupole Shapes in Nulei. *Annual Review of Nulear and Particle Science*, 43:71–116, 1993.

[2] SA Ahmad, W. Klempt, R. Neugart, EW Otten, P.G. Reinhard, G. Ulm, and K. Wendt. Mean square charge radii of radium isotopes and octupole deformation in the 220-228 Ra region. *Nuclear Physics A*, 483(2):244–268, 1988.

[3] SA Ahmad, W. Klempt, R. Neugart, EW Otten, K. Wendt, and C. Ekström. Determination of nuclear spins and moments in a series of radium isotopes. *Physics Letters B*, 133(1-2):47–52, 1983.

[4] Jim Al-Khalili. An introduction to halo nuclei. *Lect. Notes Phys.*, 651:77, 2004.

[5] G. D. Alkhazov et al. Nuclear matter distributions in ^{6}He and ^{8}He from small angle p-He scattering in inverse kinematics at intermediate energy. *Phys. Rev. Lett.*, 78(12):2313–2316, Mar 1997.

[6] Claire S. Allred, Jason Reeves, Christopher Corder, and Harold Metcalf. Atom lithography with metastable helium. *Journal of Applied Physics*, 107(3):033116, 2010.

[7] Altarev, I. et al. New constraints on lorentz invariance violation from the neutron electric dipole moment. *EPL*, 92(5):51001, 2010.

[8] A. Amroun, V. Breton, J. M. Cavedon, B. Frois, D. Goutte, F. P. Juster, Ph. Leconte, J. Martino, Y. Mizuno, X. H. Phan, S. K. Platchkov, I. Sick, and S. Williamson. ^{3}H and ^{3}He electromagnetic form factors. *Nuclear Physics A*, 579(3-4):596 – 626, 1994.

[9] J. R. P. Angel and P. G. H. Sandars. The hyperfine structure stark effect i. theory. *Proceedings of the Royal Society A*, 305, 1968.

[10] A. Antognini et al. Illuminating the proton radius conundrum: the μHe$^+$ lamb shift. *Canadian Journal of Physics*, 89(1):47–57, 2011.

[11] G. Audi, O. Bersillon, J. Blachot, and A. H. Wapstra. The evaluation of nuclear and decay properties. *Nuclear Physics A*, 729(1):3 – 128, 2003. The 2003 NUBASE and Atomic Mass Evaluations.

[12] G. Audi, A. H. Wapstra, and C. Thibault. The 2003 atomic mass evaluation: (ii). tables, graphs and references. *Nuclear Physics A*, 729(1):337 – 676, 2003. The 2003 NUBASE and Atomic Mass Evaluations.

[13] N. Auerbach, V. V. Flambaum, and V. Spevak. Collective t- and p-odd electromagnetic moments in nuclei with octupole deformations. *Phys. Rev. Lett.*, 76(23):4316–4319, Jun 1996.

[14] Naftali Auerbach and Vladimir Zelevinsky. Nuclear structure and the search for collective enhancement of P,T -violating schiff moments. *Journal of Physics G: Nuclear and Particle Physics*, 35(9):093101, 2008.

[15] C. A. Baker, D. D. Doyle, P. Geltenbort, K. Green, M. G. D. van der Grinten, P. G. Harris, P. Iaydjiev, S. N. Ivanov, D. J. R. May, J. M. Pendlebury, J. D. Richardson, D. Shiers, and K. F. Smith. Improved experimental limit on the electric dipole moment of the neutron. *Phys. Rev. Lett.*, 97:131801, Sep 2006.

[16] C. A. Baker, D. D. Doyle, P. Geltenbort, K. Green, M. G. D. van der Grinten, P. G. Harris, P. Iaydjiev, S. N. Ivanov, D. J. R. May, J. M. Pendlebury, J. D. Richardson, D. Shiers, and K. F. Smith. Improved experimental limit on the electric dipole moment of the neutron. *Phys. Rev. Lett.*, 97(13):131801, Sep 2006.

[17] H. A. Bethe and E. E. Salpeter. *Quantum mechanics of one and two electon atoms*. Plenum Publishing company, 1977.

[18] J. Bieroń. MCDHF calculations of the hyperfine structures of radium. *Journal of Physics B: Atomic, Molecular and Optical Physics*, 38:2221–2228, 2005.

[19] J. Bieron. Multiconfiguration dirac-hartree-fock calculations of the hyperfine structures of radium. *Jounal of Physics B: Atomic Molecular Optical Physics*, 38, 2005.

[20] J. Bieron, C. F. Fischer, S. Fritzsche, and K. Pachucki. Lifetime and hyperfine structure of the ^{3}D$_2$ state of radium. *Jounal of Physics B: Atomic Molecular Optical Physics*, 37, 2004.

[21] J. Bieron, C.F. Fischer, S. Fritzsche, and K. Pachucki. Lifetime and hyperfine structure of the $^3D_2$ state of radium. *Journal of Physics B: Atomic, Molecular and Optical Physics*, 37(17):L305–L311, 2004.

[22] J. Bieroń, P. Indelicato, and P. Jönsson. Multiconfiguration Dirac-Hartree-Fock calculations of transition rates and lifetimes of the eight lowest excited levels of radium. *The European Physical Journal-Special Topics*, 144(1):75–84, 2007.

[23] J. Bieron, P. Indelicato, and P. Jonsson. Multiconfiguration dirac-hartree-fock calculations of transition rates and lifetimes of the eight lowest excited levels of radium. *The European Physical Journal-Special Topics*, 144, 2007.

[24] I. I. Bigi and A. I. Sanda. *CP Violation*. Cambridge University Press, 2000.

[25] L. A Bloomfield, B. Couillaud, Ph. Dabkiewicz, H. Gerhardt, and T. W. Hänsch. Hyperfine structure of the $2^3S - 5^3P$ transition in ^{3}He by high-resolution uv-laser spectroscopy. *Phys. Rev. A*, 26:713–716, Jul 1982.

[26] Edward Blucher, Bruce Winstein, and Taku Yamanaka. Testing the ckm model with kaon experiments. *Progress of Theoretical Physics*, 122(1):81–101, 2009.

[27] A. Bohr and B. R Mottelson. *Nuclear Structure, Vol. 1.* W. A. Benjamin, 1969.

[28] E. Borie and G. A. Rinker. Improved calculation of the muonic-helium lamb shift. *Phys. Rev. A*, 18(2):324–327, Aug 1978.

[29] E. Borie and G. A. Rinker. The energy levels of muonic atoms. *Rev. Mod. Phys.*, 54(1):67, Jan 1982.

[30] Marie-Anne Bouchiat and Claude Bouchiat. Parity violation in atoms. *Reports on Progress in Physics*, 60(11):1351, 1997.

[31] M. Brodeur, T. Brunner, C. Champagne, S. Ettenauer, M. J. Smith, A. Lapierre, R. Ringle, V. L. Ryjkov, S. Bacca, P. Delheij, G. W. F. Drake, D. Lunney, A. Schwenk, and J. Dilling. First direct mass-measurement of the two-neutron halo nucleus 6He and improved mass for the four-neutron halo 8He. *ArXiv e-prints*, July 2011.

[32] B. A. Brown. 'the nuclear shell model towards the drip lines. *Progress in Particle and Nuclear Physics*, 47(2):517 – 599, 2001.

[33] Tomasz M Brzozowski, Maria Maczynska, Michal Zawada, Jerzy Zachorowski, and Wojciech Gawlik. Time-of-flight measurement of the temperature of cold atoms for short trap-probe beam distances. *Journal of Optics B: Quantum and Semiclassical Optics*, 4(1):62, 2002.

[34] P. A. Butler and W. Nazarewicz. Intrinsic reflection asymmetry in atomic nuclei. *Rev. Mod. Phys.*, 68(2):349–421, Apr 1996.

[35] E. Caurier and P. Navrátil. Proton radii of $^{4,6,8}He$ isotopes from high-precision nucleon-nucleon interactions. *Phys. Rev. C*, 73(2):021302, Feb 2006.

[36] F. Chautard, C. Berthe, A. Colombe, L. David, P. Dolegieviez, B. Jacquot, C. Jamet, M. Lechartier, P. Lehérissier, and G. Sénécal. Status report on GANIL-SPIRAL1. In D. Rifuggiato, editor, *Proceedings of the 18th International Conference on Cyclotrons and their Applications 18th International Conference on Cyclotrons and their Applications - Cyclotrons 2007*, pages 99–104, Giardini-Naxos Italy, 2007.

[37] C. Y. Chen, Y. M. Li, K. Bailey, T. P. O'Connor, L. Young, and Z.-T. Lu. Ultrasensitive Isotope Trace Analyses with a Magneto-Optical Trap. *Science*, 286(5442):1139–1141, 1999.

[38] Cheng Chin, Véronique Leiber, Vladan Vuletic, Andrew J. Kerman, and Steven Chu. Measurement of an electron's electric dipole moment using cs atoms trapped in optical lattices. *Phys. Rev. A*, 63(3):033401, Feb 2001.

[39] J. H. Christenson, J. W. Cronin, V. L. Fitch, and R. Turlay. Evidence for the 2π decay of the K_2^0 meson. *Phys. Rev. Lett.*, 13(4):138–140, Jul 1964.

[40] Tim Chupp. Permanent electric dipole moments of atoms and molecules. In P.R. Berman E. Arimondo and C.C. Lin, editors, *Advances In Atomic, Molecular, and Optical Physics*, volume 59 of *Advances In Atomic, Molecular, and Optical Physics*, pages 129 – 174. Academic Press, 2010.

[41] H. T. Coelho, T. K. Das, and M. R. Robilotta. Two-pion-exchange three-nucleon force and the ^3H and ^3He nuclei. *Phys. Rev. C*, 28(4):1812–1828, Oct 1983.

[42] C Cohen-Tannoudji. Bose-einstein condensation of metastable helium. *Physica Scripta*, 2002(T102):111, 2002.

[43] S. A. Coon, M. D. Scadron, P. C. McNamee, B. R. Barrett, D. W. E. Blatt, and B. H. J. McKellar. The two-pion-exchange three-nucleon potential and nuclear matter. *Nuclear Physics A*, 317(1):242 – 278, 1979.

[44] A. Couvert, T. Kawalec, G. Reinaudi, and D. Guéry-Odelin. Optimal transport of ultracold atoms in the non-adiabatic regime. *EPL (Europhysics Letters)*, 83(1):13001, 2008.

[45] S. De, U. Dammalapati, K. Jungmann, and L. Willmann. Magneto-optical trapping of barium. *Physical Review A (Atomic, Molecular, and Optical Physics)*, 79(4):041402, 2009.

[46] Derouard, J., Lombardi, M., and Jost, R. Forbidden singlet-triplet anticrossings in 3he : precise determination of n1d-n3d (n = 3-6) intervals. *J. Phys. France*, 41(8):819–830, 1980.

[47] J. Dobaczewski and J. Engel. Nuclear time-reversal violation and the schiff moment of ^{225}Ra. *Phys. Rev. Lett.*, 94:232502, Jun 2005.

[48] P. Doleschall, I. Borbely, Z. Papp, and W. Plessas. Nonlocality in the nucleon-nucleon interaction and three-nucleon bound states. *Phys. Rev. C*, 67(6):064005, Jun 2003.

[49] G. Drake and Z.-C. Yan. Studies of light halo nuclei by the isotope shift method. *Hyperfine Interactions*, 172:141–147, 2006. 10.1007/s10751-007-9572-x.

[50] G. W. F. Drake. . In F. S. Levin and D. A. Micha, editors, *Long-Range Casimir Forces:Theory and Recent Experiments in Atomic Systems.* Plenum, New York, 1993.

[51] G. W. F. Drake. . In G. W. F. Drake, editor, *Atomic, Molecular, and Optical Physics Handbook*. Springer, New York, 2006.

[52] G. W. F. Drake. . private communication, 2007.

[53] G. W. F Drake, W Nörtershäuser, and Z.-C. Yan. Isotope shifts and nuclear radius measurements for helium and lithium. *Can. J. Phys.*, 83:311, 2005.

[54] V. A. Dzuba. private communication, 2008.

[55] V. A. Dzuba and V. V. Flambaum. private communication, 2007.

[56] V. A. Dzuba and V. V. Flambaum. Calculation of energy levels and transition amplitudes for barium and radium. *Jounal of Physics B Atomic Molecular Optical Physics*, 40, 2007.

[57] V. A. Dzuba and J. S. M. Ginges. Calculation of energy levels and lifetimes of low-lying states of barium and radium. *Physical Review A*, 73, 2006.

[58] VA Dzuba and VV Flambaum. Calculation of energy levels and transition amplitudes for barium and radium. *Journal of Physics B: Atomic, Molecular and Optical Physics*, 40(1):227–236, 2007.

[59] VA Dzuba and JSM Ginges. Calculations of energy levels and lifetimes of low-lying states of barium and radium. *Physical Review A*, 73(3):32503, 2006.

[60] A. R. Edmonds. *Angular Momentum in Quantum Mechanics*. Princeton University Press, Princeton, New Jersey, 1996.

[61] J. Engel, M. Bender, J. Dobaczewski, J. H. de Jesus, and P. Olbratowski. Time-reversal violating schiff moment of ^{225}Ra. *Phys. Rev. C*, 68(2):025501, Aug 2003.

[62] J. Engel, J. L. Friar, and A. C. Hayes. Nuclear octupole correlations and the enhancement of atomic time-reversal violation. *Phys. Rev. C*, 61(3):035502, Feb 2000.

[63] R. Engfer, H. Schneuwly, J.L. Vuilleumier, H.K. Walter, and A. Zehnder. Charge-distribution parameters, isotope shifts, isomer shifts, and magnetic hyperfine constants from muonic atoms. *Atomic Data and Nuclear Data Tables*, 14(5-6):509 – 597, 1974. Nuclear Charge and Moment Distributions.

[64] Fang Fang and David S. Weiss. Resonator-enhanced optical guiding and trapping of cs atoms. *Opt. Lett.*, 34(2):169–171, Jan 2009.

[65] Christopher J. Foot. *Atomic Physics*. Oxford University Press, 2005.

[66] E. N. Fortson, F. G. Major, and H. G. Dehmelt. Ultrahigh resolution $\Delta F = 0, \ \pm 1$ $(He^3)^+$ hfs spectra by an ion-storage collision technique. *Phys. Rev. Lett.*, 16(6):221–225, Feb 1966.

[67] Mark Fred, Frank S. Tomkins, James K. Brody, and Morton Hamermesh. The spectrum of he^3 i. *Phys. Rev.*, 82:406–421, May 1951.

[68] R. R. Freeman, P. F. Liao, R. Panock, and L. M. Humphrey. Isotope shift of the $2^3p - 3^3d$ transition in helium. *Phys. Rev. A*, 22:1510–1516, Oct 1980.

[69] James Lewis Friar and John W. Negele. Theoretical and experimental determination of nuclear charge distributions. *Adv. Nucl. Phys.*, 8:219–376, 1973.

[70] M. C. George, L. D. Lombardi, and E. A. Hessels. Precision microwave measurement of the $2^3p_1 - 2^3p_0$ interval in atomic helium: A determination of the fine-structure constant. *Phys. Rev. Lett.*, 87:173002, Oct 2001.

[71] Vladislav Gerginov and Carol E. Tanner. Fluorescence of a highly collimated atomic cesium beam: theory and experiment. *Optics Communications*, 222(1-6):17 – 28, 2003.

[72] J. S. M. Ginges and V. V. Flambaum. Violations of fundamental symmetries in atoms and tests of unification theories of elementary particles. *Physics Reports*, 397(2):63 – 154, 2004.

[73] S. Goudsmit and R. F. Bacher. Anomalies in hyperfine structure. *Phys. Rev.*, 43:894–899, Jun 1933.

[74] W. C. Griffith, M. D. Swallows, T. H. Loftus, M. V. Romalis, B. R. Heckel, and E. N. Fortson. Improved limit on the permanent electric dipole moment of ^{199}Hg. *Physical Review Letters*, 102(10):101601, 2009.

[75] R. Grimm, M. Weidemuller, and Y. B. Ovchinnikov. Optical dipole traps for neutral atoms. *Advances in Atomic, Molecular and Optical Physics*, 42, 2000.

[76] Theoretical HEP group Radboud University Nijmegen. `http://nn-online.org`.

[77] JR Guest, ND Scielzo, I. Ahmad, K. Bailey, JP Greene, RJ Holt, ZT Lu, TP O'Connor, and DH Potterveld. Laser trapping of ^{225}Ra and ^{226}Ra with repumping by room-temperature blackbody radiation. *Phys Rev Lett*, 98(9):093001, 2007.

[78] T. L. Gustavson, A. P. Chikkatur, A. E. Leanhardt, A. Görlitz, S. Gupta, D. E. Pritchard, and W. Ketterle. Transport of bose-einstein condensates with optical tweezers. *Phys. Rev. Lett.*, 88(2):020401, Dec 2001.

[79] D. M. Harber and M. V. Romalis. Measurement of the scalar stark shift of the $6^1S \rightarrow 6^3P_1$ transition in hg. *Phys. Rev. A*, 63(1):013402, Nov 2000.

[80] W. C. Haxton and E. M. Henley. Enhanced t-nonconserving nuclear moments. *Phys. Rev. Lett.*, 51(21):1937–1940, Nov 1983.

[81] R.G. Helmer, M.A. Lee, C.W. Reich, and I. Ahmad. Intrinsic reflection asymmetry in ^{225}ra: Additional information from a study of the [alpha]-decay scheme of ^{229}th. *Nuclear Physics A*, 474(1):77 – 113, 1987.

[82] E. A. Hinds, J. D. Prestage, and F. M. J. Pichanick. Analysis of a level-crossing experiment on the 2 ^3p state of ^{3}He. *Phys. Rev. A*, 33:68–71, Jan 1986.

[83] R. Hofstadter. http://nobelprize.org/nobel_prizes/physics/laureates/1961/hofstadter-lecture.html.

[84] Robert Hofstadter. Electron scattering and nuclear structure. *Rev. Mod. Phys.*, 28(3):214–254, Jul 1956.

[85] F. Hoogeveen. The standard model prediction for the electric dipole moment of the electron. *Nuclear Physics B*, 341(2):322 – 340, 1990.

[86] C. J. Horowitz, S. J. Pollock, P. A. Souder, and R. Michaels. Parity violating measurements of neutron densities. *Phys. Rev. C*, 63(2):025501, Jan 2001.

[87] J. J. Hudson, D. M. Kara, I. J. Smallman, B. E. Sauer, M. R. Tarbutt, and E. A. Hinds. Improved measurement of the shape of the electron. *Nature*, 473:493–496, 2011.

[88] L. R. Hunter, D. Krause Jr., S. Murthy, and T. W. Sung. Precision measurement of the stark shift of the cesium d lines. *Phys. Rev. A*, 37(9):3283–3292, May 1988.

[89] Jun ichi Fujita and Hironari Miyazawa. Pion theory of three-body forces. *Progress of Theoretical Physics*, 17(3):360–365, 1957.

[90] Takeyasu M Ito and the nEdm Collaboration. Plans for a neutron edm experiment at sns. *Journal of Physics: Conference Series*, 69(1):012037, 2007.

[91] Y. Iwata, K. Ieki, A. Galonsky, J. J. Kruse, J. Wang, R. H. White-Stevens, E. Tryggestad, P. D. Zecher, F. Deak, A. Horvath, A. Kiss, Z. Seres, J. J. Kolata, J. von Schwarzenberg, R. E. Warner, and H. Schelin. Dissociation of ^8He. *Phys. Rev. C*, 62(6):064311, Nov 2000.

[92] J. H. de Jesus and J. Engel. Time-reversal-violating schiff moment of ^{199}Hg. *Phys. Rev. C*, 72:045503, Oct 2005.

[93] H. Kamada, A. Nogga, W. Glockle, E. Hiyama, M. Kamimura, K. Varga, Y. Suzuki, M. Viviani, A. Kievsky, S. Rosati, J. Carlson, Steven C. Pieper, R. B. Wiringa, P. Navratil, B. R. Barrett, N. Barnea, W. Leidemann, and G. Orlandini. Benchmark test calculation of a four-nucleon bound state. *Phys. Rev. C*, 64(4):044001, Aug 2001.

[94] Hidetoshi Katori, Tetsuya Ido, Yoshitomo Isoya, and Makoto Kuwata-Gonokami. Magneto-optical trapping and cooling of strontium atoms down to the photon recoil temperature. *Phys. Rev. Lett.*, 82(6):1116–1119, Feb 1999.

[95] Iosif B. Khriplovich and Steve K. Lamoreaux. *CP Violation without Strangeness.* Springer, 1997.

[96] T. KIBEDI and R. H. SPEAR. Reduced electric-octupole transition probabilities, $B(E3; 0_1^+ \rightarrow 3_1^-)$–an update. *Atomic Data and Nuclear Data Tables*, 80(1):35 – 82, 2002.

[97] A. Kievsky, M. Viviani, and S. Rosati. Study of bound and scattering states in three-nucleon systems. *Nuclear Physics A*, 577(3-4):511 – 527, 1994.

[98] S. J. M. Kuppens, K. L. Corwin, K. W. Miller, T. E. Chupp, and C. E. Wieman. Loading an optical dipole trap. *Phys. Rev. A*, 62(1):013406, Jun 2000.

[99] M. Lacombe, B. Loiseau, J. M. Richard, R. Vinh Mau, J. Côté, P. Pirès, and R. de Tourreil. Parametrization of the paris $n-n$ potential. *Phys. Rev. C*, 21(3):861–873, Mar 1980.

[100] F. Landré-Pellemoine et al. Recent results at the SIRa test bench: Diffusion properties of carbon graphite and B4C targets. *Nuclear Physics A*, 701(1-4):491 – 494, 2002. 5th International Conference on Radioactive Nuclear Beams.

[101] T. D. Lee and C. N. Yang. Question of parity conservation in weak interactions. *Phys. Rev.*, 104(1):254–258, Oct 1956.

[102] J. Léonard, M. Walhout, A. P. Mosk, T. Mueller, M. Leduc, and C. Cohen-Tannoudji. Giant helium dimers produced by photoassociation of ultracold metastable atoms. *Phys. Rev. Lett.*, 91(7):073203, Aug 2003.

[103] Michael A. Lieberman and Allan J. Lichtenberg. *Principles of Plasma Discharges and Materials Processing*. John Wiley and Sons, Inc., 2005.

[104] R. Machleidt. High-precision, charge-dependent bonn nucleon-nucleon potential. *Phys. Rev. C*, 63(2):024001, Jan 2001.

[105] F. Marin, F. Minardi, F. S. Pavone, M. Inguscio, and G. W. F. Drake. Hyperfine structure of the 3^3P state of ^{3}He and isotope shift for the 2^3S-3^3P$_0$ transition. *Zeitschrift fur Physik D Atoms, Molecules and Clusters*, 32:285–293, 1995. 10.1007/BF01437272.

[106] R. Maruyama, R. H. Wynar, M. V. Romalis, A. Andalkar, M. D. Swallows, C. E. Pearson, and E. N. Fortson. Investigation of sub-doppler cooling in an ytterbium magneto-optical trap. *Phys. Rev. A*, 68(1):011403, Jul 2003.

[107] Kirill Melnikov and Timo van Ritbergen. Three-loop slope of the Dirac form factor and the $1S$ Lamb shift in hydrogen. *Phys. Rev. Lett.*, 84(8):1673–1676, Feb 2000.

[108] Harold J Metcalf and Peter van der Straten. *Laser Cooling and Trapping*. Springer, 1999.

[109] J. D. Miller, R. A. Cline, and D. J. Heinzen. Far-off-resonance optical trapping of atoms. *Phys. Rev. A*, 47(6):R4567–R4570, Jun 1993.

[110] P. Moller, J. R. Nix, W. D. Myers, and W. J. Swiatecki. Nuclear ground-state masses and deformations. *Atomic Data and Nuclear Data Tables*, 59(2):185 – 381, 1995.

[111] C.E. Moore. Atomic energy levels. *NBS Circular 467*, 3, 1958.

[112] Donald C. Morton, Qixue Wu, and G. W. F. Drake. Nuclear charge radius for ^{3}He. *Phys. Rev. A*, 73:034502, Mar 2006.

[113] Donald C Morton, Qixue Wu, and G WF Drake. Energy levels for the stable isotopes of atomic helium(4he i and 3he i). *Canadian Journal of Physics*, 84(2):83–105, 2006.

[114] P. Mueller, I. A. Sulai, A. C. C. Villari, J. A. Alcántara-Núñez, R. Alves-Condé, K. Bailey, G. W. F. Drake, M. Dubois, C. Eléon, G. Gaubert, R. J. Holt, R. V. F. Janssens, N. Lecesne, Z.-T. Lu, T. P. O'Connor, M.-G. Saint-Laurent, J.-C. Thomas, and L.-B. Wang. Nuclear charge radius of ^8He. *Phys. Rev. Lett.*, 99(25):252501, Dec 2007.

[115] P. Mueller, L.-B. Wang, G. W. F. Drake, K. Bailey, Z.-T. Lu, and T. P. O'Connor. Fine structure of the $1s3p\,^3P_J$ level in atomic ^4He: Theory and experiment. *Phys. Rev. Lett.*, 94(13):133001, Apr 2005.

[116] R. Neugart, E.W. Otten, K. Wendt, S. Ahmad, N. Panigrahy, R.W. Dougherty, K.C. Mishra, T.P. Das, and J. Andriessen. Evaluation of the magnetic moments of radium isotopes. *Hyperfine Interactions*, 59(1):145–148, 1990.

[117] A. Nogga, D. Huber, H. Kamada, and W. Glockle. Triton binding energies for modern nn forces and the [pi]-[pi] exchange three-nucleon force. *Physics Letters B*, 409(1-4):19 – 25, 1997.

[118] K. M. O'Hara, S. R. Granade, M. E. Gehm, and J. E. Thomas. Loading dynamics of CO_2 laser traps. *Phys. Rev. A*, 63(4):043403, Mar 2001.

[119] A.N. Ostrowski, H.G. Bohlen, B. Gebauer, S.M. Grimes, R. Kalpakchieva, Th. Kirchner, T.N. Massey, W. von Oertzen, Th. Stolla, M. Wilpert, and Th. Wilpert. Spectroscopy of ^{10}he. *Physics Letters B*, 338(1):13 – 19, 1994.

[120] K. Pachucki and A. M. Moro. Nuclear polarizability of helium isotopes in atomic transitions. *Phys. Rev. A*, 75(3):032521, Mar 2007.

[121] Krzysztof Pachucki and Jonathan Sapirstein. Higher-order recoil corrections to helium fine structure. *Journal of Physics B: Atomic, Molecular and Optical Physics*, 36(5):803–809, 2003.

[122] A. Palffy. Nuclear effects in atomic transitions. *Contemporary Physics*, 51(6):471, 2010.

[123] Michael E. Peskin and Daniel V. Schroeder. *An Introduction to Quantum Field Theory*. Addison-Wesley, 1995.

[124] Wolfgang Petrich, Michael H. Anderson, Jason R. Ensher, and Eric A. Cornell. Behavior of atoms in a compressed magneto-optical trap. *J. Opt. Soc. Am. B*, 11(8):1332–1335, 1994.

[125] Steven C. Pieper. Quantum monte carlo calculations of light nuclei. *Nuclear Physics A*, 751:516 – 532, 2005. Proceedings of the 22nd International Nuclear Physics Conference (Part 1).

[126] Steven C. Pieper. Quantum monte carlo calculations of light nuclei. *Rivista del Nuovo Cimento*, 31(12):709, 2008.

[127] Steven C. Pieper, V. R. Pandharipande, R. B. Wiringa, and J. Carlson. Realistic models of pion-exchange three-nucleon interactions. *Phys. Rev. C*, 64(1):014001, Jun 2001.

[128] Steven C. Pieper and R. B. Wiringa. Quantum monte carlo calculations of light nuclei. *Annual Review of Nuclear and Particle Science*, 51(1):53–90, 2001.

[129] Randolf Pohl et al. The size of the proton. *Nature*, 466:213, 2010.

[130] Maxim Pospelov and Adam Ritz. Electric dipole moments as probes of new physics. *Annals of Physics*, 318(1):119 – 169, 2005. Special Issue.

[131] J. D. Prestage, E. A. Hinds, and F. M. J. Pichanick. Precise measurements of hyperfine structure in the 2^3p state of ^{3}He. *Phys. Rev. Lett.*, 50:828–832, Mar 1983.

[132] M. A. Preston and R. K. Bhaduri. *Structure of the Nucleus*. Addison-Wesley Publishing Company, 1975.

[133] PREX. `http://hallaweb.jlab.org/parity/prex/`.

[134] Mariusz Puchalski and Krzysztof Pachucki. Nuclear structure effects in the isotope shift with halo nuclei. *Hyperfine Interactions*, 196:35–42, 2010. 10.1007/s10751-009-0137-z.

[135] E. M. Purcell and N. F. Ramsey. On the possibility of electric dipole moments for elementary particles and nuclei. *Phys. Rev.*, 78(6):807, Jun 1950.

[136] P. Quinet, C. Argante, V. Fivet, C. Terranova, A. V. Yushchenko, and É. Biémont. Atomic data for radioactive elements Ra I, Ra II, Ac I and Ac II and application to their detection in HD 101065 and HR 465. *Astron. Astrophys.*, 474:307–314, 2007.

[137] E. Rasmussen. Das bogenspektrum des radiums. *Zeitschrift fur Physik A Hadrons and Nuclei*, 87, 1934.

[138] B. C. Regan, Eugene D. Commins, Christian J. Schmidt, and David DeMille. New limit on the electron electric dipole moment. *Phys. Rev. Lett.*, 88(7):071805, Feb 2002.

[139] E. Riis, A. G. Sinclair, O. Poulsen, G. W. F. Drake, W. R. C. Rowley, and A. P. Levick. Lamb shifts and hyperfine structure in $^6Li^+$ and $^7Li^+$: Theory and experiment. *Phys. Rev. A*, 49:207–220, Jan 1994.

[140] M. V. Romalis and E. N. Fortson. Zeeman frequency shifts in an optical dipole trap used to search for an electric-dipole moment. *Phys. Rev. A*, 59(6):4547–4558, Jun 1999.

[141] H. N. Russell. The spectrum and ionization potential of radium. *Phys. Rev.*, 46:989–990, 1934.

[142] V. L. Ryjkov, M. Brodeur, T. Brunner, M. Smith, R. Ringle, A. Lapierre, F. Ames, P. Bricault, M. Dombsky, P. Delheij, D. Lunney, M. R. Pearson, and J. Dilling. Direct mass measurement of the four-neutron halo nuclide ^8He. *Phys. Rev. Lett.*, 101(1):012501, Jul 2008.

[143] Robert G. Sachs. *The Physics of Time Reversal*. The University of Chicago Press, 1987.

[144] M. Schellekens, R. Hoppeler, A. Perrin, J. Viana Gomes, D. Boiron, A. Aspect, and C. I. Westbrook. Hanbury Brown Twiss Effect for Ultracold Quantum Gases. *Science*, 310(5748):648–651, 2005.

[145] L. I. Schiff. Measurability of nuclear electric dipole moments. *Phys. Rev.*, 132(5):2194–2200, Dec 1963.

[146] N. Scielzo. Measurement of the lifetimes of the lowest $^3P_1$ state of neutral Ba and Ra. *Physical Review A*, 73, 2006.

[147] D. Shiner, R. Dixson, and V. Vedantham. Three-nucleon charge radius: A precise laser determination using ^{3}He. *Phys. Rev. Lett.*, 74(18):3553–3556, May 1995.

[148] I. Sick. Precise radii of light nuclei from electron scattering. *Lecture Notes in Physics*, 745:57, 2008.

[149] Ingo Sick. Precise root-mean-square radius of ^4He. *Phys. Rev. C*, 77(4):041302, Apr 2008.

[150] I. I. Sobelman. *Atomic Spectra and Radiative Transitions*. Springer-Verlag, 1979.

[151] Marco S. Sozzi. *Discrete Symmetris and CP Violation*. Oxford University Press, 2008.

[152] V. Spevak, N. Auerbach, and V. V. Flambaum. Enhanced t-odd, p-odd electromagnetic moments in reflection asymmetric nuclei. *Phys. Rev. C*, 56(3):1357–1369, Sep 1997.

[153] V. G. J. Stoks, R. A. M. Klomp, C. P. F. Terheggen, and J. J. de Swart. Construction of high-quality nn potential models. *Phys. Rev. C*, 49(6):2950–2962, Jun 1994.

[154] I. A. Sulai, Qixue Wu, M. Bishof, G. W. F. Drake, Z.-T. Lu, P. Mueller, and R. Santra. Hyperfine suppression of $2\,^3S_1 - 3\,^3P_J$ transitions in ^3He. *Phys. Rev. Lett.*, 101(17):173001, Oct 2008.

[155] O.P. Sushkov, V.V. Flambaum, and I.B. Khriplovich. On the possibility to study p odd and t odd nuclear forces in atomic and molecular experiments. *Zh. Eksp. Teor. Fiz. (JETP)*, 84:1521, 1984.

[156] M. Swallows. *A search for the permanent electric dipole moment of mercury-199*. PhD thesis, The University of Washington, 2007.

[157] Andrzej Szczepkowicz, Leszek Krzemień, Adam Wojciechowski, Krzysztof Brzozowski, Michael Krüger, Michał Zawada, Marcin Witkowski, Jerzy Zachorowski, and Wojciech Gawlik. Optimal geometry for efficient loading of an optical dipole trap. *Phys. Rev. A*, 79(1):013408, Jan 2009.

[158] I. Tanihata, D. Hirata, T. Kobayashi, S. Shimoura, K. Sugimoto, and H. Toki. Revelation of thick neutron skins in nuclei. *Physics Letters B*, 289(3-4):261 – 266, 1992.

[159] K. Tillmann, H. J. Andrä, and W. Wittmann. Hyperfine-structure studies of ^{3}He by zero-field quantum beats. *Phys. Rev. Lett.*, 30:155–158, Jan 1973.

[160] W. L. Trimble, I. A. Sulai, I. Ahmad, K. Bailey, B. Graner, J. P. Greene, R. J. Holt, W. Korsch, Z.-T. Lu, P. Mueller, and T. P. O'Connor. Lifetime of the $7s6d\ ^1D_2$ atomic state of radium. *Phys. Rev. A*, 80(5):054501, Nov 2009.

[161] Wim Vassen and Wim Hogervorst. High-resolution uv laser spectroscopy of the 1s2s $^3S_1 \rightarrow$ 1snp (n=5–79) transitions in ^3He and ^4He. *Phys. Rev. A*, 39(9):4615–4627, May 1989.

[162] A.C.C. Villari, C. Barué, G. Gaubert, S. Gibouin, Y. Huguet, P. Jardin, S. Kandri-Rody, F. Landré-Pellemoine, N. Lecesne, R. Leroy, M. Lewitowicz, C. Marry, L. Maunoury, J.Y. Pacquet, J.P. Rataud, M.G. Saint-Laurent, C. Stodel, J.C. Angélique, N.A. Orr, and R. Lichtenthäler. Ion source developments for RNB production at SPIRAL/GANIL. *Nuclear Physics A*, 701(1-4):476 – 479, 2002. 5th International Conference on Radioactive Nuclear Beams.

[163] A C Vutha, W C Campbell, Y V Gurevich, N R Hutzler, M Parsons, D Patterson, E Petrik, B Spaun, J M Doyle, G Gabrielse, and D DeMille. Search for the electric dipole moment of the electron with thorium monoxide. *Journal of Physics B: Atomic, Molecular and Optical Physics*, 43(7):074007, 2010.

[164] L.-B. Wang. *Determination of the Helium-6 Nuclear Charge Radius Using High-Resolution Laser Spectroscopy*. PhD thesis, The University of Illinois at Urbana Champaign, 2004.

[165] L.-B. Wang, P. Mueller, K. Bailey, G. W. F. Drake, J. P. Greene, D. Henderson, R. J. Holt, R. V. F. Janssens, C. L. Jiang, Z.-T. Lu, T. P. O'Connor, R. C. Pardo, K. E. Rehm, J. P. Schiffer, and X. D. Tang. Laser spectroscopic determination of the ^6He nuclear charge radius. *Phys. Rev. Lett.*, 93(14):142501, Sep 2004.

[166] K. Wendt, S. A. Ahmad, W. L. Klempt, R. Neugart, E. W. Otten, and H. H. Stroke. On the hyperfine structure and isotope shift of radium. *Zeitschrift fur Physik D Atoms, Molecules and Clusters*, 4, 1987.

[167] R. Wiringa. Nucleon-nucleon interactions. In Xing-Wang Pan, Da Hsuan Feng, and Michel Vallières, editors, *Contemporary Nuclear Shell Models*, volume 482 of *Lecture Notes in Physics*, pages 1–24. Springer Berlin / Heidelberg, 1997. 10.1007/BFb0104360.

[168] R. B. Wiringa, V. G. J. Stoks, and R. Schiavilla. Accurate nucleon-nucleon potential with charge-independence breaking. *Phys. Rev. C*, 51(1):38–51, Jan 1995.

[169] Robert. Wiringa. private communication, 2011.

[170] Samuel S. M. Wong. *Introductory Nuclear Physics*. Wiley-VCH, 1998.

[171] C. S. Wu, E. Ambler, R. W. Hayward, D. D. Hoppes, and R. P. Hudson. Experimental test of parity conservation in beta decay. *Phys. Rev.*, 105(4):1413–1415, Feb 1957.

[172] Hideki Yukawa. Models and methods in the meson theory. *Rev. Mod. Phys.*, 21(3):474–479, Jul 1949.

[173] T. Zelevinsky, D. Farkas, and G. Gabrielse. Precision measurement of the three 2^3P_J helium fine structure intervals. *Phys. Rev. Lett.*, 95(20):203001, Nov 2005.

[174] X. Zhan et al. High Precision Measurement of the Proton Elastic Form Factor Ratio $\mu_p G_E/G_M$ at low Q^2. *arXiv*, 2011.